

# *Engineering Documents*

---

*University of Pennsylvania*

*Year 1993*

---

## Optical Studies of the Structure and Dynamics of Opaque Colloids

Peter D. Kaplan  
University of Pennsylvania,

University of Pennsylvania, Dissertation, 1993.

This paper is posted at ScholarlyCommons@Penn.  
<http://repository.upenn.edu/seas.docs/4>

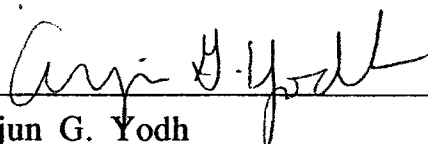
Optical Studies of the Structure  
and Dynamics of Opaque Colloids

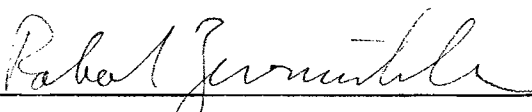
Peter D. Kaplan

A DISSERTATION IN  
PHYSICS

Presented to the Faculties of the University of Pennsylvania  
in Partial Fulfillment of the Requirements for the Degree of  
Doctor of Philosophy.

1993

  
\_\_\_\_\_  
Arjun G. Yodh  
Supervisor of Dissertation

  
\_\_\_\_\_  
Robert W. Zarnuhle  
Graduate Group Chairperson

# Acknowledgements

The subject of multiple scattering happened into my life during my first year at the University of Pennsylvania, when my advisor, Arjun Yodh, heard a talk by my undergraduate Electricity and Magnetism Professor, David Pine. The three of us have been working together and separately on the subject ever since. It is a subject which treats an extremely basic phenomena that is not covered in the formal physics curriculum. In class, we learn that when light is reflected, the angle of incidence is equal to the angle of reflection. This description does not explain the appearance of white materials such as clouds, dairy products, biological tissues, paints, sugar, or flour.

Many people contributed to this work directly and indirectly. To all of them I am most grateful. I especially thank Arjun Yodh, who shared his sense of scientific ambition, enthusiasm, and energy with me. David Pine's patient and expert guidance were indispensable in the early stages of this work, when we were being introduced to colloid science. His insight and hard work have continued to play a critical role in selecting, defining, and solving problems throughout this thesis.

It has been my great pleasure to meet and learn from many people at Exxon, including David Weitz, Paul Chaikin, Scott Milner, Harry Deckman, J.Z. Xue, Fred MacKintosh, Doug Durian, Andrea Liu, Paul Dixon, Kalman Migler, Connie Gettinger, David Morse, and Tom Mason.

At the University of Pennsylvania, the expert assistance of the faculty have been invaluable. I must single out Tom Lubensky, who has lent a patient ear and offered

excellent advice throughout. From discourse to discussions, other members of the Physics department have been tremendously helpful, including Paul Heiney, Elias Burstein, and Ralph Amado. One of the best surprises at Penn. was the discovery of a biological community also interested in multiple scattering. These people helped to broaden my perspective, but more importantly, they provided camaraderie and companionship in discussing the basic questions of multiple scattering. Led by the esteemed and humorous Briton Chance, Dinos Gonatas, Kyung Kang, Eva Sevick, and John Haselgrove shared many lively discussions with me.

The people in our laboratory have made my time at Penn. far richer and more productive. I thank especially, Mohsen Yeganeh, who has been with me in the lab since it opened. David Boas, Tony Dinsemore, Jennifer Rouke, Maureen O'Leary, Jining Qi, Joe Culver, Ming Hsü Kao, and Ilya Koltover all helped to share laboratory responsibilities and made the lab an interesting and productive place. The companionship and advice of other physics friends including Bruce Gluckman, Dan Grupp, Alan Blankman, Laura Smilowitz, and Cynthia Schwartz have been crucial at both the painful and exciting phases of graduate school.

I thank David Townsend and H. N. Cheng of Hercules for bringing us an important industrial problem to which we could apply multiple light scattering.

Of course, many people contributed to this thesis in less direct ways, many of them before I arrived at Penn. Beginning with the people closest to my work, I thank Jerry Gollub, in whose laboratory I learned how absolutely fascinating and dynamic Physics is even as I was becoming disenchanted with formal classroom work. After graduating from Haverford College, Paul Citrin and Robert Hamers sequentially gave me the opportunity to work in different areas of condensed matter physics in the best conditions of industrial laboratories. Finally, I thank Albert Libchaber, for providing my next destination in Physics after Penn.

Science is not pursued in a vacuum. It has been my family who have been responsible for the good work that I have managed to achieve. My parents, Albert and

Deborah Kaplan, managed to raise me to have the confidence (perhaps arrogance) to approach and overcome life's challenges. I am grateful for the friendship and love of my sister, Diana, my brother Gary, and my brother-in-law, Peter Holquist.

Most importantly, my beautiful wife and best friend, Deirdre O'Halloran, has provided the love and support that held me fast during the difficult times. She has shared in the successes of these five years, and has given me perspective on what is really important: our long journey together. With humor and patience, she taught me the little grammar I know. Most concretely, her careful, late-night editing of this manuscript is responsible for whatever is stylistically successful within it. The blame for the rest lies on my shoulders.

Most concretely of all, I am grateful to the University of Pennsylvania (for start-up funds) and the National Science Foundation (through grant number DMR-9003687 and the Materials Research program through the Laboratory for Research on the Structure of Matter) for funding my graduate education, laboratory equipment, and supplies.

# Abstract

## Optical Studies of the Structure and Dynamics of Opaque Colloids

Peter D. Kaplan

Arjun G. Yodh

Three fundamental experiments on multi-particle interactions in hard-sphere systems are presented in this thesis. In the first experiment, a mixture of two monodisperse colloids with different particle diameters, but the same particle composition, is studied using diffusing-wave spectroscopy. We find that both the particle structure and the hydrodynamic interactions between large and small balls are well modeled by existing theories. These theories, however, do not comment on the observed diffusion of particles in complex solutions over distances larger than a particle diameter. Incidental observations during this experiment led to the second experiment, the study of the phase diagram of binary hard-sphere mixtures of colloidal particles. In the process of mapping this phase diagram, driven entirely by entropy, a novel surface phase was discovered. This surface phase is explained geometrically in terms of the entropy of the small particles in the suspension. In the final experiment, the diffuse model of photon transport is extended to create a new technique called Diffuse Transmission Spectroscopy (DTS) for exploiting the wave vector dependent structure of colloidal suspensions. DTS uses the wavelength dependent transmission of a slab of colloid to probe interparticle structure. The diffuse transmission spectrum is shown to be useful for measuring particle diameter and differences in interparticle potential in dense, undiluted systems, as well as for testing the validity of structural models.

# Contents

<b>Acknowledgements</b>	<b>ii</b>
<b>Abstract</b>	<b>v</b>
<b>1 Multiple Scattering and Dense Colloids</b>	<b>1</b>
<b>2 Photon Transport in Static Media</b>	<b>8</b>
2.1 Single Scattering of Light . . . . .	8
2.2 Microscopic Picture of Diffuse Transport . . . . .	11
2.3 Random Walks . . . . .	18
2.4 The Diffusion Equation . . . . .	20
2.5 Measuring $l^*$ . . . . .	21
2.6 Time Dependent Transport . . . . .	26
<b>3 Photon transport in dynamic media: diffusing-wave spectroscopy</b>	<b>32</b>
3.1 Introduction . . . . .	32
3.2 Dynamic Single Scattering . . . . .	33
3.3 Multiple Scattering . . . . .	35
3.4 DWS of Photons which have Traveled Paths of Different Lengths . . . . .	38
3.5 The Siegert Relation . . . . .	39
3.6 Collective Diffusion . . . . .	44
3.7 Analytic Techniques . . . . .	48

3.7.1	Obtaining $g_1(\tau)$ . . . . .	48
3.7.2	Analytic forms of $g_1(\tau)$ . . . . .	49
3.7.3	Backscattering . . . . .	50
3.7.4	Transmission . . . . .	51
<b>4</b>	<b>Miscible Binary Systems: Dynamics and Structure</b>	<b>58</b>
4.1	Introduction and Survey . . . . .	58
4.2	Calculating $l^*$ in a Binary Mixture . . . . .	68
4.3	Interpreting DWS Measurements of Bidisperse Colloids . . . . .	70
4.4	Binary Structure Functions . . . . .	72
4.5	Stokes Flow and Hydrodynamics in Binary Systems . . . . .	73
<b>5</b>	<b>Phase Separation in Binary Colloids</b>	<b>82</b>
5.1	Introduction and Survey . . . . .	82
5.2	Calculation of Excluded Volume . . . . .	95
5.3	Coulomb Repulsion and van der Waals Attraction . . . . .	98
5.4	Comparison to a Simple Theory . . . . .	101
5.5	DWS Tests of Phase Separated Suspensions . . . . .	103
5.6	Preliminary Investigation of Surface Structure . . . . .	103
<b>6</b>	<b>Diffuse-Transmission Spectroscopy, a Static Probe of Structure</b>	<b>112</b>
6.1	Experiment . . . . .	117
6.2	Results . . . . .	121
6.3	Conclusion . . . . .	128
6.4	Direct Matrix Inversion . . . . .	130
6.5	Inversion by Expansion of $S(q)$ . . . . .	131
<b>7</b>	<b>Experimental Necessities</b>	<b>140</b>
7.1	Chemical Technique . . . . .	140
7.1.1	Measuring Small Volumes of Colloidal Samples . . . . .	140

7.1.2	Cleaning Glassware . . . . .	142
7.1.3	Polystyrene Spheres . . . . .	143
7.1.4	Making Colloidal Crystals . . . . .	144
7.1.5	The Metler Balance . . . . .	144
7.1.6	Clean Water . . . . .	147
7.2	Optical Technique . . . . .	148
7.2.1	Photomultiplier Tubes and Fiber Optics . . . . .	148
7.2.2	Collection Geometry . . . . .	150
7.2.3	Electronic Autocorrelators . . . . .	152
7.2.4	Argon-Ion Lasers . . . . .	154
7.2.5	Index of Refraction for Water and Polystyrene . . . . .	154
7.3	Computer Practice . . . . .	156
7.3.1	Laboratory Automation . . . . .	156
7.3.2	Data Analysis . . . . .	157
7.3.3	Pulse Counter . . . . .	158
7.3.4	Stepper-Motor Controller . . . . .	159
7.3.5	Mie Calculations . . . . .	162
	<b>Appendix</b>	<b>164</b>
	<b>A Listing of Mie Scattering Program</b>	<b>164</b>
	<b>Bibliography</b>	<b>177</b>
	<b>Index</b>	<b>188</b>

# List of Tables

4.1	Binary Systems in DWS Study . . . . .	60
5.1	Systems Tested for Phase Separation . . . . .	89
5.2	Previous Table Continued. . . . .	90
5.3	Previous Table Continued . . . . .	91
6.1	Systems in DTS Study . . . . .	129
6.2	Samples which Demonstrate Sensitivity of DTS to Interparticle Potential	130
7.1	Ar <sup>+</sup> -ion Laser Lines . . . . .	155
7.2	Configuration of Parallel Port . . . . .	157

# List of Figures

1.1	Multiple Scattering Geometry Used Throughout Thesis . . . . .	3
2.1	Scattering Geometry . . . . .	9
2.2	Relation Between Scattering Intensity and Structure . . . . .	11
2.3	Microscopic Picture of Scattering and the Quantities $l^*$ and $l$ . . . . .	15
2.4	Photon's Scatter From Small Groups of Particles . . . . .	15
2.5	Mie Scattering Geometry . . . . .	17
2.6	Distribution of Diffuse Energy Density in a Slab Under Steady Illumination. . . . .	23
2.7	The Net Flux . . . . .	24
2.8	Apparatus for Measuring Transmission . . . . .	25
2.9	Time Dependence of Transmitted Pulses . . . . .	28
3.1	QELS Apparatus . . . . .	34
3.2	Scattering of a Photon Through a <i>Path</i> . . . . .	36
3.3	Path is Described as a Sequence of Scattering Events. . . . .	37
3.4	Diffusing-wave Spectroscopy Apparatus . . . . .	38
3.5	Pulses Transmitted by a Slab of Colloid . . . . .	41
3.6	Graphic Illustration of Effect of Short Pulses on $g_2(\tau)$ . . . . .	43
3.7	Collective Diffusion . . . . .	45
3.8	DWS Backscattering Apparatus . . . . .	51
3.9	First Cumulant as a Function of Sample Thickness . . . . .	54
4.1	Graphic Comparison of Binary Systems Studied . . . . .	60

4.2	$l^*$ v. $\phi_S$ for Binary Colloid with Diameter Ratio of 3. . . . .	62
4.3	$D_{eff}$ vs $\phi_S$ for Binary Colloid with Diameter Ratio of 3. . . . .	66
4.4	Calculation of Scattering Intensity in a Binary Fluid . . . . .	68
4.5	Partial Structure Factors for Binary Mixtures . . . . .	74
5.1	Geometric Explanation of Binary Hard-Sphere Phase Separation . . .	85
5.2	Surface Crystallites as Viewed Under an Optical Microscope. . . . .	87
5.3	Phase Diagram of 460/65 nm System . . . . .	94
5.4	Overlap Volume Between Two Spheres . . . . .	96
5.5	Entropic Potential . . . . .	97
5.6	Comparison of Ball-Ball, and Ball-Wall Potentials . . . . .	97
5.7	Comparison of Experimental and Theoretical Phase Diagram . . . . .	104
5.8	DWS Autocorrelation Function for Crystalline Phase . . . . .	105
5.9	Two-Dimensional Geometry of Interstitial Spheres . . . . .	106
5.10	Three Dimensional Geometry of Interstitial Spheres . . . . .	107
5.11	SEM Image of Binary Crystal . . . . .	108
6.1	Form and Structure Factors for 299 nm Spheres . . . . .	114
6.2	Diffuse Transmission Spectroscopy Apparatus . . . . .	119
6.3	Direct Comparison of Diffuse Transmission Data with Percus-Yevick Calculation . . . . .	123
6.4	Sensitivity of DTS to Particle Size. . . . .	124
6.5	Dependence of Diffuse Transmission on Interaction Potential . . . . .	126
6.6	Illustration of Errors in $S(y)$ Due to Noise . . . . .	129
6.7	Diffuse Transmission Spectrum Fit with Set of Polynomials . . . . .	134
6.8	Diffuse Transmission Spectrum Fit with Set of Bessel Functions . . .	135
6.9	Diffuse Transmission Spectrum Fit with Set of Percus-Yevick Struc- ture Factors . . . . .	136
7.1	Calibration of Metler Balance . . . . .	146
7.2	Collection Geometry and the Concept of Speckle . . . . .	151

7.3	A Generic Makefile. . . . .	158
7.4	Schematic of Pulse Counter . . . . .	160
7.5	Schematic of Stepper Motor Controller . . . . .	161

# Chapter 1

## Multiple Scattering and Dense Colloids

Although not often studied, systems which multiply scatter light are probably more plentiful than single scattering systems. In this thesis, multiply scattered light is the principal tool used to study microscopic properties of dense colloidal suspensions. We work in the highly multiple scattering limit and in the absence of photon absorption. This means that our samples are opaque and white, like milk. The advantage of the highly multiple scattering limit is the applicability of the diffusion equation to describe photon transport.

From the wide variety of available multiple scattering materials, we have chosen to focus on colloidal suspensions of polystyrene spheres in water. Polystyrene spheres have been of interest to physicists for a variety of reasons. Often they are studied as a model for atomic systems. We have studied monodisperse colloids for their intrinsic interest as macroscopic systems whose properties are controlled largely by statistical mechanics. In the course of the work described in this thesis, existing optical multiple scattering techniques have been refined and new techniques developed, enabling us to learn new physics of this model system. These techniques and tools apply to a wide variety of systems such as paint, dairy products [1], biological tissue [2,3], and

coating materials (*e.g.*, paper size [4]).

The spheres, whose diameters typically range from 50 to 3000 nm, are manufactured in nearly monodisperse suspensions. The interparticle potential depends on the charge on the spheres and the concentration of ions in the solution (see Section 5.3). The range of the interaction can be made quite short, which allows us to treat the particles almost as if they were hard spheres.

Multiple scattering occurs in a variety of contexts, including nuclear fission, astronomy, and atmospheric physics. Many treatments of multiple scattering are quite broad; they cover a wide range of geometries and opacities [5]. While these treatments are powerful, we have restricted our attention to a narrow range of multiple scattering geometries. Thus, we may proceed without concerning ourselves with most of the specialized vocabulary and formalism of these treatments. In particular, all of the scattering data presented in this thesis were obtained in a single experimental geometry – transmission of a beam of light through a slab of colloid (Fig. 1.1). The light sources used in this thesis ranged from lasers to lamps, and the detectors included photomultiplier tubes and photodiodes. The scattering problem, that of light being transmitted through a slab, remains constant.

Chapters 2 and 3 are a review of the basic conceptual tools needed to discuss the three experiments presented in this thesis. In Chapter 2, we discuss the transport of light in an optically dense media. In Chapter 3, we consider dynamic samples and introduce the technique of diffusing-wave spectroscopy. After these introductory chapters, three experiments on opaque colloids are presented.

These experiments are motivated by the fundamental questions about dense suspensions which are questions about collective behavior. An isolated, suspended particle will undergo Brownian motion due to thermal fluctuations in the fluid around it. It will also settle (or rise) due to buoyant forces if its density is different than that of the fluid. Collective effects begin to appear if the interaction range of the particles is comparable to the average interparticle spacing. For hard sphere particles there

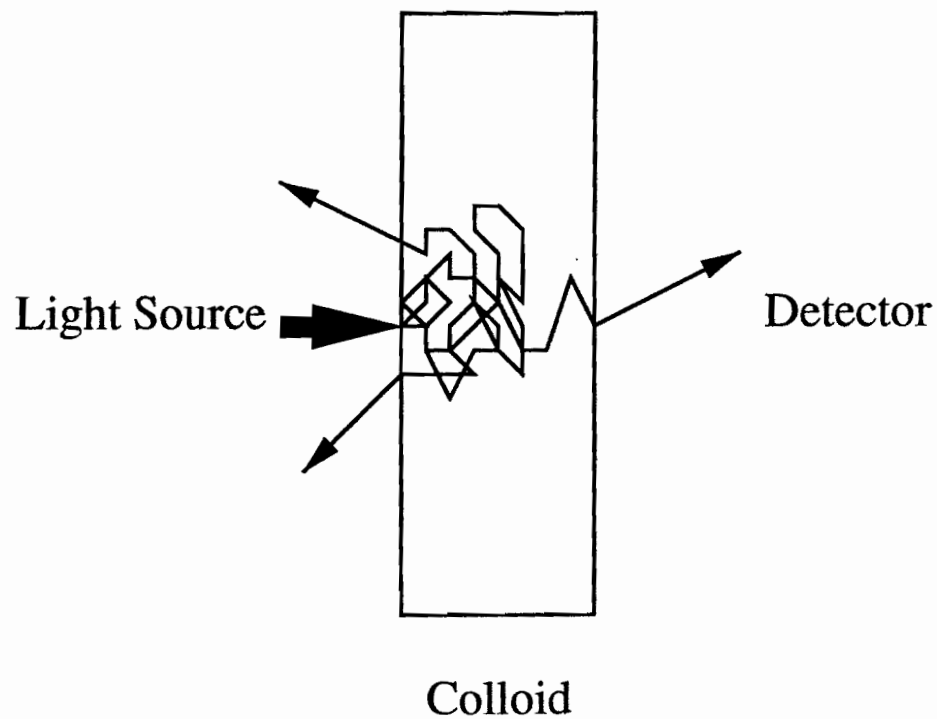


Figure 1.1: This is the geometry for multiple light scattering used throughout this thesis. Light strikes a slab of colloid. Most of the light is reflected. The light source and the detection scheme change with each experiment; the experimental geometry is constant throughout.

are two types of interactions: hydrodynamic interactions and entropic interactions.

The origin of the hydrodynamic interaction is simple. As a particle moves, the fluid around it moves and buffets neighboring particles. The effects of hydrodynamic interactions are not so simple. It is only in recent years that good measurements were made of the hydrodynamic suppression of the diffusion coefficient in the simplest system, monodisperse hard sphere colloids [6–10]. In commonly occurring suspensions such as milk, paint, dairy products, and the complex cytoplasm of biological cells, there are particles of different sizes diffusing and interacting with each other. In Chapter 4, we present the first measurements of the suppression of the diffusion coefficient in a system with two particle sizes. This experiment shows that collective effects on motion of particles over distances small compared to their diameter are well understood. This experiment also highlighted the fact that diffusion over longer distances is still poorly understood despite the fact that it is quite important in the familiar systems mentioned above.

The origin of entropic interactions is also quite simple. Wherever one particle is, no other particle can be. At volume fractions greater than a few percent, the fact that the particles cannot overlap noticeably affects the arrangement of particles in a suspension. This volume exclusion strongly influences the entropy of hard sphere systems. Roughly, the volume available to a particle is proportional to the number of states accessible to it, and the entropy is the logarithm of the number of states. Unlike dynamic hydrodynamic interactions which are calculated using fluid mechanics, calculations of entropic interactions rely on statistical mechanics and thermodynamics. The importance of particle ordering is emphasized throughout this thesis. In our studies of diffusion in binary systems in Chapter 4, we test an old theory of particle ordering and find that it works well for the systems being studied. In the next chapter, however, we find that in more concentrated systems and in systems with a larger ratio of large to small particle diameter, this old theory sometimes breaks down completely. Remarkably, in some of these systems, large and small particles un-mix into

phase separated states with higher total entropy. These experiments highlight the importance of improving our knowledge of the thermodynamics of dense mixtures of particles of different sizes by revealing complex, unexpected, and potentially useful facts about these systems.

The final experiment develops new experimental techniques for determination of structure in dense suspensions. Such structure is extremely difficult to probe, requiring large experimental facilities such as neutron sources or X-ray synchrotrons. There is a significant amount of information about structure, however, embedded in multiple scattering data. In Chapter 6, we focus on techniques for extracting that information from these systems. The results of this study indicate that while it may not be possible to measure structure factors directly, it is certainly possible to check model calculations and to make meaningful and detailed comparisons between colloidal systems using multiple light scattering.

The final chapter 7 contains experimentally useful information that is relevant to all of the preceding chapters.

In this thesis, we applied multiple light scattering to an important and simple set of systems and were able to extract significant new physical information about these systems. In particular, we have made important measurements about the collective static and dynamic properties of mixtures of hard spheres which indicate both the utility and success of simple theories about these systems and the limited range of these theories compared to the variety of behavior observed in these suspensions. The potential uses of multiple light scattering remain under explored and potentially quite powerful.

# Bibliography

- [1] D. G. Dalgleish and D. S. Horne, *Studies of gelation of acidified and renneted milks using diffusing-wave spectroscopy*, *Milchwissenschaft* **46**, 417 (1991).
- [2] M. A. O'Leary, D. A. Boas, B. Chance, and A. G. Yodh, *Refraction of diffuse photon density waves*, *Phys. Rev. Lett.* **69**, 2658 (1993).
- [3] D. A. Boas, M. A. O'Leary, B. Chance, and A. G. Yodh, *Scattering and Wavelength Transduction of Diffuse Photon Density Waves*, *Phys. Rev. E* **47**, R2999 (1993).
- [4] P. D. Kaplan, A. G. Yodh, and D. F. Townsend, *Noninvasive study of gel formation in polymer-stabilized dense colloids using multiply scattered light*, *J. Coll. and Int. Sci.* **155**, 31 (1993).
- [5] A. Ishimaru, in *Wave Propagation and Scattering in Random Media* (Academic Press, New York, 1978).
- [6] S. Fraden and G. Maret, *Multiple Light Scattering from Concentrated Interacting Suspensions*, *Phys. Rev. Lett.* **65**, 512 (1990).
- [7] X. Qiu *et al.*, *Hydrodynamic Interactions in Concentrated Suspensions*, *Phys. Rev. Lett.* **65**, 516 (1990).
- [8] A. G. Yodh, P. D. Kaplan, and D. J. Pine, *Pulsed Diffusing-Wave Spectroscopy: High Resolution through Nonlinear Optical Gating*, *Phys. Rev. B* **42**, 4744 (1990).

- [9] A. P. Philipse and A. Vrij, *Determination of Static and Dynamic Interactions Between Monodisperse Charged Silica Spheres in an Optically Matching Organic Solvent*, J. Chem. Phys. **88**, 6459 (1988).
- [10] A. van Veluwen, H. N. W. Lekkerkerker, C. G. de Kruif, and A. Vrij, *Measurement of the Short Time Self-diffusion Coefficient in Dilute and Concentrated Suspensions: Influence of Direct Particle Interactions*, J. Chem. Phys. **87**, 4873 (1987).

## Chapter 2

# Photon Transport in Static Media

When light enters a white material, such as a milk, where does it go? In the simplest explanation, the light scatters many times inside the material. When it eventually emerges, it is traveling in a random direction. Most of the light that enters a white material is reflected, which means that it leaves from the same surface that it enters from, although the angle of reflection is random, and thus not equal to the angle of incidence. The randomization of direction is responsible for the difference in appearance between a white surface and a mirror of the same total reflectivity. In this chapter we provide a much more detailed answer to the question of where the light goes. We will describe a microscopic picture of photon transport in optically dense media, from which we will develop the diffusion equation for photon transport. The diffusion equation will then be used to develop a useful and intuitive understanding of light propagation in highly multiple scattering materials.

### 2.1 Single Scattering of Light

Single scattering is a well known and commonly exploited tool for exploring weakly scattering samples. For generations, scientists interested in structure have used single scattering techniques, including X-ray, neutron, and light scattering to measure

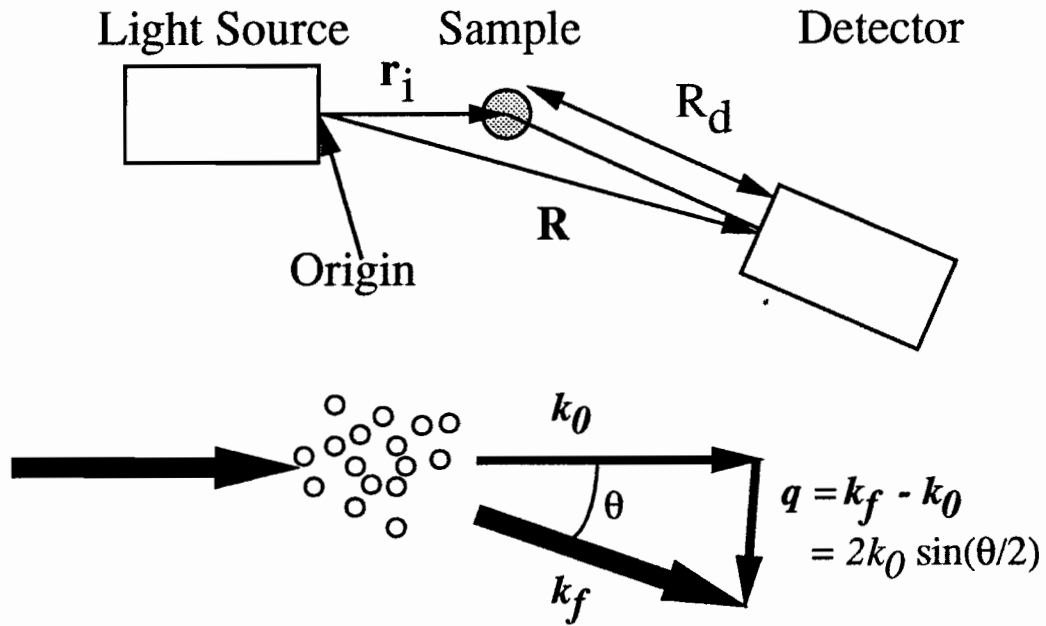


Figure 2.1: Scattering Geometry. The connection between scattering angle and wave-vector.

structure. There are several multiple scattering techniques in condensed matter physics such as LEED (low energy electron diffraction). Condensed matter physicists also study problems which fundamentally involve multiple scattering, including the photonic band structure and the localization of electrons, photons, and acoustic waves. Another example of the use of multiply scattered light in ordered media is the work of Pieranski on Kossel lines [1,2]. We begin the discussion of multiple scattering in disordered media by reviewing the connection between single scattering and sample structure. Ultimately, these ideas will be needed to connect multiple scattering data to the physics of dense colloidal systems.

In this introductory section we are concerned with calculating the single scattering intensity and making the connection between the scattering intensity and arrangement of particles in the sample.

In scattering problems, the illuminated particles are treated as a set of radiating sources whose radiated fields interfere with each other (Fig. 2.1). A beam of light originating at the origin scatters from a particle at  $\mathbf{r}$  through an angle  $\theta$  to a detector

at position  $\mathbf{R}$ , a distance  $R_d$  from the sample ( $R_d$  is much greater than the separation between particles). The electric field at the detector is

$$\mathbf{E}_{sc} = (E_o/\sqrt{4\pi R_d^2})(f_1(\theta)\hat{e}_1 + f_2(\theta)\hat{e}_2)e^{i\mathbf{q}\cdot\mathbf{r}_i+i\mathbf{k}_f\cdot\mathbf{R}}, \quad (2.1)$$

where  $f$  is the scattering amplitude into two orthogonal polarizations labeled 1 and 2,  $\mathbf{q}$  is the difference between the input and output wave-vectors  $\mathbf{k}_f - \mathbf{k}_0$ , and the magnitude of both  $\mathbf{k}_f$  and  $\mathbf{k}_0$  is  $2\pi/\lambda$ , where  $\lambda$  is the photon wavelength in the scattering medium. For an ensemble of identical particles, the field at the detector is calculated by adding the scattered field from each particle

$$\mathbf{E}_{sc} = (E_o/\sqrt{4\pi R_d^2})(f_1(\theta)\hat{e}_1 + f_2(\theta)\hat{e}_2)e^{i\mathbf{k}_f\cdot\mathbf{R}} \left( \sum_i e^{i\mathbf{q}\cdot\mathbf{r}_i} \right). \quad (2.2)$$

The scattered intensity is proportional to the square modulus of the scattered field

$$I(\mathbf{q}) = (|E_o|^2/4\pi R_d^2) (|f_1(\theta)|^2 + |f_2(\theta)|^2) \left( \sum_{i,j} e^{i\mathbf{q}\cdot(\mathbf{r}_i-\mathbf{r}_j)} \right), \quad (2.3)$$

where we have used the orthogonality of our polarization vectors ( $\hat{e}_i \cdot \hat{e}_j = \delta_{i,j}$ ) to simplify the prefactor which is identified as the form factor  $F(\theta) = |f_1(\theta)|^2 + |f_2(\theta)|^2$ .

The remaining sum is identified as the structure factor

$$S(\mathbf{q} \neq \mathbf{0}) = (1/N) \langle \sum_{i,j} e^{i\mathbf{q}\cdot(\mathbf{r}_i-\mathbf{r}_j)} \rangle, \quad (2.4)$$

where the angle brackets indicate a configurational average. The configurational average is equivalent to a time average for most systems considered in this thesis. A few properties of the structure factor are worth recalling: the structure factor is isotropic ( $S(\mathbf{q}) = S(q)$ ) in a fluid; the structure factor  $S(q)$  is the Fourier transform of the pair correlation function and is thus intimately connected to the statistical mechanics and thermodynamics of a system; and  $S(q)$  is the same structure factor measured by X-ray and neutron scattering. The structure factor depends on the arrangement of particles within the sample, while the form factor depends on the ratio of the particle size to the photon wavelength as well as on the index of refraction

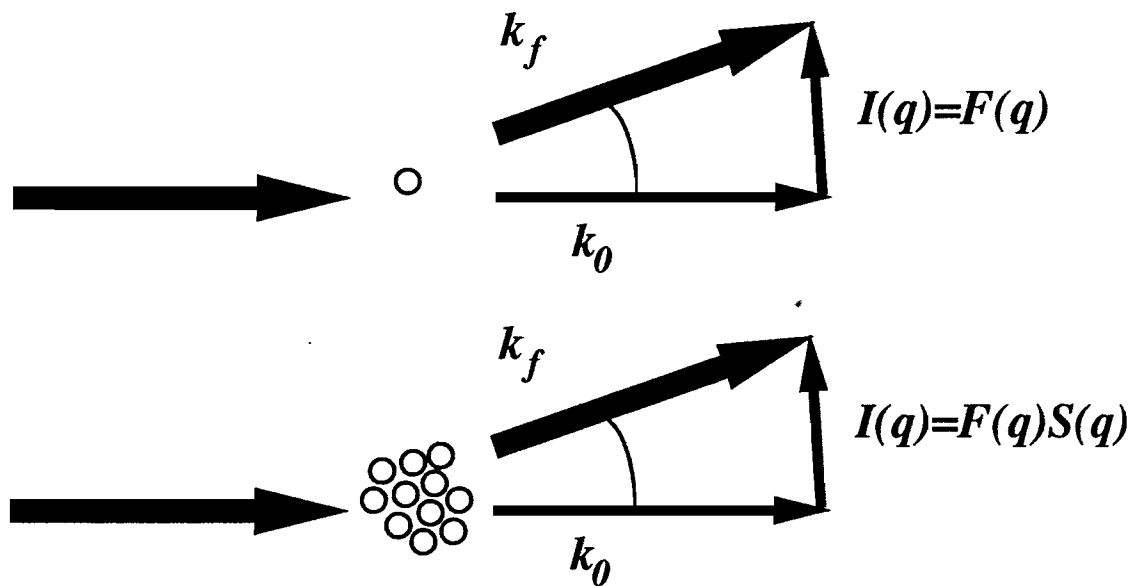


Figure 2.2: The connection between the scattering intensity, the form factor  $F(\theta)$  and the structure factor  $S(q)$ .

of the particle. With these newly introduced functions, we can rewrite (2.3) in the form,

$$I(q) = I_0 F(q, k_0 a) S(\mathbf{q}), \quad (2.5)$$

where  $a$  is the diameter of the scattering particle. The ratio of particle diameter to photon wavelength  $k_0 a$  is an important dimensionless number for scattering calculations.

## 2.2 Microscopic Picture of Diffuse Transport

We now turn our attention to scattering in opaque suspensions. Typically, a thin cell filled with a dense colloid is placed between a light source and a detector (Fig.1.1). Other common geometries include collecting light backscattered at some angle from the cell (Fig. 3.8) and using submerged optical fibers for both light injection and collection. In all of these geometries, photons scatter many times, through many different angles, typically taking tortuous paths which are very long compared to

the sample thickness (*e.g.* two centimeter long paths through a one millimeter thick cell).

Although the scattering problem is the same for multiple scattering as for single scattering, information is lost in multiple scattering because there is no way to determine the sequence of angles that photons are scattered through. As we move from one to many scattering events, we will see, however, that some useful information is preserved in multiple scattering. Our goal is to extract as much information as possible from the *statistical properties of multiply scattered light*.

The structure factor is a central part of all discussions of multiple scattering in this thesis. In the limit where the distance over which particle positions are correlated (the correlation length) is longer than the distance between scattering events, photon transport is often discussed in terms of photonic band structure [3]. In this thesis, we will assume that the distance between scattering events is long compared to the correlation length. When we discuss transmission experiments, we also assume that the sample is much thicker than the distance between scattering events. The question of how much thicker the sample must be has been addressed by a number of groups [4–6]. In addition, the distance between scattering events is assumed to be far longer than the photon wavelength. If the distance between scattering events is smaller than the photon wavelength, then different phenomena are expected, including a reduction in the speed of light [7] and the strong localization of photons [8].

In a multiple scattering experiment, after a photon scatters once it is still inside the sample where it will typically scatter many more times before escaping. We describe these multiple scattering events using the diffusion approximation for photon transport [9]. In the picture that describes the diffusion approximation, the multiply scattered photon is a random walker. Typically, the distribution of scattering events is generally sharply peaked at small scattering angles (Fig. 2.1). This peaked distribution pertains to relatively large particles with  $k_0 a > 1$ . The cross

section of smaller particles is so small that strong multiple scattering is difficult to achieve. In mixtures of particles, the larger ones tend to dominate scattering. After a single scattering event, the photon is not moving in a random direction, but is almost certainly moving nearly in the forward direction. The length scale on which the photon's direction is randomized is referred to as the *random walk step-length* or more formally as the *photon transport mean free pathlength* and denoted  $l^*$ . The distance between scattering events  $l$  is typically much shorter than the random walk step-length.

The expression for  $l^*$  in a single component mixture is now developed with an emphasis on the physical properties which determine it. In Chapter 4 we will revisit this discussion, identifying the changes necessary in order to calculate  $l^*$  in mixtures of different sized particles. In rigorous derivations of the diffusion approximation  $l^*$  arises naturally from electro-magnetic transport theory in random media [9]. As the rigorous treatment is quite technical, it is difficult to gain insight from it. Rather than repeating a formal treatment of transport theory, we will motivate the final result by analogy to polymers. In a polymer molecule, each monomer of length  $l$  has a bond which makes an angle  $\theta$  with the previous monomer. The persistence length of the polymer is  $l^*$ , which is given by the sum (see Figs. 2.3 and 2.4)

$$l^* = l \sum_{n=0}^{\infty} \langle \cos(\theta) \rangle^n. \quad (2.6)$$

This expression for the the persistence length relates the length over which the polymer bends significantly. The same expression relates the distance over which a photon's direction of propagation becomes randomized to the distance between scattering events. The infinite geometric sum in (2.6) simplifies to

$$\frac{l^*}{l} = 1/(1 - \langle \cos(\theta) \rangle). \quad (2.7)$$

The scattering angle is related to the scattering wave-vector by

$$q = 2k_0 \sin(\theta/2), \quad (2.8)$$

where  $k_0$  is calculated in the suspending medium (*i.e.*,  $k_0 = 2\pi n/\lambda$ ). Using this definition of  $q$ , we find

$$l^*/l = 2k_0^2/\langle q^2 \rangle_\Omega, \quad (2.9)$$

where the average  $\langle \rangle_\Omega$  is an average over scattering angles. Thus,  $l^*$  and  $l$  are connected through the average square scattering vector. To calculate this scattering wave vector, we must weight the scattering wave vectors by the intensity function ( $F(q)S(q)$ ) developed in section 2.1. The angular average is given by

$$\langle q^2 \rangle = \frac{\int_{4\pi} q^2 F(q)S(q)d\Omega}{\int_{4\pi} F(q)S(q)d\Omega}, \quad (2.10)$$

which is used to calculate the ratio of  $l^*$  to  $l$ ,

$$\frac{l^*}{l} = \frac{2k_0^2 \int_{4\pi} F(q)S(q)d\Omega}{\int_{4\pi} q^2 F(q)S(q)d\Omega}. \quad (2.11)$$

Ratios such as (2.11) often appear in the literature. To actually calculate  $l^*$  we also need to be very specific about the definitions of  $F(q)$ ,  $S(q)$ , and  $d\Omega$ . Ratios such as (2.11) are often simple to use because many factors of  $2\pi$  and  $k_0^2$  cancel, simplifying the calculation.

We now present the full expression for  $l^*$ . First, we change to a dimensionless Fourier variable  $y \equiv qa$  where  $a$  is the ball diameter [10]. In terms of the new variable, Eq. (2.11) reads

$$\frac{l^*}{l} = 2(k_0a)^2 \frac{\int_0^{2k_0a} F(y)S(y)ydy}{\int_0^{2k_0a} y^2 F(y)S(y)ydy}. \quad (2.12)$$

To calculate  $l^*$ , we must explicitly write out  $l$ , the mean free path. The mean free path is defined by,

$$l = 1/\rho\sigma_{sc}, \quad (2.13)$$

where  $\rho$  is the particle number density and  $\sigma_{sc}$  is the scattering cross section. At this point, a careful derivation of  $\sigma_{sc}$  is necessary to eliminate calculational ambiguity. In particular, we want to include the formalism of Mie theory in the expression for  $l^*$ .

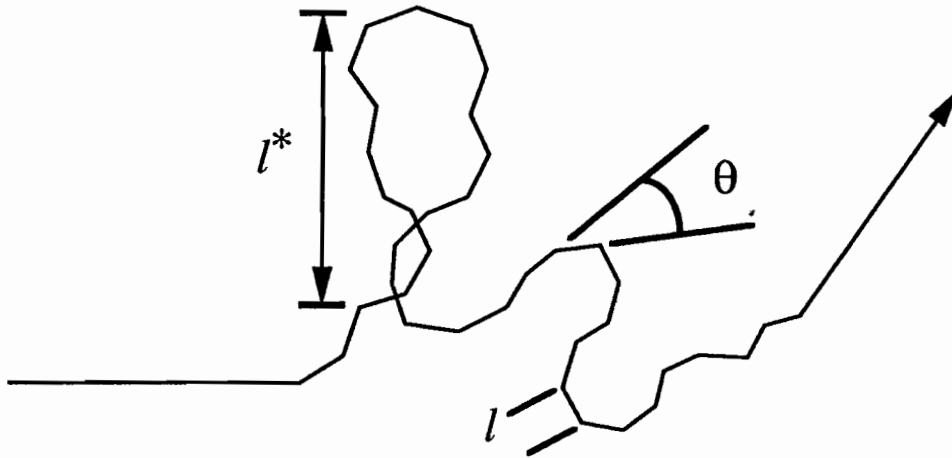


Figure 2.3: Microscopic picture of scattering and description of the quantities  $l^*$  and  $l$ .

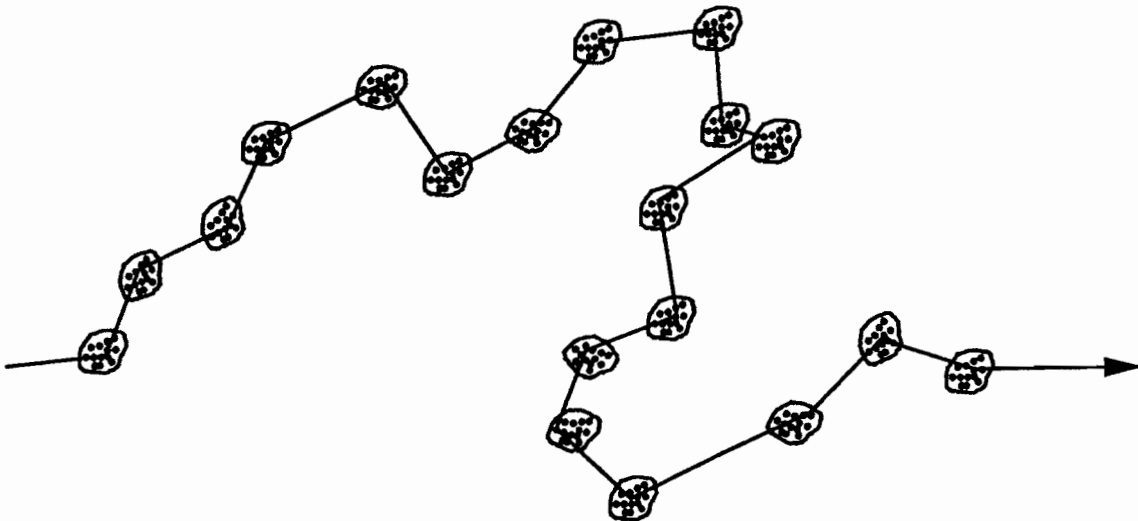


Figure 2.4: The inclusion of the structure factor  $S(y)$  in scattering accounts for the fact that a photon scatters from small correlated regions of the sample as depicted in this figure.

Mie theory describes scattering from dielectric spheres whose diameter is comparable to the photon wavelength.

We begin with the general definition of the differential cross section in Jackson (Jackson's Eq. (9.81)) [11]

$$\frac{d\sigma(\mathbf{n}, \vec{\epsilon}; \mathbf{n}_o, \vec{\epsilon}_o)}{d\Omega} = \frac{r^2 \frac{c}{8\pi} |\vec{\epsilon}^* \cdot \mathbf{E}_{sc}|^2}{\frac{c}{8\pi} |\vec{\epsilon}_o^* \cdot \mathbf{E}_{inc}|^2}. \quad (2.14)$$

Here the  $\mathbf{n}$ 's are unit vectors in the input and output propagation directions, and the  $\vec{\epsilon}$ 's are polarization vectors. A fairly complete description of Mie theory is found in Ishimaru's *Wave Propagation and Scattering in Random Media* volume 1. In Mie theory, the fields scattered by a small particle are:

$$\begin{aligned} E_\phi &= -\frac{ie^{ikr}}{kr} E_o \mathcal{S}_1(\theta) \sin \phi, \\ E_\theta &= \frac{ie^{ikr}}{kr} E_o \mathcal{S}_2(\theta) \cos \phi, \\ \mathcal{S}_1(\theta) &= \sum_{n=1, \infty} \frac{(2n+1)}{n(n+1)} [a_n \pi_n(\cos \theta) + b_n \tau_n(\cos \theta)], \\ &\text{and} \end{aligned}$$

$$\mathcal{S}_2(\theta) = \sum_{n=1, \infty} \frac{(2n+1)}{n(n+1)} [a_n \tau_n(\cos \theta) + b_n \pi_n(\cos \theta)], \quad (2.15)$$

where  $\pi_n$  and  $\tau_n$  are functions related to Legendre polynomials, the  $a_n$  and  $b_n$ 's are Mie scattering coefficients, and the field is resolved along the  $\theta$  and  $\phi$  directions as described in Fig. 2.5. Comparing the scattered fields to the definition of the differential cross section, we find

$$\frac{d\sigma}{d\Omega} = \frac{1}{2k_0^2} |\mathcal{S}_1(\theta)|^2 + \frac{1}{2k_0^2} |\mathcal{S}_2(\theta)|^2. \quad (2.16)$$

We are averaging over initial polarizations and then adding final polarizations. By comparing this differential cross section with the expression for the scattered intensity and the form factor in Eq. (2.3), we find the formal connection between the partial cross section and the form factor

$$\frac{d\sigma}{d\Omega} = \frac{1}{k_0^2} F(\theta). \quad (2.17)$$

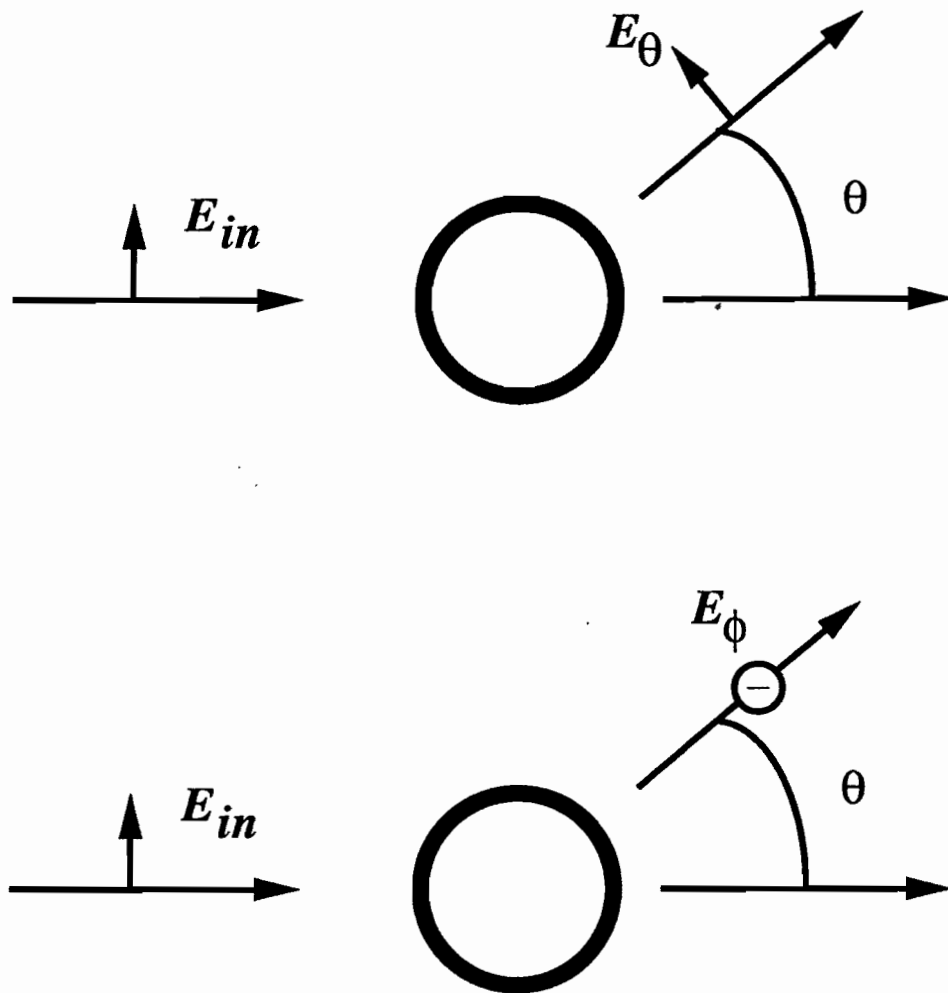


Figure 2.5: Mie scattering geometry.

The final detail of the scattering formalism is the technique for averaging over polarizations. The maxim taught in Quantum Mechanics and Electromagnetism is “average over input polarizations, sum over output polarizations.” This is because the output polarizations are physically distinguishable, and the intensity of each output polarization is thus added. Input polarizations, however, are not distinguishable at the detector. Therefore, we average over input polarization

$$\frac{d\sigma}{d\Omega} = \frac{\int_0^{2\pi} \frac{d\sigma(\vec{\epsilon}_{in})}{d\Omega} d\phi}{\int_0^{2\pi} d\phi}. \quad (2.18)$$

The polarization dependent part of the cross section is  $|\mathcal{S}_i(\theta) \frac{\sin(\phi)}{\cos(\phi)}|^2$ . The averages over  $\sin^2 \phi$  and  $\cos^2 \phi$  give the factor of 1/2 found in (2.16) .

We now unambiguously write the scattering cross section

$$\sigma_{sc} = \frac{1}{k_0^2} \int_{4\pi} F(\theta) S_{k_0 a}(\theta) d\Omega, \quad (2.19)$$

where  $S_{k_0 a}(\theta)$  is  $S(y)$  from (2.12). Before using  $\sigma_{sc}$  to calculate  $l^*$  using (2.12) we will rewrite  $\sigma_{sc}$  in terms of the dimensionless Fourier variable  $y = qa$  [10].

$$\sigma_{sc} = \frac{2\pi}{k_0^2 (k_0 a)^2} \int_0^{2k_0 a} F(y) S(y) y dy. \quad (2.20)$$

The factor of  $2\pi$  is a result of the integral over  $\phi$ , and the extra factor of  $(k_0 a)^2$  is a byproduct of the change of variables.

The final ingredient needed to calculate  $l^*$  is  $\rho$ , the number density

$$\rho = \frac{\phi}{\frac{\pi}{6} a^3}, \quad (2.21)$$

where  $\phi$  is the volume fraction of the colloidal particles. Using the number density (2.21) and the scattering cross section (2.20), we rewrite  $l^*$  (2.12)

$$\begin{aligned} l^* &= \frac{(k_0 a)^6 a}{6\phi \int_0^{2k_0 a} y^2 F(y) S(y) y dy} \\ &= \frac{(k_0 a)^4 k_0^2}{\pi \rho \int_0^{2k_0 a} y^2 F(y) S(y) y dy}. \end{aligned} \quad (2.22)$$

The random walk step-length is an *average* over the structure factor. Not only is knowledge of  $S(y)$  necessary for calculations of  $l^*$ , but our understanding of structure may be tested by measuring  $l^*$ .

## 2.3 Random Walks

We have seen that a photon in a dense medium scatters many times, and that its path may be characterized by two lengths, a distance between scattering events  $l$  and a so-called random walk step-length (the transport mean free path length)  $l^*$

over which the direction of propagation becomes randomized. In this section, we will quickly state a few well known properties of random walks. More complete discussions are available at the textbook level (*e.g.*, Reif [12] Chapters 1 and 12).

For a random walk beginning at the origin in one dimension, the average position after  $n$  steps  $\bar{x}$  is defined by

$$\bar{x} = \sum_x xP(x, n), \quad (2.23)$$

where  $x$  takes integer values, and  $P(x, n)$  is the probability that the walker is at position  $x$  after  $n$  steps. This average is zero because steps in each direction are equally likely,  $P(x, n) = P(-x, n)$ . The average mean square displacement  $\overline{x^2}$ , however, is not zero. To calculate the average squared displacement, we need to know  $P(x, n)$ . The probability  $P(x, n)$  is the probability of taking  $(n+x)/2$  consecutive steps in the  $+$  direction followed by  $(n-x)/2$  consecutive steps in the  $-$  direction multiplied by the total number of permutations of this particular sequence. The result is

$$P(x, n) = \binom{n}{(n+x)/2} \left(\frac{1}{2}\right)^{(n+x)/2} \left(\frac{1}{2}\right)^{(n-x)/2}, \quad (2.24)$$

where the notation  $\binom{n}{m}$  is a count of the number of ways in which one can choose  $m$  steps in the positive direction from a set of  $n$  steps

$$\binom{n}{m} = \frac{n!}{m!(n-m)!}. \quad (2.25)$$

In the continuum limit, where  $n$  is very large, the probability distribution (2.24) approaches

$$P(x, n) = \frac{1}{\sqrt{2\pi n}} e^{-x^2/2}. \quad (2.26)$$

We are concerned with two properties of this distribution: (i) the displacement  $\langle x^2(n) \rangle^{1/2}$  is proportional to the *square root* of the number of steps, and (ii) the average number of steps taken by those random walkers which reach a particular point along the walk  $x_0$  is proportional to the *square* of the number of direct steps to that point.

Examination of random walks in the continuum limit leads to the diffusion equation. This is seen by considering a set of non-interacting random walkers in one dimension. If the number of walkers at each point  $i$  after  $n$  steps is  $m_i(n)$ , then the number after the next step  $m_i(n+1)$  is calculated by considering the difference between the number of walkers that left point  $i$  and the number that arrived at point  $i$ . Since half of the walkers at each point move in each direction, the temporal change in  $m_i(n)$  is

$$m_i(n+1) - m_i(n) = \left(\frac{1}{2}\right)(m_{i-1}(n) - m_i(n)) + \left(\frac{1}{2}\right)(m_{i+1}(n) - m_i(n)) \quad (2.27)$$

$$= \left(\frac{1}{2}\right)[m_{i-1}(n) - 2m_i(n) + m_{i+1}(n)]. \quad (2.28)$$

The second line is the numerical expression for the second spatial derivative. Setting  $t = n\Delta t$  and considering the continuum limit where both  $\Delta t$  and the spatial separation between points  $i$  and  $i+1$  are small, this discrete expression becomes

$$\partial_t \rho(x, t) = \frac{\Delta x^2}{\Delta t} \frac{\partial^2 \rho(x, t)}{\partial x^2}, \quad (2.29)$$

where  $\rho$  is the number density of walkers. This is the well studied *diffusion equation*. In this example we will identify  $\Delta x^2/\Delta t$  as the diffusion coefficient.

In this thesis we will discuss two types of diffusion, the diffusion of light in a highly multiply scattering sample and the diffusion of particles undergoing Brownian motion.

## 2.4 The Diffusion Equation

Random walks and the diffusion equation are intimately connected. In this section we will write the diffusion equation for photon transport in multiply scattering materials. A random walker which takes steps of length  $l^*$  obeys the diffusion equation

$$\partial_t U(\mathbf{r}, t) = \frac{v l^*}{d} \nabla^2 U(\mathbf{r}, t), \quad (2.30)$$

where  $d$  is the dimension of the space in which the walk takes place,  $v$  is the ballistic velocity or the velocity of the walker between steps, and  $U$  is the energy density of the photon field, which is proportional to the number density of photons. Equation (2.30) defines the photon diffusion coefficient  $D_\gamma = (vl^*/3)$ , where  $v$  is the speed of light in the solvent, which is the speed of light in vacuum divided by the solvent's index of refraction  $n_s$  (for limits on the validity of calculating the speed of light this way, see Ref. [7]). The index of refraction  $n_s$  is well known for many common solvents, including water, which is exclusively used in this thesis. The only parameter of the photon diffusion equation

$$\partial_t U(\mathbf{r}, t) = D_\gamma \nabla^2 U(\mathbf{r}, t), \quad (2.31)$$

is the random walk step-length  $l^*$  which depends on the particle form factor and the interparticle structure factor.

## 2.5 Measuring $l^*$

Our first application of the photon diffusion equation will be to find a simple way to measure  $l^*$ . Since  $l^*$  is the only parameter in (2.31), many calculated results of the diffusion equation will be  $l^*$  dependent. There are a number of different approaches which can be used successfully to measure  $l^*$ . The simplest and one of the most direct methods is to monitor the transmission coefficient of a slab of scattering material.

The transmission  $T$  through a non-absorbing slab of infinite transverse extent and thickness  $L$  is nearly proportional to the photon random walk step-length  $l^*$

$$T = \left(\frac{5}{3}\right) \frac{l^*}{L} [1 + (4/3)(l^*/L)]^{-1}. \quad (2.32)$$

In this section we present a simple derivation of (2.32). The transmission coefficient  $T$  is independent of the profile of the input beam for a slab of infinite transverse extent because it depends only on propagation in one direction and is thus insensitive to photon displacements along the surface of the cell. We choose to solve the

simplest problem, the one dimensional photon diffusion problem, and then use this solution to compute the flux at both faces. The transmission is then calculated by dividing the transmitted flux by the total flux. There are many other derivations of (2.32) [9, 13–15].

Within the diffusion approximation, in the absence of absorption, photon transport is described by Eq. (2.31). We consider the steady-state, one dimensional problem pictured in Fig. 2.6

$$\partial_z^2 U = 0, \quad (2.33)$$

solutions of which are linear in  $z$ . We further assume that the incident flux appears as a diffuse source at some distance  $\alpha l^*$  inside the sample,  $\alpha \approx 1$ . For convenience we choose  $U(\alpha l^*) = 2U_0$ . The solution to the diffusion equation is of the form

$$U = \begin{cases} A_l + B_l z & \text{for } z < \alpha l^* \\ A_r + B_r z & \text{for } z > \alpha l^* . \end{cases} \quad (2.34)$$

To solve for the A and B coefficients we need the correct boundary conditions.

The boundary conditions require that there be no diffuse flux into the sample from the outside. Thus, the diffuse flux at the boundary into the sample is only the reflected outgoing flux. The net current  $\mathbf{J}$  given by Fick's law can be considered as the sum of the currents in each direction (Fig. 2.7) [9, 16]

$$\mathbf{J} \cdot \hat{z} = J_+ - J_- = -D_\gamma \hat{z} \cdot \nabla U . \quad (2.35)$$

The current in each direction has both an isotropic component and a part which depends on the gradient of  $U$  [17]

$$J_\pm = \frac{Uc}{4} \mp \frac{D_\gamma}{2} \partial_z U . \quad (2.36)$$

In terms of this current, the boundary conditions are

$$J_+(0) = RJ_-(0) \quad (2.37)$$

$$J_-(L) = RJ_+(L) , \quad (2.38)$$

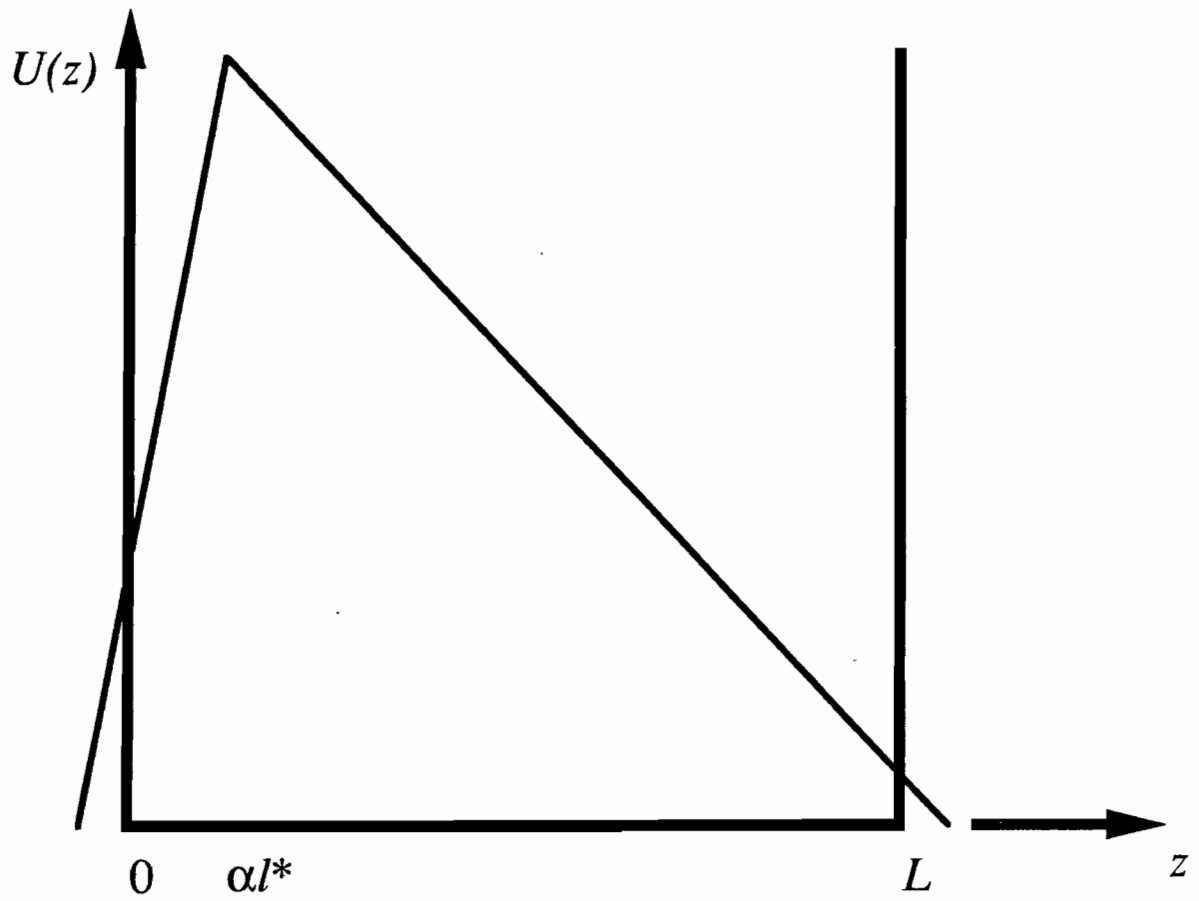


Figure 2.6: Distribution of diffuse energy density in a slab under steady illumination.

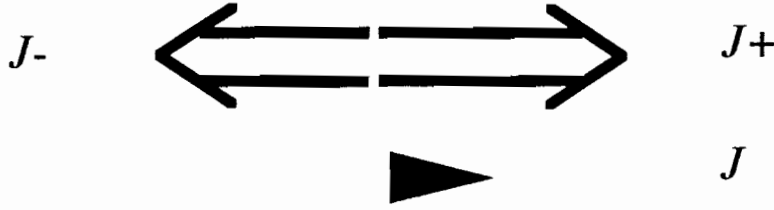


Figure 2.7: The flux is largely isotropic. There is a small anisotropy, which is the net flux. The flux in each direction must satisfy the boundary conditions of the diffusion equation.

where  $R$  is the diffuse reflection coefficient. These boundary conditions enforce the requirement that there is no diffuse flux directed into the sample at each wall, except for reflected outgoing flux. The calculation of the diffuse reflection coefficient has been carefully described in Refs. [18] and [4]. It is obtained by averaging over the angle dependent reflection coefficient and summing over multiple reflections when the medium is bounded by a cell wall of finite thickness. The final boundary condition is that  $U$  has no discontinuity at  $z = \alpha l^*$ . We now have three boundary conditions for the four coefficients. We arbitrarily set  $A_l$  to  $U_0$  and find

$$U = U_0 \begin{cases} (1 + z/hl^*) & \text{for } z < \alpha l^* \\ \frac{1+\alpha/h}{L+(h-\alpha)l^*}(L + hl^* - z) & \text{for } z > \alpha l^* \end{cases}, \quad (2.39)$$

where  $h = (2/3)(1+R)/(1-R)$ . With this solution for the energy density, the transmission coefficient is readily obtained using the transmitted and the backscattered flux.

The total transmission depends on the directional fluxes at both sides of the sample

$$T = \frac{J_+(L)}{J_+(L) + J_-(0)}, \quad (2.40)$$

which is evaluated using (2.36), giving:

$$T = \left(\frac{l^*}{L}\right) \frac{\frac{2}{3} \left(\frac{1+R}{1-R}\right) + \alpha}{1 + \frac{4}{3} \left(\frac{1+R}{1-R}\right) \frac{l^*}{L}}. \quad (2.41)$$

The factor of  $5/3$  in (2.32) is obtained by setting  $R$  to 0 and  $\alpha$  to 1. It depends on both the physical boundary conditions and  $\alpha$ , which is an artifact of this simple

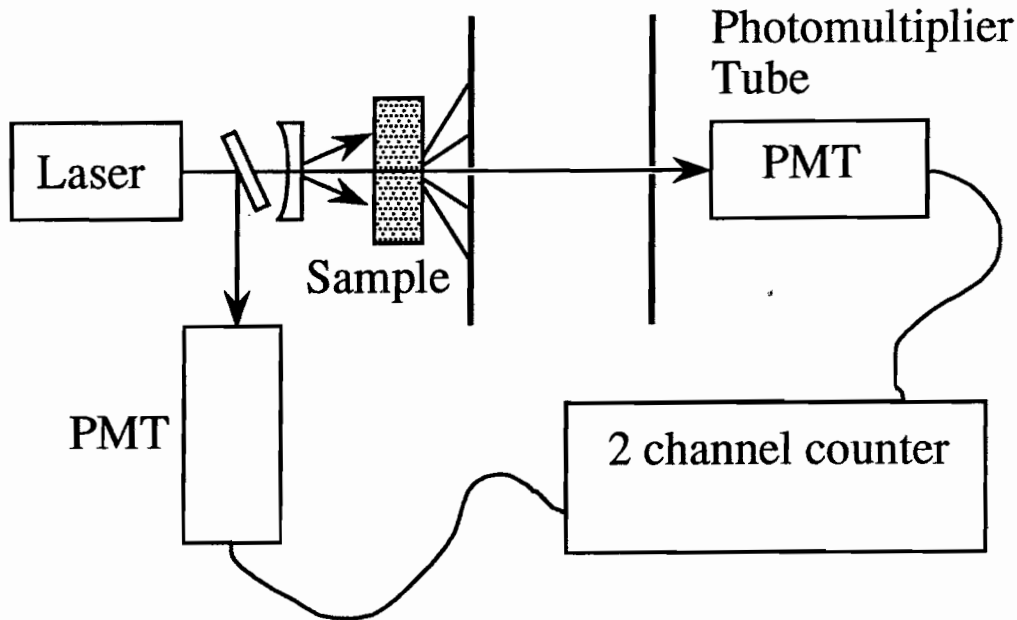


Figure 2.8: Apparatus for measuring transmission  $T$ .

model. The denominator, however, depends only on the boundary conditions. We always measure the ratio of the transmission of different samples. This ratio is insensitive to the value of the prefactor in Eq. (2.32).

If the absorption length  $l_a$  is of order  $L^2/l^*$  or less, this result is multiplied by a factor of  $\beta/\sinh(\beta)$ , where  $\beta$  is  $\sqrt{3L^2/l^*l_a}$  [19]. In this thesis we ignore absorption since  $l_a$  is on the order of a few meters and average pathlengths, which are of order  $L^2/l^*$ , are always less than 15 cm.

We measure optical transmission by comparing the intensity transmitted through the sample into a photomultiplier tube to the intensity collected from the beam splitter in Fig. 2.8. The resulting ratio drifts when the laser's spatial mode shifts during the course of an experiment. To normalize for that drift, the transmission of a standard cell is measured repeatedly. Thus, we are only able to measure the ratio of the transmission of the sample cell to that of a standard cell. Repeated measurements indicate that transmission measurements obtained in this apparatus fluctuate by roughly 4%. We have tested the validity of these results by varying sample thickness [4]. The transmission coefficient derived from the diffusion approximation is valid

for samples which are more than roughly  $10 l^*$  thick. In samples with a larger ratio of  $l^*$  to  $l$ , there are more scattering events per “random walk step.” Thus, the diffuse result (2.41) applies to significantly thinner samples.

## 2.6 Time Dependent Transport

Our second application of the diffusion equation (2.31) is the problem of the time dependence of the transmission of a short pulse through a slab of infinite transverse extent. By using the full time dependent diffusion equation, the transmitted intensity  $I(t)$  can be calculated. Most of our discussions focus not on the time spent by a photon in the sample, but on the distance it travels through the sample, so that we will focus on the probability distribution for paths of length  $s$ ,  $P(s) \propto I(t = s/(c/n))$ . Rather than repeating derivations of  $P(s)$ , we will focus on some of its properties.

To calculate  $P(s)$ , we employ a standard reference for mathematical solutions of the diffusion Eq. (2.30) [20]. In Fig. 2.9a,  $P(s)$  is displayed for a sample  $L$  thick with  $L/l^* = 20$ . The important properties of this graph are that (1) the transmitted pulse rises much faster than it falls, (2) the decay is exponential, and (3) the centroid of the pulse scales with  $L^2/l^*$ . This last point is demonstrated in Fig. 2.9b, a graph of the average pathlength against sample thickness.

The formula used to calculate the curves in Fig. 2.9 is obtained from Ref. [20]. In particular, the result is

$$I(t) = 2 \sum_{n=1, \infty} \left( e^{-D\alpha_n^2 t} \right) \frac{\alpha_n \cos(\alpha_n z_0) + h^{-1} \sin(\alpha_n z_0)}{(\alpha_n^2 + h^{-2})L + 2/h} (\alpha_n \cos(\alpha_n L) + h \sin(\alpha_n L)), \quad (2.42)$$

where  $I(t)$  is proportional to  $P(s = t/c)$ ,  $h = (2/3)l^*(1 + R)/(1 - R)$  is the extrapolation length,  $z_0$  is the point at which energy is deposited (roughly at  $z = l^*$ ),  $L$  is the cell thickness, and the  $\alpha_n$ 's are solutions to

$$\tan(\alpha L) = \frac{2\alpha/h}{\alpha^2 - h^{-2}}. \quad (2.43)$$

This is a transcendental equation with a large set of solutions. To avoid numerical difficulties, separate the tangent into sine and cosine before solving.

It is possible to measure  $l^*$  by measuring and fitting to  $P(s)$  [21], instead of relying on the diffusion equation. This method is experimentally much more complex than the simple transmission measurement described in Section 2.5.

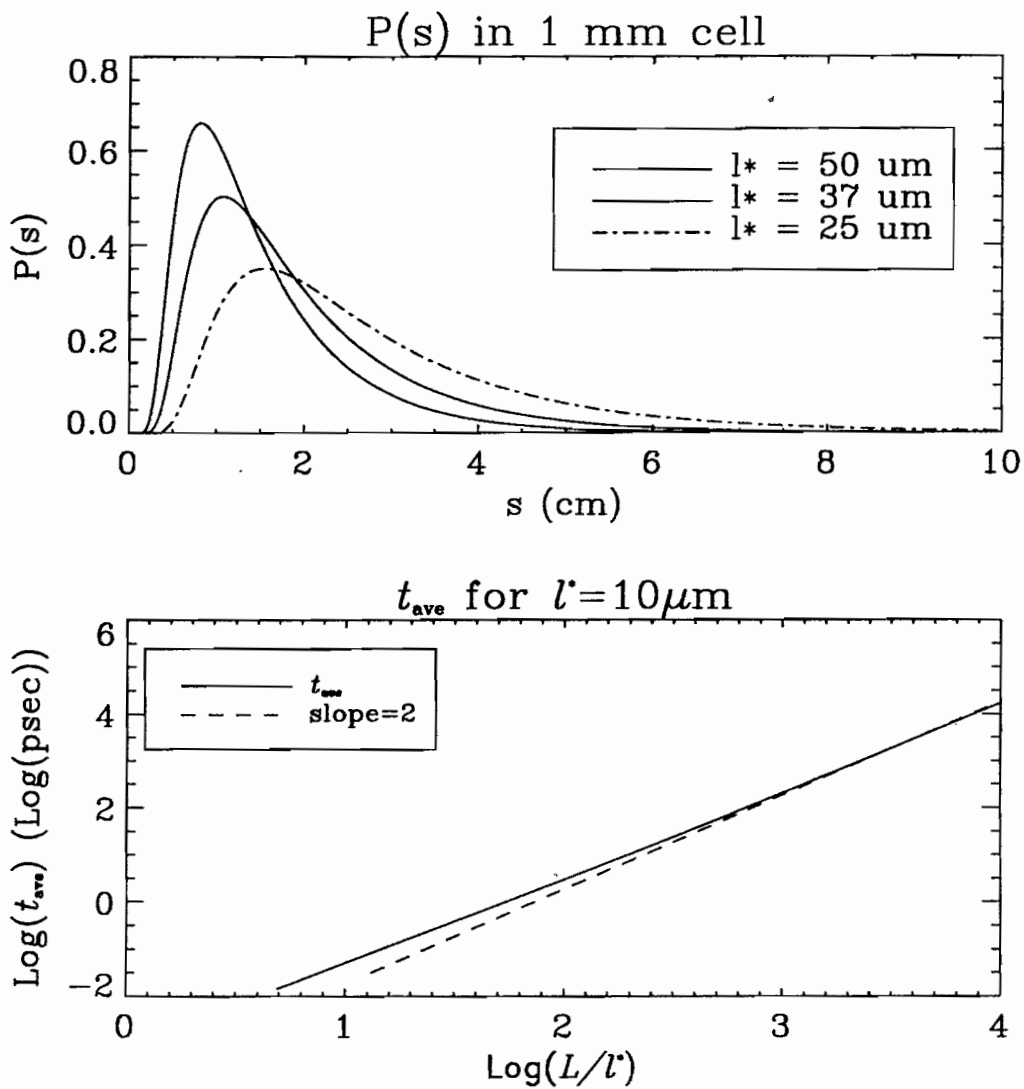


Figure 2.9: (top) Time dependence of the pulse transmitted through a sample with different values of  $l^*$ , and  $L = 1$  mm. (bottom) Scaling between thickness and average time. In this case,  $l^* = 10 \mu\text{m}$  and the thickness is varied. This figure shows the scaling of the average transit time with the sample thickness squared. Calculations in this figure are based on Sections 3.9 and 3.10 of Ref. [20].

# Bibliography

- [1] P. Pieranski, *Colloidal Crystals*, Contemp. Phys. **24**, 25 (1983).
- [2] P. Pieranski and B. Pansu, *Microspectroscopy*, J. de Phys. **46-C3**, c3 (1985).
- [3] E. Yablonovitch, *Photonic band-gap structures*, J. Opt. Soc. Am. B **10**, 283 (1993).
- [4] P. D. Kaplan, M. H. Kao, A. G. Yodh, and D. J. Pine, *Geometric constraints for the design of diffusing-wave spectroscopy experiments*, Appl. Optics **32**, 3828 (1993). *Eng.*
- [5] K. M. Yoo, F. Liu, and R. R. Alfano, *When Does the Diffusion Approximation Fail to Describe Photon Transport in Random Media?*, Phys. Rev. Lett. **64**, 2647 (1990).
- [6] K. M. Yoo, F. Liu, and R. R. Alfano, *Errata: When Does the Diffusion Approximation Fail to Describe Photon Transport in Random Media?*, Phys. Rev. Lett. **65**, 2210 (1990).
- [7] M. P. van Albada, B. A. van Tiggelen, A. Lagendijk, and A. Tip, *Speed of Propagation of Classical Waves in Strongly Scattering Media*, Phys. Rev. Lett. **66**, 3132 (1991).
- [8] P. W. Anderson, *The Question of Classical Localization A Theory of White Paint?*, Philos. Mag. B **52**, 505 (1985).

[9] A. Ishimaru, in *Wave Propagation and Scattering in Random Media* (Academic Press, New York, 1978).

[10] The change of integration variables from  $d\Omega$  to  $ydy$  begins by noting that  $d\Omega = \sin(\theta)d\theta d\phi$ . Using the trigonometric relation

$$\sin(\theta) = 2 \sin(\theta/2) \cos(\theta/2) \quad (2.44)$$

and the definition of the wave-vector (2.8) we arrive at

$$d\Omega = \frac{1}{k_0^2} q dq d\phi. \quad (2.45)$$

Integrating over the azimuthal variable and multiplying by  $a/a$  twice we find

$$d\Omega \longrightarrow \frac{2\pi}{(k_0 a)^2} y dy. \quad (2.46)$$

[11] J. D. Jackson, *Classical Electrodynamics* (John Wiley and Sons, New York, 1975).

[12] F. Reif, *Fundamentals of statistical and thermal physics* (McGraw-Hill, New York, 1965).

[13] A. Lagendijk, R. Vreeker, and P. DeVries, *Influence of Internal Reflection on Diffusive Transport in Strongly Scattering Media*, Phys. Lett. A **136**, 81 (1989).

[14] A. Z. Genack, N. Garcia, and W. Polkosnik, *Long-range intensity correlation and the approach to localization*, Waves in random media **3**, s57 (1991).

[15] C. P. Gonatas *et al.*, *Determination of optical mean free path from pulse propagation and backscattering*, submitted Phys. Rev. E **XX**, XXX (1993).

[16] D. J. Pine, D. A. Weitz, J. X. Zhu, and E. Herbolzheimer, *Diffusing-Wave Spectroscopy: Dynamic Light Scattering in the Multiple Scattering Limit*, J. Phys. France **51**, 2101 (1990).

- [17] S. Glasstone and M. C. Edlund, in *the Elements of Nuclear Reactor Theory* (D. van Nostrand Co., Princeton N.J., 1952).
- [18] J. X. Zhu, D. J. Pine, and D. A. Weitz, *Internal reflection of diffusive light in random media*, Phys. Rev. A **44**, 3948 (1991).
- [19] D. J. Durian, D. A. Weitz, and D. J. Pine, *Multiple Light-scattering Probes of Foam Structure and Dynamics*, Science **252**, 686 (1991).
- [20] H. S. Carslaw and J. C. Jaeger, *Conduction of Heat in Solids, Second Edition* (Oxford University Press, New York, 1959).
- [21] A. G. Yodh, P. D. Kaplan, and D. J. Pine, *Pulsed Diffusing-Wave Spectroscopy: High Resolution through Nonlinear Optical Gating*, Phys. Rev. B **42**, 4744 (1990).

# Chapter 3

## Photon transport in dynamic media: diffusing-wave spectroscopy

### 3.1 Introduction

Diffusing-wave spectroscopy (DWS) is a probe of the *dynamics of scatterers*. The connection between light scattering and dynamics is made by considering fluctuations in the *phase* of scattered photons; the phase was ignored in Chapter 2. There have been a number of careful reviews of the basic theory of DWS both in the literature [1–4] and in thesis form [5–7]. This chapter is intended to be a concise presentation of basic results that will be useful in later chapters.

We will work within a simple conceptual framework that allows us to understand DWS well enough for its use in this thesis without recourse to Green’s functions. If we treat the scattering of a photon through a tortuous path within the sample as the elementary scattering event rather than focusing on scattering from individual particles, then we find that DWS is formally similar to the single scattering technique

quasi-elastic light scattering (QELS). After a review of QELS, which lays the foundation for the connection between temporal fluctuations in the intensity of scattered light and particle motion, we will consider the effects of multiple scattering, arriving at the basic results of DWS. Finally, we will discuss some of the experimental details and the nuances of DWS measurements.

## 3.2 Dynamic Single Scattering

The technique of quasi-elastic light scattering (QELS) is used to measure the dynamic properties of particles in systems where light is singly scattered. In QELS (see Fig. 3.1) a small volume of the sample is imaged onto a detector. The intensity of the collected light depends on the interference from light scattered off of different particles. As these particles move relative to each other, the interference condition changes. It is the statistics of the changing interference condition that is related to the motion of the particles.

The first step in relating fluctuations of the scattered field to the motion of the particles is to calculate the electric field at the detector. The detected field is the sum of the field scattered from each particle

$$\mathbf{E}_{sc} = (E_o/\sqrt{4\pi R^2})(f_1(\theta)\hat{e}_1 + f_2(\theta)\hat{e}_2)e^{i\mathbf{k}_f \cdot \mathbf{R}} \left( \sum_i e^{i\mathbf{q} \cdot \mathbf{r}_i} \right), \quad (3.1)$$

where the amplitude  $f$  is related to the form factor  $F = f^* f$ .

To study particle dynamics we need access to the time dependence of  $E_{sc}(t)$ . For particles whose motion is generated by statistical, random forces, the scattered field fluctuates randomly. Rather than examining the field itself, we turn to statistical properties of the field's fluctuations. In particular, we use the temporal field autocorrelation function, which is defined by

$$g_1(\tau) \equiv \frac{\langle E(\tau)E^*(0) \rangle}{|E|^2} = \left\langle \sum_{i,j=1,N} e^{i\mathbf{q} \cdot (\mathbf{r}_i(\tau) - \mathbf{r}_j(0))} \right\rangle, \quad (3.2)$$

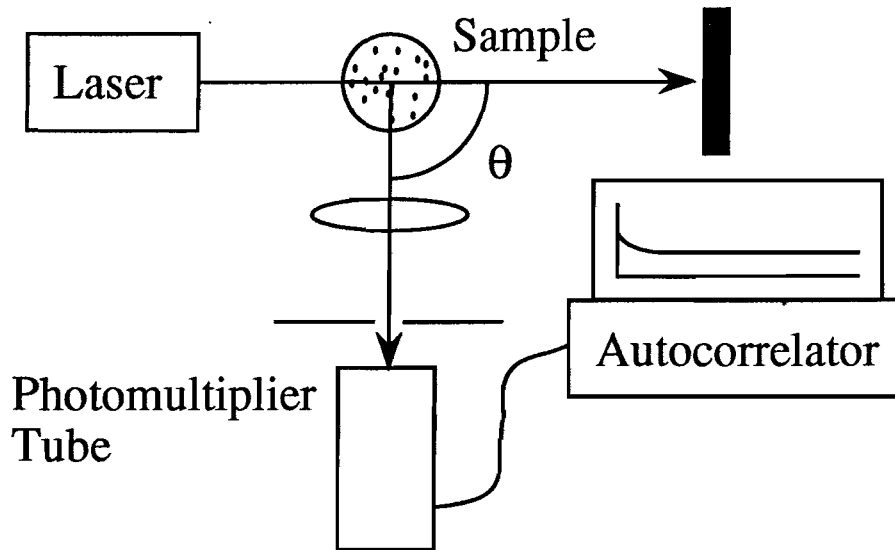


Figure 3.1: Quasi-elastic light scattering apparatus. The autocorrelation function of singly scattered light is a simple exponential.

where the  $\langle \rangle$  brackets denote an ensemble average. In sufficiently dilute systems, there is no correlation between the motion of different particles, and all terms in (3.2) with  $i \neq j$  are 0. In a monodisperse system of  $N$  particles, all terms with  $i = j$  are equivalent, and the final expression

$$g_1(\tau) = NF(q, k_0 a) \langle e^{i\mathbf{q} \cdot \Delta \mathbf{r}(\tau)} \rangle \quad (3.3)$$

is a function of the particle displacement  $\Delta \mathbf{r}(\tau) \equiv \mathbf{r}(\tau) - \mathbf{r}(0)$ . Evaluating the average in (3.3) requires knowledge of the time evolution of  $\Delta \mathbf{r}(\tau)$ . The motion of small particles in a viscous fluid is dominated by thermal fluctuations and is called Brownian motion. The subject of Brownian motion has received a great deal of study [8,9] and will be only briefly discussed here (see also the discussion of random walks in Section 2.3). The displacement of a Brownian particle free to wander in three dimensions over sufficiently long times is described by the probability distribution

$$P(|\Delta \mathbf{r}(\tau)|) = \frac{1}{(4\pi D\tau)^{3/2}} e^{-|\Delta \mathbf{r}(\tau)|^2/4D\tau}, \quad (3.4)$$

where the diffusion coefficient  $D$  is generally the Einstein diffusion coefficient  $D = k_B T / 6\pi\eta(a/2)$ . In any random walk, there is a time scale on which motion is ballistic

$(\Delta r^2 \propto \tau^2)$  rather than diffusive ( $\Delta r^2 \propto \tau$ ). In Brownian systems, this time scale is set by the *hydrodynamic* time  $\tau_H = \rho a^2 / 4\eta$ , where  $a$  is the particle diameter,  $\eta$  is the fluid viscosity, and  $\rho$  is fluid density. The hydrodynamic time is the time taken for vorticity in the fluid to diffuse around the particle. Diffusive motion is well established over the course of  $100\tau_H$ 's; in this thesis, we focus on time scales longer than  $100\tau_H$ 's. The transition to diffusive motion is discussed, for example, in Refs. [10,11]. After integrating over the probability distribution (3.4) to evaluate the average phase shift in (3.3), we arrive at the central result of QELS

$$g_1(\tau) = \exp(-q^2 D\tau) = \exp(-q^2 \langle \Delta \mathbf{r}(\tau) \rangle^2 / 6). \quad (3.5)$$

The simple exponential decay of the QELS correlation function is extremely useful for measuring diffusion coefficients and, through the Einstein relation, for measuring the size of small particles [12–14].

In the next two sections, the single scattering correlation function will be extended to multiple scattering experiments. Later in the text (sections 3.6 and 4.3), we will reexamine the development of QELS (3.5), introducing interparticle order and hydrodynamic interactions which become significant when the suspended particles are not dilute.

### 3.3 Multiple Scattering

We will now discuss multiply scattered photons in terms of the *paths* that they take through the sample rather than focusing on the individual particles that they scatter off of along their paths (see Fig. 3.2). In this section, paths will be discussed with a view towards calculating the correlation function for photons that take a particular path. The final result relies on and strongly resembles the QELS result, Eq. (3.5).

A path is a sequential list of particles from which a photon may scatter. Each path is characterized by a total length  $s(\{\mathbf{r}_i(t)\})$ , which fluctuates with the particles' positions. The fluctuation in pathlength results in fluctuations in the phase and

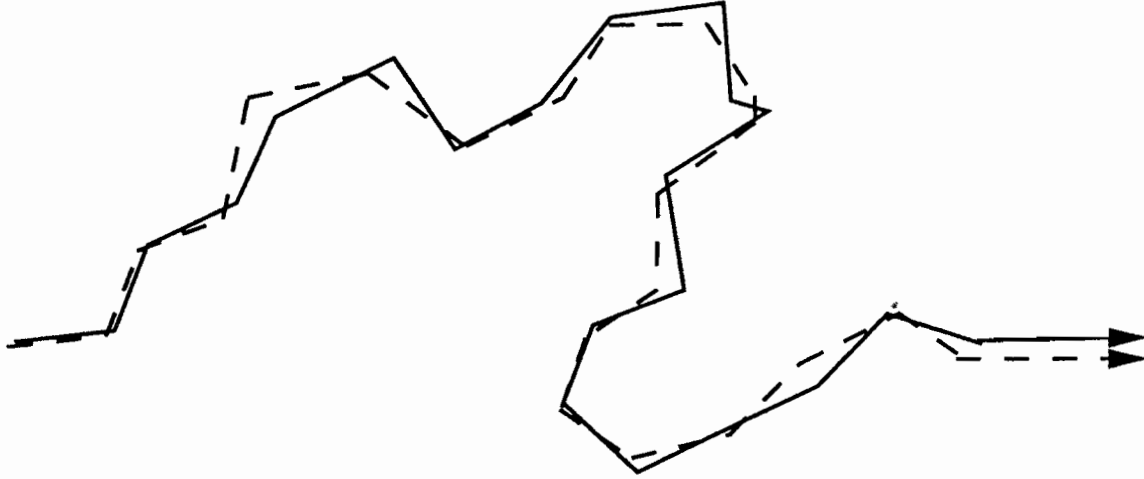


Figure 3.2: In DWS, photons scatter through a *path* that fluctuates in total length as the individual particles along the path move.

amplitude of the scattered photon. The phase accumulated by a photon which travels through a path with  $N$  scattering events is  $\sum_i \mathbf{k}_i \cdot (\mathbf{r}_i - \mathbf{r}_{i-1})$ . After grouping terms in this sum in terms of  $\mathbf{r}_i$  rather than  $\mathbf{k}_i$ , we write the accumulated phase as

$$\theta_N(t) = \mathbf{q}_1 \cdot \mathbf{r}_1(t) + \mathbf{q}_2 \cdot \mathbf{r}_2(t) + \mathbf{q}_3 \cdot \mathbf{r}_3(t) + \cdots + \mathbf{q}_N \cdot \mathbf{r}_N(t), \quad (3.6)$$

where the scattering wave vectors are described in Fig. 3.3. The field correlation function for photons scattering through such paths is obtained by multiplying the field at time 0 by the field at time  $\tau$ , just as for QELS (equation (3.2)). The result is:

$$g_1^{(N)}(\tau) = \langle \exp [i(\theta_N(\tau) - \theta_N(0))] \rangle \quad (3.7)$$

$$= \langle \prod_i \exp [i\mathbf{q}_i \cdot (\mathbf{r}_i(\tau) - \mathbf{r}_i(0))] \rangle. \quad (3.8)$$

When  $N$  is large, and  $N$  is typically  $\sim 10^2 - 10^4$ , we treat each scattering event as being both statistically independent and equivalent. This is a good approximation even if the motion of a particle is correlated with that of its nearest neighbors because the distance between scattering events is typically long compared to the distance between nearest neighbors. The correlation function for a path with  $N$  scattering

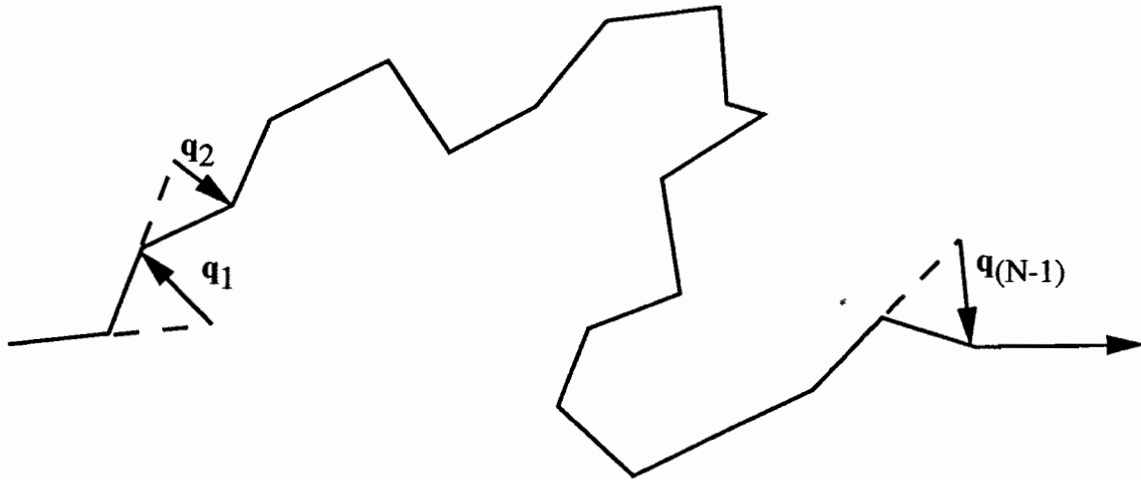


Figure 3.3: A path consists of many scattering events, each with an associated scattering wave vector.

events is

$$g_1^{(N)}(\tau) = \langle \exp(i\mathbf{q} \cdot \Delta\mathbf{r}(\tau)) \rangle^N. \quad (3.9)$$

This correlation function is simply the single scattering correlation function (equation (3.3)) raised to the  $N$ th power. By averaging over the particle displacements as we did for QELS (3.3), we arrive at

$$g_1(\tau) = \exp(-N\langle q^2 \rangle_\Omega D\tau) = \exp\left(-\langle q^2 \rangle_\Omega \langle \Delta\mathbf{r}(\tau) \rangle^2 \frac{s}{6l}\right), \quad (3.10)$$

where the total pathlength  $s$  is related to the number of scattering events by the mean distance between collisions  $N = s/l$ , and the brackets  $\langle \rangle_\Omega$  denote an average over all scattering angles. Substituting the connection between the distance between scattering events  $l$  and the transport mean free path  $l^*$  found in Eq. (2.22), we arrive at a more useful form of the field autocorrelation function:

$$g_1^{(s)}(\tau) = \exp(-k_0^2 \langle \Delta\mathbf{r}(\tau) \rangle^2 (s/l^*)/3). \quad (3.11)$$

This result has been experimentally verified in our laboratory using non-linear optical gating to select photons that scattered through paths of known length [15].

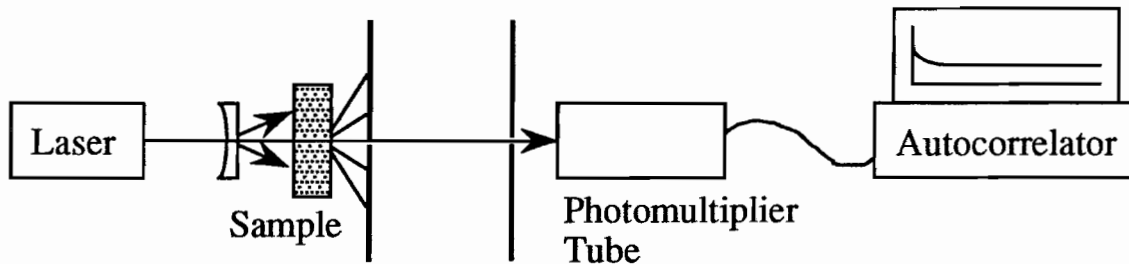


Figure 3.4: Diffusing-wave spectroscopy apparatus. A C.W. laser illuminates a slab of scattering particles. A single speckle of transmitted light flickers. The autocorrelation function of this flicker is connected to the transport of particles in the sample.

### 3.4 DWS of Photons which have Traveled Paths of Different Lengths

In simple DWS experiments (Fig. 3.4), photons scatter through paths of many different lengths before being detected. The resulting correlation function is obtained by averaging the single pathlength correlation function (3.11) over all photon pathlengths

$$g_1(\tau) = \int_0^{\infty} P(s) \exp(-k_0^2 \langle \Delta \mathbf{r}(\tau) \rangle^2 (s/l^*)/3) ds, \quad (3.12)$$

where the probability distribution of pathlengths is  $P(s)$  [16] (see Section 2.6 and Fig. 2.9). At this point, the meaning of the term “diffusing-wave spectroscopy” becomes apparent: in DWS, Eq. (3.12) is evaluated using the *photon-diffusion approximation* to calculate  $P(s)$ . In systems where  $P(s)$  is not known, Eq. (3.12) can still be used by *measuring*  $P(s)$ . The combination of Eq. (3.12) and measured pathlength distributions  $P(s)$  should be useful for a variety of complex opaque systems such as human tissue, liquid crystals, electrorheologic fluids, suspensions of magnetically interacting particles, and qualitative measurements on poorly characterized or very complex scattering systems.

### 3.5 The Siegert Relation

We generally do not measure the field correlation function  $g_1(\tau)$  discussed above (see Ref. [10] for a technique which directly measures  $g_1$ ). We use an electronic autocorrelator which measures the *intensity* autocorrelation function  $\langle I(t)I(t+\tau) \rangle / \langle I \rangle^2$ . Generally, one cannot simply replace the average of the square (the intensity) with the square of the average (the field correlation function). We must spend a few pages discussing the relationship between the field and intensity correlation functions. For fluctuations, which are described by Gaussian probability distributions such as (2.26) and (3.4), the two correlation functions are closely related; they are connected by the Siegert relationship via

$$g_2(\tau) = 1 + |g_1(\tau)|^2. \quad (3.13)$$

In this section we discuss the Siegert relation, its assumptions, and its implications for the use of pulsed lasers and lasers with finite coherence lengths in DWS. Many of the results described here were developed independently for C.W. lasers with finite coherence length [17]. We will therefore focus on the expression of the formalism that applies to pulsed lasers.

The standard derivation of the Siegert relation begins as Chapters 2 and 3 began, by expressing the electric field at the detector as a sum over all  $N$  sources:

$$E(t) = \sum_{i \in \text{all sources}} E_i(t) e^{i\phi_i(t)}, \quad (3.14)$$

where the field  $E_i(t) = F_i E_L(t)$ ,  $F_i$  is the form factor for scattering from the input field off of source  $i$  to the detector, and  $\phi_i$  is the phase of photons from a particular source. We generally assume that our systems are ergodic and stationary. *Ergodic* means that configurational averages are equivalent to time averages. *Stationarity* is the assumption that neither  $E_L$  nor  $F_i$  are time dependent [18]. Stationarity is a property of the light source; pulsed lasers are not stationary sources. Ergodicity is a property of the sample. Fluids are ergodic; gels are not ergodic. Without the

assumption of stationarity, but with the assumption of ergodicity, Eq. (3.2) becomes

$$G_1(\tau) = \left\langle \sum_{i,j \in \text{all sources}} E_i(t) E_j^*(t + \tau) e^{i(\phi_i(t) - \phi_j(t + \tau))} \right\rangle, \quad (3.15)$$

where capital  $G$  is used to denote unnormalized correlation functions as a notational convenience. According to (3.14), the intensity at the detector is

$$I(t) = \sum_{i,j \in \text{all sources}} E_i(t) E_j^*(t) e^{i(\phi_i(t) - \phi_j(t))}. \quad (3.16)$$

Thus, the intensity autocorrelation function is

$$G_2(\tau) = \left\langle \sum_{i,j,l,m} E_i(t) E_j^*(t) E_l(t + \tau) E_m^*(t + \tau) e^{i(\phi_i(t) - \phi_j(t) + \phi_l(t + \tau) - \phi_m(t + \tau))} \right\rangle. \quad (3.17)$$

The phases  $\phi_x(t)$  are uncorrelated random variables; therefore, each term in (3.17) in which the indices are not pairwise equal is, on average, zero. There are three types of terms with pairwise equal indices. First are the  $N^2 - N$  terms with  $i = j$  and  $l = m$ . These terms have *no* phase. They are simply

$$|E_i(t)|^2 |E_l(t + \tau)|^2. \quad (3.18)$$

The next  $N^2 - N$  non-zero terms have  $i = l$  and  $j = m$ . The exponent in these terms is the *sum* of the phases at  $t$  and  $t + \tau$ . That is, the exponential factor is,  $e^{i(\phi(t) + \phi(t + \tau))}$ , which is, on average, zero. The important terms are the  $N^2 - N$  terms with  $i = m$  and  $j = l$ . The exponent in these terms is the *change* in phase  $\delta\phi(t, \tau) \equiv \phi(t) - \phi(t + \tau)$ . The *change* in phase contains information about the system's dynamics. These terms are

$$E_i(t) E_i^*(t + \tau) E_j(t) E_j^*(t + \tau) e^{i(\delta\phi_i(t, \tau) - \delta\phi_j(t, \tau))}. \quad (3.19)$$

Finally, there are  $N$  terms with  $i = j = l = m$ . These are phaseless depending only on the amplitudes in (3.18) but with  $i = l$ . We will ignore these  $N$  terms as the  $N^2 - N$  terms with pairwise equal indices in (3.19) will overwhelm them.

With the assumption of that the incident intensity is time independent, we neglect the time dependence of the  $E$ 's in (3.18) and (3.19). Thus, (3.17) is evaluated by

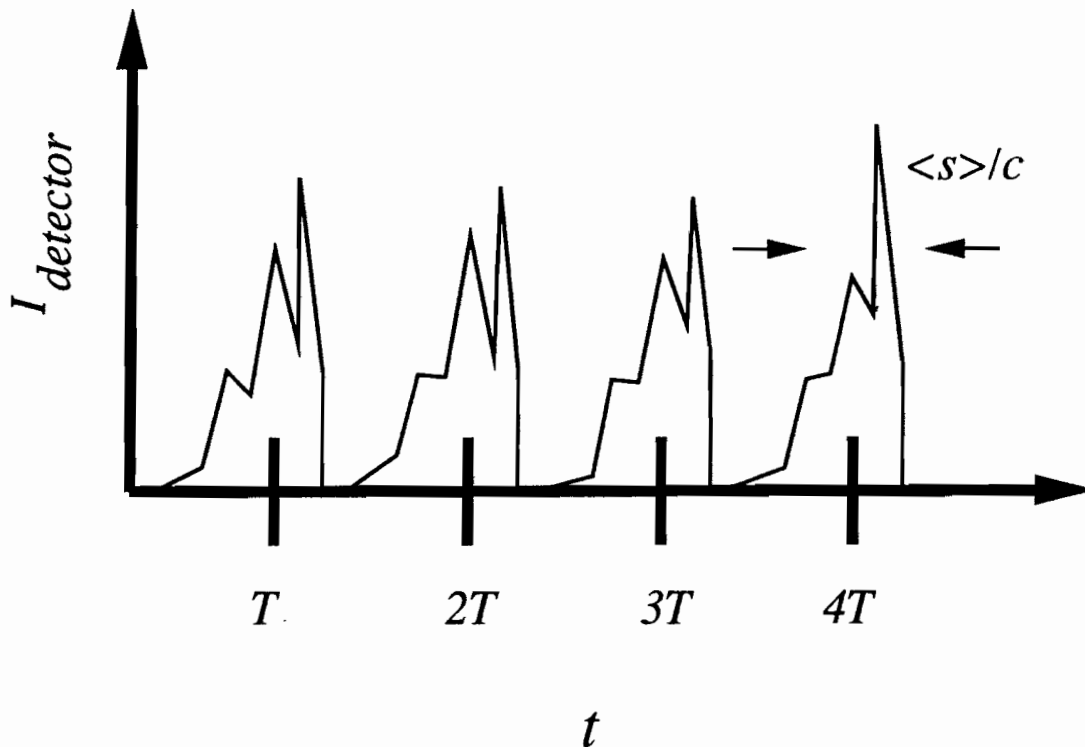


Figure 3.5: Pulses transmitted through a slab of colloid.

performing a configurational average over the change in phase  $\delta\phi(t, \tau)$  in (3.19). If we assume that changes in phase along paths  $i$  and  $j$  are uncorrelated, then we can decouple  $\delta\phi_i$  and  $\delta\phi_j$ , recovering (3.13) the Siegert relationship.

$$(3.19) \xrightarrow{\text{stationarity}} I^2 \langle e^{i(\delta\phi_i(t, \tau) - \delta\phi_j(t, \tau))} \rangle = I^2 \langle e^{i\delta\phi_i(\tau)} \rangle \langle e^{i\delta\phi_j(\tau)} \rangle \quad (3.20)$$

$$(3.18) \xrightarrow{\text{stationarity}} I^2. \quad (3.21)$$

Adding these terms together gives  $G_2(\tau) = I^2(1 + |g_1(\tau)|^2)$ . Deviations from the Siegert relationship may arise if the stationarity condition is violated, for instance, by the use of a pulsed laser. If the light source is a laser which produces a periodic train of pulses in which a new pulse begins whenever  $t = nT$ , the signal at the detector will be a series of stretched pulses.

We now wish to calculate the field and intensity autocorrelation functions for CW and pulsed laser sources. We will find that having a pulsed laser changes the

intensity correlation function in a complex and non-trivial way. The sum over all sources (3.2) required by DWS is replaced by an integral over all path lengths (3.12)

$$\sum_{i \in \text{all sources}} E_i(t - \frac{s}{c}) E_i^*(t - \frac{s}{c}) \longrightarrow \int_0^\infty ds P(s) E_L(t - \frac{s}{c}) E_L^*(t - \frac{s}{c}). \quad (3.22)$$

In this case, the fact that  $E_L(t)$  is pulsed will be significant unless the laser pulse width is much longer than the width of  $P(s)$ . To be concrete, examine the terms in  $G_2(\tau)$  of type (3.18). These terms constitute the constant part of  $G_2(\tau)$

$$\int dt ds_1 ds_2 P(s_1) P(s_2) \left| E_L(t - \frac{s_1}{c}) \right|^2 \left| E_L(t - \frac{s_2}{c} + \tau) \right|^2. \quad (3.23)$$

For a C.W. source, the electric fields may be factored out of this integral. For a pulsed source, however,  $\tau + (s_2 - s_1)/c$  must be within a laser pulse duration of the laser repetition time in order to contribute significantly to the final signal. The loss of separability of these integrals will violate the Siegert relation and make it more difficult to calculate the constant term in  $G_2(\tau)$ .

The terms in  $G_2(\tau)$  which decay, however, are even harder to calculate. Terms of type (3.19) are

$$\int dt ds_1 ds_2 P(s_1) P(s_2) E_L(t - s_1/c) E_L^*(t - s_1/c + \tau) E_L(t - s_2/c) E_L^*(t - s_2/c + \tau) \times e^{i(\delta\phi(t, s_1, \tau) - \delta\phi(t, s_2, \tau))} \quad (3.24)$$

where  $\delta\phi(t, s, \tau)$  is an average over paths of the same length. In the derivation of the Siegert relation, this integral is separated into the product of identical integrals over  $s_1$  and  $s_2$ . The time dependence of  $E_L$  prevents this factoring and thus violates the Siegert relationship. In particular, if the difference in path lengths is greater than the width of the input pulse  $|s_1 - s_2|/c \geq \Delta t$ , then the product of electric fields in (3.24) will be very small, reducing the contributions of these paths to the correlation function. For laser pulses of duration  $\Delta t$  comparable to or shorter than  $\Delta s/c$ , the number of paths contributing to the decaying of  $G_2(\tau)$  is reduced (see Fig. 3.6 for a graphic illustration of this effect). The relative weight of long pathlengths is also decreased in the final autocorrelation function, changing its functional form.

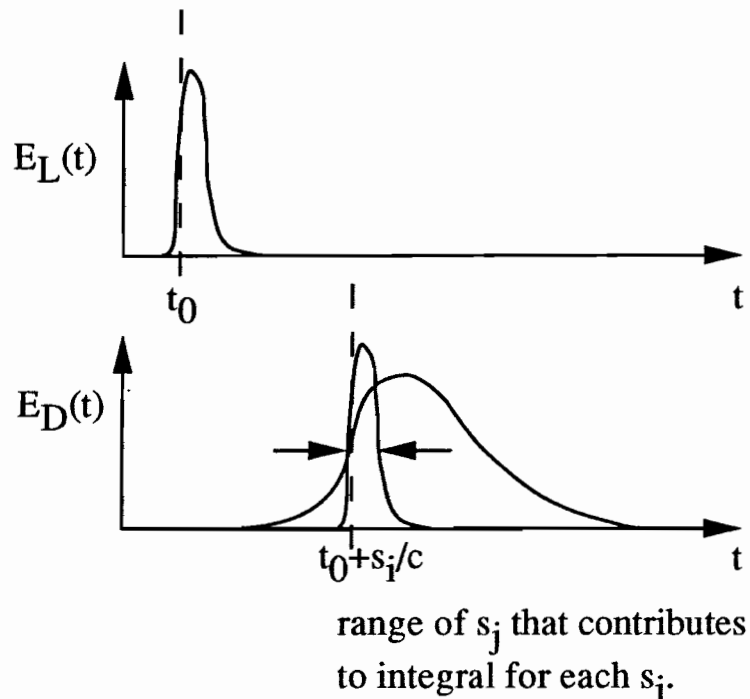


Figure 3.6: Graphic illustration of effect of short pulses on  $g_2(\tau)$ . The condition of stationarity generally allows the time dependence of the source to be factored out of the sum in (3.17). With a pulsed laser, however, the pulse duration limits the range of the sum over  $s_j$  which contribute to each term  $s_i$ . The sums are no longer separable. Finite coherence of a C.W. laser can be similarly included by replacing  $E_L(t - s_i/c)E_L^*(t - s_j/c)$  with a factor which indicates the loss of coherence as a function of  $s_i - s_j$ .

The same analysis can be applied to C.W. lasers with finite coherence lengths. There is a random, nonzero phase between  $E_L(t - s_i/c)$  and  $E_L^*(t - s_j/c)$  which introduces some factor  $f$  which is a function  $f(t - (s_i - s_j)/c)$ . This factor, which decays to  $1/e$  in a coherence time (1/bandwidth of the laser), prevents us from separating the sum over  $s_i$  and  $s_j$  in the same way that finite pulse duration did.

The evaluation of the expression in (3.24) is, in general, rather difficult. The important point is that the integral in (3.24) is *not* separable into independent integrals over  $s_1$  and  $s_2$ . The Siegert relation relies on this separability.

Note that the limitations that the Siegert relation imposes on the laser coherence time are different for measuring an intensity autocorrelation function than for measuring a field autocorrelation function. In an experiment capable of measuring  $G_1(\tau)$ , such as Diffusing-Wave Interferometry [10], the laser coherence time must be long, compared to  $G_1(\tau)$ 's decay time. In DWS, however, the coherence length must be long, compared to the width of  $P(s)$ .

### 3.6 Collective Diffusion

DWS is an exciting technique because it allows the study of very dense, interacting systems. In these systems, we must consider not just the evolution of an individual particle's position  $\Delta\mathbf{r}(\tau)$ , which is described by the *self-diffusion coefficient*, but also the collective motion of particles in the suspension, described by the *collective diffusion coefficient*. In this section, we introduce the concept of collective diffusion (Fig. 3.7) and contrast this notion with the notion of *self* diffusion. This discussion is important since light scattering is sensitive to collective diffusion; thus, DWS tells us about collective motion. The detailed connection between light-scattering and collective diffusion will be revisited and extended to polydisperse systems in Chapter 4.

There is a difference between "self-diffusion" or the diffusive displacement of a

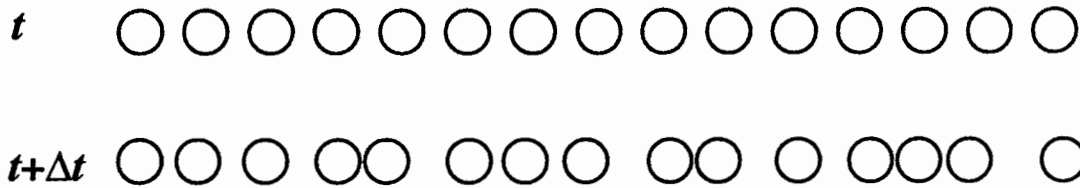


Figure 3.7: The  $q$  dependent diffusion coefficient represents the decay of periodicities that may appear in a system. Here we see a periodic one dimensional array of particles lose its periodicity.

particle described by  $\langle \Delta r(\tau)^2 \rangle = 6D\tau$  and collective diffusion, which is the decay of density fluctuations involving many particles. The diffusion equation for a collection of particles is

$$\partial_t \rho(\mathbf{r}, t) = D \nabla^2 \rho(\mathbf{r}, t), \quad (3.25)$$

where  $\rho$  is the number density of particles. The Fourier space version of this equation is

$$\partial_t \rho(\mathbf{q}, t) = -Dq^2 \rho(\mathbf{q}, t), \quad (3.26)$$

which has as a solution

$$\rho(\mathbf{q}, t) = A(q)e^{-Dq^2 t} + B(q). \quad (3.27)$$

The Fourier transformation is defined by

$$\rho(\mathbf{q}, t) = \int \rho(\mathbf{r}, t) e^{-i\mathbf{q}\cdot\mathbf{r}} d\mathbf{r} \quad (3.28)$$

$$\rho(\mathbf{r}, t) = \frac{1}{2\pi} \int \rho(\mathbf{q}, t) e^{i\mathbf{q}\cdot\mathbf{r}} d\mathbf{q}. \quad (3.29)$$

In the Fourier space picture, we can easily discuss the decay of concentration fluctuations. The diffusion equation (3.26) describes the net motion of diffusing particles, not the detailed motion of individual particles. In systems with a characteristic length scale, such as the particle diameter in a colloidal suspension, the diffusion coefficient will be  $q$ -dependent. Notice that for very large wave-vectors, where  $qa \gg 1$ , the collective diffusion coefficient refers to the collective behavior of volumes much smaller than a particle diameter. Motion on such short length scales is conceptually

and formally the same as self-diffusion. That is, in the large- $q$  limit, the collective diffusion coefficient approaches the self diffusion coefficient. Later in this section, we will see that the diffusion of density from fluctuations at a wave-vector  $q$  which persist as peaks in the structure factor is slower than diffusion of fluctuations at non-favored wave-vectors.

By examining the correlation function (3.2), we will now show that the diffusion coefficient measured by light scattering is, in fact, the collective diffusion coefficient. The single scattering field autocorrelation function is

$$\langle E^*(0)E(\tau) \rangle = I_0 \left\langle \sum_{k,l} F(q) e^{i\mathbf{q} \cdot (\mathbf{r}_k(0) - \mathbf{r}_l(\tau))} \right\rangle, \quad (3.30)$$

where the  $F$ 's are form factors. To examine the decay of (3.30) we follow Pusey and Tough [12] and examine the cumulant expansion of (3.30). For a function  $\mathcal{F}(x)$  the cumulant expansion is defined by

$$\mathcal{F}(x) = e^{K_1 x + K_2 x^2 + \dots}. \quad (3.31)$$

The first term cumulant  $K_1$  of the field autocorrelation function (3.30) is  $q^2 D$ . In fact, it is common to define the diffusion coefficient as the first cumulant of the QELS autocorrelation function divided by  $q^2$ . To calculate the first cumulant, we take the derivative

$$q^2 D = \lim_{\tau \rightarrow 0} \frac{d}{d\tau} \log(\langle E^*(0)E(\tau) \rangle) = \frac{1}{\langle E^*(0)E(0) \rangle} \lim_{\tau \rightarrow 0} \frac{d}{d\tau} \langle E^*(0)E(\tau) \rangle. \quad (3.32)$$

Using some helpful techniques found in [19], we arrive at

$$\frac{d}{d\tau} \langle E^*(0)E(\tau) \rangle = -I_0 q^2 \sum_{k,l} F(q) \int_0^\infty dt \langle \mathbf{v}_k(0) \cdot \mathbf{v}_l(t) e^{i\mathbf{q} \cdot (\mathbf{r}_k(0) - \mathbf{r}_l(t))} \rangle. \quad (3.33)$$

The velocity-velocity correlation function falls off in a time characteristic of ballistic motion; the phase in the integral in (3.33) certainly changes very little in this time. Moreover, on this short time scale, the velocities of distinct particles are surely uncorrelated. That is, the relationship between the velocity autocorrelation function

and the self-diffusion coefficient holds only for terms with  $k = l$

$$\int_0^\infty dt \langle \mathbf{v}_k(0) \cdot \mathbf{v}_l(t) \rangle = 3D\delta_{kl}. \quad (3.34)$$

To the extent that the approximations leading to (3.34) are wrong, a factor of  $H(q, \tau)$  may be introduced. In this section we will treat  $H(q, \tau)$  as being equal to one. We now simplify the derivative (3.32)

$$\frac{d}{d\tau} \langle E^*(0)E(\tau) \rangle = I_0 q^2 F(q) N D, \quad (3.35)$$

for  $N$  particles. The factor of 3 in (3.34) is due to the number of dimensions (3) available to the diffusing particle. Using (3.35) in (3.32) and the definition of the structure factor (2.4) we arrive the collective diffusion coefficient

$$D(q) = \frac{I_0 N q^2 F(q) D_0}{I_0 N F(q) S(q)} \quad (3.36)$$

$$= \frac{D_0}{S(q)}. \quad (3.37)$$

This result correctly implies that fluctuations at a wave-vector  $q$  favored by the structure factor persist and that light scattering measures a collective diffusion coefficient.

In single scattering experiments, the  $q$ -dependent diffusion coefficient can be measured. Multiple light scattering, however, averages over scattering wave-vectors, obscuring resolution of motion on different length scales. Thus, in diffusing-wave spectroscopy, a  $q$ -averaged diffusion coefficient is measured. The angular average appeared previously in the development of the DWS autocorrelation function (3.10). Including the  $q$ -dependence of the DWS autocorrelation function, DWS measures the effective diffusion coefficient

$$D_{eff} = \frac{\int_0^{2k_0a} F(q) S(q) D(q) q^3 dq}{\int_0^{2k_0a} F(q) S(q) q dq}. \quad (3.38)$$

That is, the measured diffusion coefficient is a  $q$ -averaged value of the collective diffusion coefficient. The range over which this average is taken depends on  $k_0a$ , which is the upper cutoff of the integrals in (3.38) and is proportional to the ratio of

the particle diameter to the probe wavelength. When the wavelength is larger than the particle size, DWS measures collective diffusion on long length scales. When the probe is smaller than the particle, DWS essentially measures self-diffusion.

## 3.7 Analytic Techniques

In any given DWS experiment, an intensity autocorrelation function is measured and must then be interpreted. Rather than working with the integral form of the DWS correlation function in (3.12) we can either measure  $P(s)$  or use an experimental geometry in which  $P(s)$  is known. Given  $P(s)$  we can evaluate the integral, arriving at an explicit expression for the autocorrelation function. In this section, we will review the practical details of the analysis of DWS autocorrelation functions.

### 3.7.1 Obtaining $g_1(\tau)$

The first step in our analysis is to relate the measured intensity autocorrelation function to a field autocorrelation function. According to the Siegert relation (3.13), the connection between the field and intensity autocorrelation functions is quite straightforward. The experimentally useful form of the Siegert relation is slightly more complicated. It includes a geometric factor due to the finite size of the collection aperture

$$g_2(\tau) = 1 + \beta |g_1(\tau)|^2, \quad (3.39)$$

where  $\beta$  is less than one. If all polarizations are measured,  $\beta$  cannot be greater than  $1/2$ ; typically,  $\beta$  is between 0.15 and 0.35. Small values of  $\beta$ , less than 0.10, are symptomatic of experimental problems that should be addressed before proceeding.

The measured autocorrelation function is unnormalized. That is, it is of the form  $A(1 + |g_1(\tau)|^2)$ . In order to recover the field autocorrelation function, we must find the experimental baseline. For scattering from ergodic systems, the baseline is the infinite- $\tau$  value of the measured intensity autocorrelation function. Electronic

MATTER PHYSICS ASIA

correlators keep track of this by maintaining a few channels of the correlation function at very large values of  $\tau$ . For truly gaussian sources, the baseline can be calculated using the total number of counts  $A$ , the elapsed time  $T$ , and the sample time  $dt$  (see Section 7.2.3 for details on autocorrelators):

$$G_2(\tau \rightarrow \infty) = \left( \frac{A dt}{T} \right)^2 . \quad (3.40)$$

The measured and calculated baselines must differ by less than about 0.1%; larger differences are signatures of significant non-gaussian fluctuations, such as a change in laser power or a dust drifting through the input beam.

After baseline subtraction and normalization of the correlation function, the value of  $\beta$  may be estimated either by assuming that the  $\beta$  is the normalized value of the first measured channel or by fitting an exponential to the first several normalized channels and using the amplitude of this exponential as  $\beta$ .

### 3.7.2 Analytic forms of $g_1(\tau)$

In this section, we mention a significant mathematical simplification used in the derivation of analytic forms of the DWS autocorrelation function [1]. In the next sections, we will consider techniques for fitting to the analytic results for two simple geometries. The DWS autocorrelation function (3.12) is closely related to the Laplace transform of  $P(s)$ , the probability that a photon took a path of length  $s$ . We calculate probability distribution using the photon diffusion approximation for photon transport described in the previous chapter. We compare the autocorrelation function and the Laplace transform of  $P(s)$  here

$$g_1(\tau) = \int_0^\infty P(s) e^{-2k_0^2 \frac{s}{l^*} D \tau} ds \quad (3.41)$$

$$p(u) = \int_0^\infty P(s) e^{-su} ds , \quad (3.42)$$

where  $p(u)$  is the Laplace transform of  $P(s)$ . By inspection, these quantities can be equated

$$g_1(\tau l^* / 2k_0^2 D) = p(\tau). \quad (3.43)$$

The utility of this observation is apparent when using handbooks of solutions to the diffusion equation such as [20]. In these texts, we find that often the Laplace transform of  $P(s)$  is calculated more easily than  $P(s)$  itself. For DWS, the easier step of calculating the Laplace transform is sufficient.

### 3.7.3 Backscattering

DWS can be done by collecting light that is backscattered from the sample (Fig. 3.8). The use of a backscattering geometry for DWS is somewhat problematic as some of the photons detected will have traveled paths which are short compared to  $l^*$ , and thus the intensity due to these paths is not well described by the photon diffusion approximation [21]. The backscattering geometry, however, works well, often better than can be expected, and this geometry can be used with samples with much stronger photon absorption than the transmission geometry. The correlation function is [1]:

$$g_1(\tau) = \frac{\sinh \left[ \sqrt{\frac{6\tau}{\tau_0}} \left( \frac{L}{l^*} - \alpha \right) \right] + \frac{2}{3} \sqrt{\frac{6\tau}{\tau_0}} \cosh \left[ \sqrt{\frac{6\tau}{\tau_0}} \left( \frac{L}{l^*} - \alpha \right) \right]}{\left( 1 + \frac{8}{3} \frac{\tau}{\tau_0} \right) \sinh \left[ \frac{L}{l^*} \sqrt{\frac{6\tau}{\tau_0}} \right] + \frac{4}{3} \sqrt{\frac{6\tau}{\tau_0}} \cosh \left[ \frac{L}{l^*} \sqrt{\frac{6\tau}{\tau_0}} \right]}, \quad (3.44)$$

which, for a sample of infinite thickness simplifies to

$$g_1(\tau) = \frac{e^{-\alpha \sqrt{\frac{6\tau}{\tau_0}}}}{1 + \frac{2}{3} \sqrt{\frac{6\tau}{\tau_0}}}, \quad (3.45)$$

where  $\alpha$  is a parameter of order one discussed in section 2.5, and  $\tau_0$  is  $1/Dk_0^2$ . Note that the correlation function for scattering from a thick sample does not depend on  $l^*$ . The backscattering correlation function depends only on one parameter, the effective diffusion coefficient and is thus simpler to analyze than the transmission correlation function discussed in the next section.

We analyze (3.45) by expanding in powers of  $\sqrt{\tau}$ . The coefficient of the first term in this expansion is  $(2/3 + \alpha)\sqrt{6/\tau_0}$ , which is proportional to the square root of the particle diffusion coefficient. Rather than experimentally determining  $\alpha$ , which depends slightly on the ratio of  $l^*$  to  $l$  (2.11) [22], we generally make two measurements

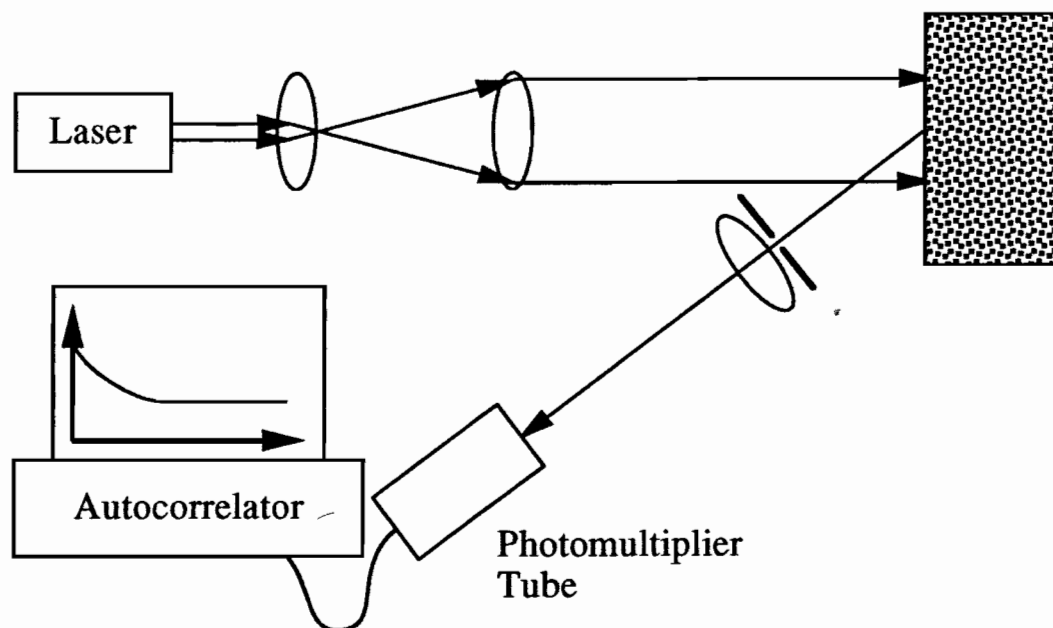


Figure 3.8: DWS backscattering apparatus. A collection lens images the sample onto a photomultiplier tube, and an iris limits the angular range of light collected.

and report the ratio of the diffusion coefficients of a known, well characterized sample and the sample being studied. Backscattering DWS can be particularly useful for quality control applications in which samples are compared to controls which are known to be of high quality. In Ref. [23], an application of backscattering DWS for quality control purposes developed in our laboratory is reported.

### 3.7.4 Transmission

The autocorrelation function for transmission through a slab of infinite transverse extent and thickness  $L$  is more complex than the backscattering function [1]

$$g_1(\tau) = \frac{L/l^* + 4/3}{\alpha + 2/3} \frac{\sinh \left[ \alpha \sqrt{\frac{6\tau}{\tau_0}} \right] + \frac{2}{3} \sqrt{\frac{6\tau}{\tau_0}} \cosh \left[ \alpha \sqrt{\frac{6\tau}{\tau_0}} \right]}{\left( 1 + \frac{8}{3} \frac{\tau}{\tau_0} \right) \sinh \left[ \frac{L}{l^*} \sqrt{\frac{6\tau}{\tau_0}} \right] + \frac{4}{3} \sqrt{\frac{6\tau}{\tau_0}} \cosh \left[ \frac{L}{l^*} \sqrt{\frac{6\tau}{\tau_0}} \right]} . \quad (3.46)$$

For times short compared to the decay time of a single scattering correlation function  $\tau_0$ , this reduces to

$$g_1(\tau) \approx \frac{\left(\frac{L}{l^*} + \frac{4}{3}\right) \sqrt{\frac{6\tau}{\tau_0}}}{\left(1 + \frac{8}{3} \frac{\tau}{\tau_0}\right) \sinh\left[\frac{L}{l^*} \sqrt{\frac{6\tau}{\tau_0}}\right] + \frac{4}{3} \sqrt{\frac{6\tau}{\tau_0}} \cosh\left[\frac{L}{l^*} \sqrt{\frac{6\tau}{\tau_0}}\right]}. \quad (3.47)$$

The time it takes for this function to decay is proportional to  $\tau_0(l^*/L)^2$ .

Unlike the backscattering correlation function, which depends only on the diffusion coefficient, the transmission correlation function depends on two quantities,  $L/l^*$  and  $D$ . The fact that the decay time of these functions is proportional to  $(l^*/L)^2/k_0^2 D$  suggests that the correlation function is interdependent on  $l^*$  and  $D$ . As a result, the transmission correlation function can be used to either fit for the diffusion coefficient or for  $l^*$  in a sample where the particle dynamics are well known. We fit to either  $l^*$  or  $D$  and the value of  $\beta$ , using the simplex method described in Ref. [24].

An alternative approach, which is suitable for very thick samples, is to fit the correlation function to an expansion in  $\tau$ . Then, using the scaling relationship that the average pathlength  $s$  is proportional to  $L^2/l^*$ , we claim that the diffusion coefficient is proportional to  $\Gamma_1 * (l^*/L)^2$ . The first few terms of the expansion of the correlation function (3.47) are:

$$\begin{aligned} g_1(\tau) = 1 &+ \frac{(36 - 13(L/l^*) - 60(L/l^*)^2 - 15(L/l^*)^3)}{5(4 + 3(L/l^*))} \tau \\ &+ \frac{624 - 1944(L/l^*) - 2929(L/l^*)^2 + 3680(L/l^*)^3 + 6390(L/l^*)^4}{50(4 + 3(L/l^*))^2} \tau^2 \\ &+ O(\tau)^{\frac{5}{2}}, \end{aligned} \quad (3.48)$$

where  $\tau_0 = 1/Dk_0^2$ . By examining the term proportional to  $\tau$ , we can see that fitting to the first two cumulants is a good, simple analytic approach for samples thicker than 20 or 30  $l^*$ , but should be used, in general, with caution. In particular, we plot the first cumulant divided by  $(L/l^*)^2$  as a function of sample thickness in Fig. 3.7.4.

For practical experiments, with samples between 20 and 40  $l^*$  thick, this approach will give consistent answers  $\pm 10\%$ . When greater accuracy is required, a complete fit to the full correlation function is required.

WILEY-INTERSCIENCE

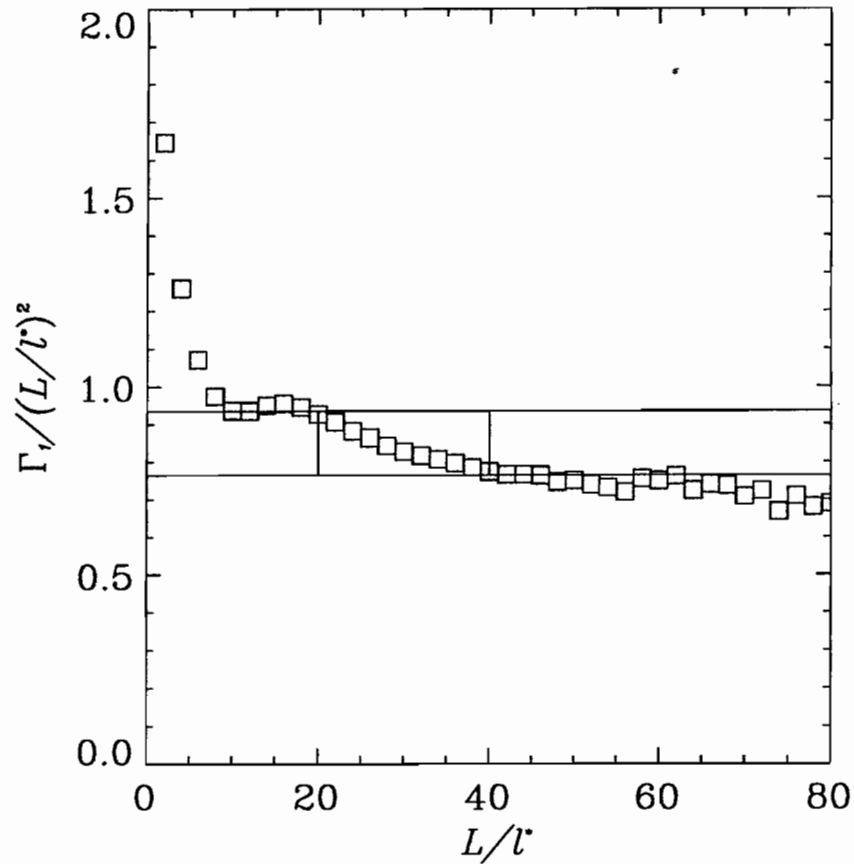


Figure 3.9: The scaling relationship for the first cumulant as a function of sample thickness is examined here. It is apparent that the relationship is approximately correct, producing results that are consistent to within  $\pm 10\%$  for samples between 20 and 30  $l^*$  thick, and better results for thicker samples. It is also apparent, however, that this is not an ideal strategy for analyzing transmission correlation functions. This figure was prepared by finding the first cumulant to the analytic form of the transmission autocorrelation function for the same diffusion coefficient, and different sample thicknesses.

# Bibliography

- [1] D. J. Pine, D. A. Weitz, J. X. Zhu, and E. Herbolzheimer, *Diffusing-Wave Spectroscopy: Dynamic Light Scattering in the Multiple Scattering Limit*, J. Phys. France **51**, 2101 (1990).
- [2] D. A. Weitz and D. J. Pine, in *Dynamic Light Scattering* (Oxford University Press, New York, 1993).
- [3] A. G. Yodh *et al.*, *Speckle fluctuations and their use as probes of dense random media*, Mol. Cryst. Liq. Cryst. Sci. Technol. - Sec B Nonlinear Optics **3**, 149 (1992).
- [4] F. C. MacKintosh and S. John, *Diffusing-Wave Spectroscopy and Multiple Scattering of Light in Correlated Random Media*, Phys. Rev. B **40**, 2383 (1989).
- [5] X. Qiu, *Diffusion in equilibrium and non-equilibrium interacting liquids*, Ph.D. thesis, University of Pennsylvania, 1990.
- [6] J. Zhu, *Diffusing-Wave Spectroscopy*, Ph.D. thesis, City University of New York, 1992.
- [7] F. C. MacKintosh, *Multiple scattering of classical waves in random media*, Ph.D. thesis, Princeton University, 1989.
- [8] R. K. Pathria, *Statistical Mechanics* (Pergammon, Oxford, 1972).

MATH PHYSASIR

- [9] F. Reif, *Fundamentals of statistical and thermal physics* (McGraw-Hill, New York, 1965).
- [10] M. H. Kao, A. G. Yodh, and D. J. Pine, *Observation of brownian motion on the time scale of hydrodynamic interactions*, Phys. Rev. Lett. **70**, 242 (1992).
- [11] E. J. Hinch, *Application of the Langevin Equation to Fluid Suspensions*, J. Fluid Mech. **72**, 499 (1975).
- [12] R. A. Pecorra, *Dynamic Light Scattering Applications of photon correlation spectroscopy* (Plenum Press, New York, 1985).
- [13] B. Chu, *Laser light scattering : basic principles and practice* (Academic Press, Boston, 1991).
- [14] K. S. Schmitz, *An introduction to dynamic light scattering by macromolecules* (Academic Press, Boston, 1990).
- [15] A. G. Yodh, P. D. Kaplan, and D. J. Pine, *Pulsed Diffusing-Wave Spectroscopy: High Resolution through Nonlinear Optical Gating*, Phys. Rev. B **42**, 4744 (1990).
- [16] G. Maret and P. E. Wolf, *Multiple Light Scattering from Disordered Media. The Effect of Brownian Motion of Scatterers*, Z. Phys. B **65**, 409 (1987).
- [17] T. Beilini, M. A. Glaser, N. A. Clark, and V. Degiorgio, *Effects of finite laser coherence in quasielastic multiple scattering*, Phys. Rev. A **44**, 5215 (1991).
- [18] L. Mandel and E. Wolf, *Coherence Properties of Optical Fields*, Rev. Mod. Phys. **37**, 231 (1965).
- [19] J. P. Hansen and I. R. McDonald, *Theory of simple liquids* (Academic Press, London, 1986).

- [20] H. S. Carslaw and J. C. Jaeger, *Conduction of Heat in Solids, Second Edition* (Oxford University Press, New York, 1959).
- [21] B. J. Ackerson, R. L. Dougherty, N. M. Reguigui, and U. Nobbman, , J. Thermophys. and Heat Trans. **6**, 577 (1992).
- [22] S. Fraden and G. Maret, *Multiple Light Scattering from Concentrated Interacting Suspensions*, Phys. Rev. Lett. **65**, 512 (1990).
- [23] P. D. Kaplan, A. G. Yodh, and D. F. Townsend, *Noninvasive study of gel formation in polymer-stabilized dense colloids using multiply scattered light*, J. Coll. and Int. Sci. **155**, 31 (1993).
- [24] W. H. Press, B. P. Flannery, S. A. Teukolsky, and W. T. Vetterling, *Numerical recipes in C : the art of scientific computing* (Cambridge, New York, 1988).

# Chapter 4

## Miscible Binary Systems: Dynamics and Structure

Our first experiment on binary colloids is quite complex. It is clear that without an understanding of static transport (*i.e.*,  $l^*$ ), DWS experiments are difficult to interpret. For this experiment, we tested and then used the standard Percus-Yevick theory for structure in binary suspensions. Based on successful measurements of  $l^*$ , we then measured hydrodynamic interactions between colloidal particles of different diameters for the first time. The first section of this chapter outlines our approach and discusses the data. Several fairly complex theoretical discussions are treated very briefly in this first section and then expanded later in the chapter.

### 4.1 Introduction and Survey

Asymmetric binary colloids present fundamental geometric questions about particle packing and interparticle forces. In contrast to uniform dispersions, binary colloids contain two distinct types of particles whose interaction depends on their relative size [1]. This extra degree of freedom introduces a complex, short-range order that can produce a much richer variety of phases at the solidification point [2] and in

the pure liquid [3]. Particle-size asymmetry also leads to instabilities and new dynamic structures in sedimenting colloids [4]. The character of these dynamic structures is controlled by the hydrodynamic interactions between different particles. In equilibrium systems, these same hydrodynamic interactions determine the Brownian diffusivity of particles and, therefore, set the time scale of the kinetics for phase transitions.

While hydrodynamic interactions between particles in polydisperse systems have attracted considerable theoretical attention in recent years, there has been little experimental work [2, 5–8] that critically tests emerging theories [9–13]. Surprisingly, few experimental studies have tested the static structure of highly asymmetric, binary, hard-sphere systems [5], although predictions based on the Percus-Yevick approximation have been available for some time [14]. This situation has arisen, in part, because traditional optical techniques are difficult to apply to dense colloids as a result of strong multiple light scattering. In this chapter, we present new diffusing-wave spectroscopy (DWS) [15–17] experiments which exploit multiple light scattering to probe diffusion and structure in dense, binary hard-sphere suspensions. This information is extracted within DWS theory by modeling photon transport as a random walk. Our work explicitly probes the hydrodynamic coupling between *unlike* spheres and thus represents a first step towards elucidating the role of particle size asymmetry and concentration in multi-component diffusion theories. In addition, we probe the structure of highly asymmetric, binary mixtures of hard-spheres at high densities and test calculations of the static partial structure factors determined within the Percus-Yevick approximation for widely separated particle sizes. Finally, we extend the theory of DWS to strongly interacting binary colloids.

A first glance at the data highlights the importance of interparticle dynamics and interparticle ordering. Measurements were made on three mixtures of polystyrene spheres with the same ratio of diameters but different average particle size (Table 4.1).

Table 4.1: To probe similar physics on different length scales, we study three systems with the same ratio of particle diameters but different absolute sizes.

	Small	Medium	Large
$a_L$ ( $\mu m$ )	0.205	0.625	2.00
$a_S$ ( $\mu m$ )	0.065	0.205	0.625
$\alpha \equiv a_S/a_L$	0.32	0.33	0.31
$\phi_L$	0.045	0.051	0.102
$k_0 a_L$	3.3	10.1	32.2

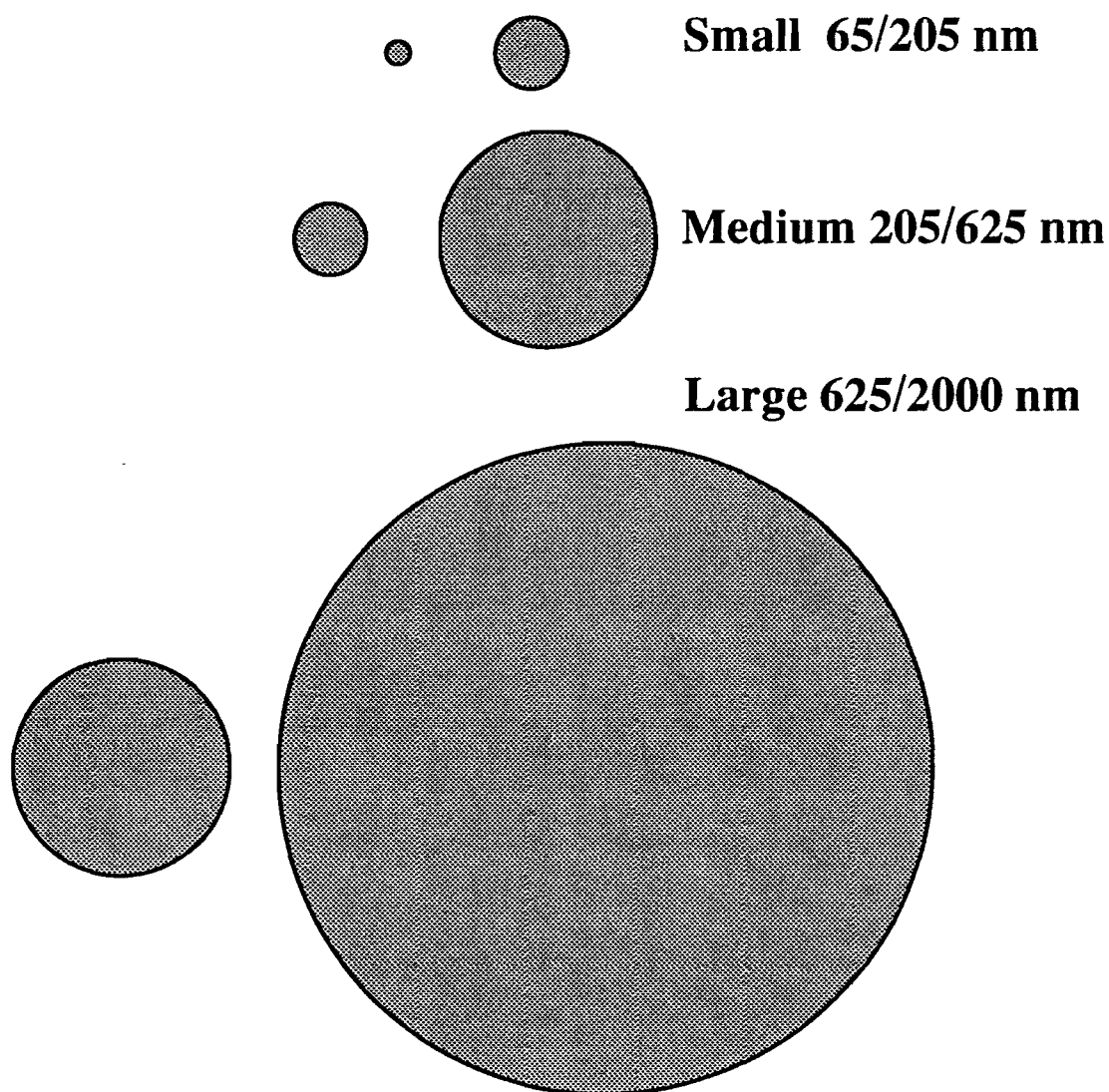


Figure 4.1: Graphic comparison of systems studied.

Measured differences between the systems are a result of the dependence of DWS on the ratio of particle size to wavelength. In each system, the volume fraction of large spheres  $\phi_L$  is held constant, and the volume fraction of small spheres  $\phi_S$  is varied. In Fig. 4.2, we plot the reciprocal of the photon random walk step-length  $1/l^*$  as a function of  $\phi_S$ . This quantity,  $1/l^*$ , is analogous to the resistivity of a binary liquid alloy [18,19]. In the first approximation these graphs are straight lines; that is, the optical resistivity is proportional to the number density of scatterers. Deviations from straight lines are a result of particle ordering, which decreases the optical resistivity. The effects of ordering are most remarkable in the smallest system where  $1/l^*$  actually *decreases* with the addition of scattering particles. In Fig. 4.3, the effective diffusion coefficient  $D_{eff}$  normalized to the value for a system with no small spheres is plotted as a function of small-sphere volume fraction  $\phi_S$ . Notice that  $D_{eff}$  first increases with  $\phi_S$  and then begins to decrease. This unusual behavior is the result of two mechanisms: the increasing contribution of small particles to the scattering as  $\phi_S$  is increased and the hydrodynamic coupling between large and small particles. Our measurements represent the first experimental determination of this coupling.

To measure  $l^*$  and  $D_{eff}$ , we employ standard DWS techniques (Chapter 3). Samples in 0.5 or 1.0-mm-thick cuvettes are illuminated from one side by the 514-nm line of an Ar-ion laser, and the intensity of a single speckle of transmitted light is monitored. By comparing the average intensity to known monodisperse samples, we deduce  $l^*$  [21]. Using  $l^*$ , we extract an effective diffusion coefficient from the first cumulant of the measured intensity autocorrelation functions, whose time dependence is proportional to the square of the field autocorrelation function  $g_1(\tau) \equiv \langle E(\tau)E^*(0) \rangle / \langle |E|^2 \rangle$ . For multiply scattered light, DWS theory gives [15–17] (see Eq. 3.12)

$$g_1(\tau) = \int_0^\infty P(s) \exp(-2 \frac{s}{l^*} k_0^2 D_{eff} \tau) ds, \quad (4.1)$$

where  $P(s)$  is the fraction of detected photons that traveled a distance  $s$  through the

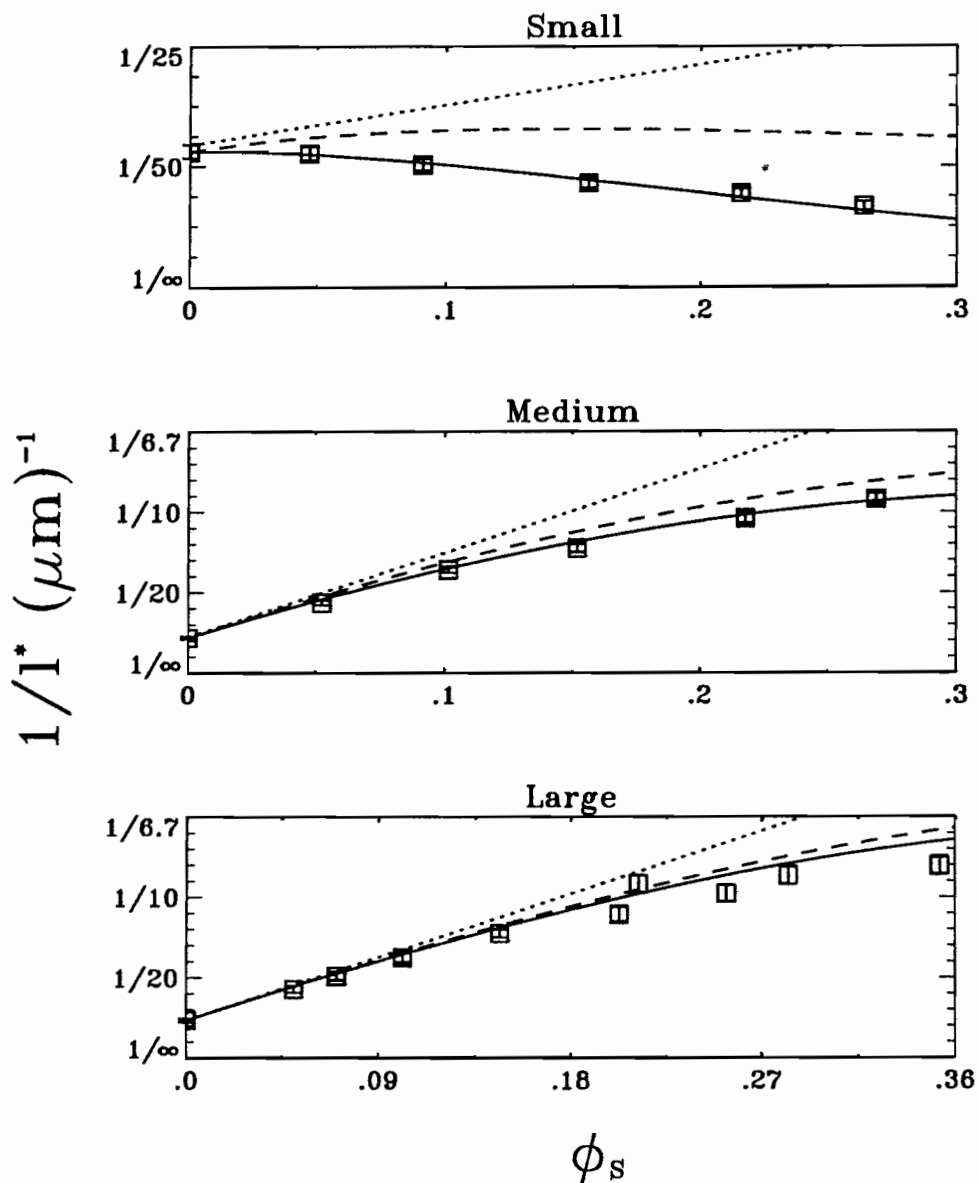


Figure 4.2: Measurements of the reciprocal photon transport mean free path  $1/l^*$  show the effects of interparticle structure. Calculations using the full PY binary hard-sphere structure factors (solid line) agree with the data and differ most from a non-interacting theory (dotted line) and a theory without interspecies structure [20] (dashed line) when the particles are smaller than the wavelength of the probe.

sample, and  $k_0$  is the laser wave vector in the solvent. The spheres are polystyrene suspended in water. We estimate the screening length of the polystyrene spheres in suspension to be  $\sim 40 \text{ \AA}$  so that the interparticle potential is essentially hard-sphere.

Two aspects of binary colloids are important for understanding our measurements: *static* particle ordering and *dynamic* particle diffusion in the presence of other particles. The static problem is solved using only the hard-sphere interaction potential to calculate  $l^*$ . A full solution of the dynamic problem requires knowledge of particle hydrodynamics *and* interparticle structure.

The static problem can be reduced to the calculation of interparticle partial structure factors in a binary system [22,23]. Within the diffusion approximation for photon transport, the key quantity is the photon random walk step-length  $l^*$ , which depends on the number of scattering events needed to randomize the direction of a photon; this number depends on the scattering properties of individual particles as well as spatial correlations between particles [20]. A general expression for  $l^*$  is [20,24] (see Eq. (2.22)):

$$l^* = k_0^6 a^4 \left( \pi \rho \int_0^{2k_0 a} I(y) y^3 dy \right)^{-1}, \quad (4.2)$$

where  $\rho$  is the number density of particles,  $a$  is the particle diameter, and  $\mathbf{y} = (\mathbf{k}_0 - \mathbf{k}_f)a$  is the dimensionless momentum transfer for a single scattering event. In a monodisperse system,  $I(y)$  is simply the product of the form and structure factors  $F(y)S(y)$ . In a binary system, we still calculate  $l^*$  using Eq. (4.2), but now we replace  $\rho$  with  $\rho_L + \rho_S$ ,  $a$  with  $a_L$  (following the convention of Ref. [25,26]), and  $I(y)$  with

$$\begin{aligned} I(y)\rho &= S_{LL}(y)F_L(y)\rho_L + S_{SS}(y)F_S(y)\rho_S \\ &\quad + 2S_{LS}(y)\text{Re}(f_L(y) \cdot f_S^*(y))\sqrt{\rho_L\rho_S}, \end{aligned} \quad (4.3)$$

where  $F(y) = |f(y)|^2$ , and  $f(y)$  is the dimensionless, far field, single scattering amplitude. The partial structure factors are defined as a sum over all particle positions

$\mathbf{r}_i^\alpha$  and  $\mathbf{r}_j^\beta$  of type  $\alpha$  and  $\beta$  (this is developed fully in Section 4.2):

$$S_{\alpha\beta}(y \neq 0) = \frac{1}{\sqrt{N_\alpha N_\beta}} \left\langle \sum_{ij} \exp[i\mathbf{y} \cdot (\mathbf{r}_i^\alpha - \mathbf{r}_j^\beta)/a_L] \right\rangle. \quad (4.4)$$

Since  $F(y)$  is known from Mie scattering theory, the only missing elements of the calculations of  $l^*$  are the partial structure factors, which measurements of  $l^*$  directly probe.

Of the many schemes available for calculating the thermodynamic properties of disordered systems, the Percus-Yevick (PY) approximation has an analytic solution for dense hard-sphere systems. Our calculations of  $l^*$ , based on the PY structure factors [25, 26], are presented with the data in Fig. 4.2. For the small and medium particle-size systems, the theory is in excellent agreement with the data; for the large particle-size system, the agreement is still quite satisfactory, although PY overestimates  $1/l^*$  by approximately 10% for  $\phi_S > 0.2$ . To illustrate the importance of using the full structure factor, we also plot the results of a calculation which ignore all interparticle structure ( $S_{\alpha\beta}(y) = \delta_{\alpha\beta}$ ) and results which ignore just correlations between particle species ( $S_{LS}(y) = 0$ ).

The difference between data sets results solely from the different cutoffs in the integral over  $I(y)y^3$  in Eq. (4.2). By varying particle size, we probe the  $y$ -dependence of  $I(y)$ . Measurements in the small system reveal the most about the long-range structure of the colloid because they are sensitive to relatively low- $y$ . Conversely, measurements in the large system reveal the most about the local structure of the colloid. With the exception of computer simulations [8], our work is one of the few experimental tests of PY for a dense, highly asymmetric, hard-sphere system. The excellent agreement for  $l^*$  indicates that the  $I(y)$  used in Eq. (4.3) is reasonable.

We consider the dynamic problem by building a multiple scattering theory from a single scattering result. In a single-scattering photon correlation experiment,  $D_{eff}$  is extracted from the first cumulant of  $g_1(\tau)$ . Following the derivation of Ref. [27]

for monodisperse colloids and *ignoring hydrodynamics*, we find for binary mixtures

$$D_{eff}(y) = \frac{D_{L0}F_L(y)\rho_L + D_{S0}F_S(y)\rho_S}{I(y)\rho}, \quad (4.5)$$

where  $D_{L0}$  and  $D_{S0}$  are single particle Einstein diffusion coefficients. This result is valid on time scales which are long compared to the particles' viscous damping times and short compared to the time it takes a particle to diffuse an interparticle spacing. Note the absence of an interspecies diffusion coefficient  $D_{LS}$  in Eq. (4.5). This term appears only after including hydrodynamic effects, and even then, it is diminished by a multiplicative factor  $S_{LS}(y)$ , which approaches 0 at large- $y$ . In a multiple scattering experiment, all wave vectors contribute, and the observed diffusion coefficient is obtained by averaging Eq. (4.5) over all scattering angles

$$D_{eff} = \frac{D_{L0} [F_L(y)] \rho_L + D_{S0} [F_S(y)] \rho_S}{[I(y)] \rho}, \quad (4.6)$$

where [28]

$$[X(y)] = \int_0^{2k_0 a_L} X y^3 dy. \quad (4.7)$$

The dot-dashed line in Fig. 4.3 shows that calculations of  $D_{eff}$  based on Eq. (4.6) inadequately describe our data at all but the smallest  $\phi_S$ . To improve our description of the data, we must include the hydrodynamic interactions between particles.

Since the hydrodynamic force between two particles depends on their separation [29,30], the particle diffusion coefficients in Eq. (4.5) are  $y$ -dependent. Unfortunately, there are at present no calculations for the  $y$ -dependence of  $D_L(y)$  and  $D_S(y)$  [31]. The infinite- $y$  limit, however, where  $D(y)$  is equivalent to the short-time self-diffusion coefficient, has been calculated by Batchelor [1]. To linear order in the volume fraction, the self-diffusion coefficients in a binary system are given by

$$\begin{pmatrix} D_L/D_{L0} \\ D_S/D_{S0} \end{pmatrix} = \mathbf{1} - \begin{pmatrix} m_{LL} & m_{LS} \\ m_{SL} & m_{SS} \end{pmatrix} \begin{pmatrix} \phi_L \\ \phi_S \end{pmatrix}, \quad (4.8)$$

where Batchelor's calculations indicate that the hydrodynamic coupling constants are  $m_{\alpha\beta} \simeq B/(1 + a_\beta/a_\alpha)$  with  $B \approx 3.75$  [32]. This beautifully simple result had

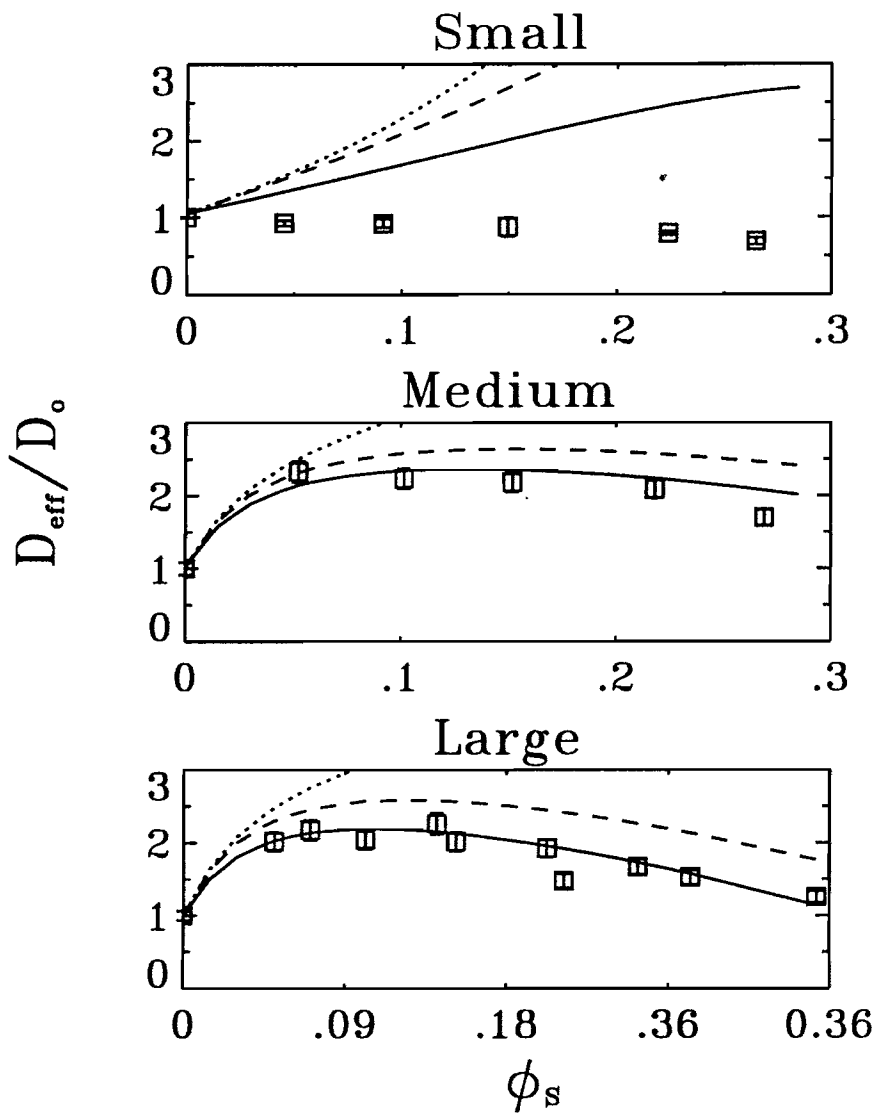


Figure 4.3: Hydrodynamic interactions decrease the effective diffusion constant. The solid line is the fully coupled theory, with  $m_{\alpha\beta}$  given by Eq. (4.8). The dashed line ignores forces between balls of different sizes ( $m_{\alpha\beta} = \delta_{\alpha\beta}B/2$ ), and the dotted line ignores forces between particles ( $m_{\alpha\beta} = 0$ ). The dramatic failure of the theory for the small system indicates the importance of having a full wavelength dependent hydrodynamic theory.

never been experimentally tested. Since we lack a  $y$ -dependent theory for binary systems, we incorporate hydrodynamic interactions by inserting the infinite- $y$  result of Eq. (4.8) into Eq. (4.6). Note that the  $y^3$  in the averages of Eq. (4.6) weight our measurements towards large- $y$  where  $D(y)$  approaches  $D(\infty)$  [28]; thus, our approximation should be asymptotically correct when the upper cutoff of the integrals in Eqs. (4.2) and (4.6) is large. We vary this upper cutoff  $2k_0a_L$  by changing the absolute particle sizes by a factor of 10, while keeping the relative particle sizes in each mixture constant. Thus, changing the particle size effectively probes the  $y$ -dependence of the dynamics, that is, of  $D_{eff}(y)$ .

The measurements of  $D_{eff}$  in Fig. 4.3 show the effect of increasing the concentration of small particles. For the two larger systems,  $D_{eff}$  rises as the diffusion of the smaller, faster particles becomes dominant. At higher volume fractions, the hydrodynamic couplings cause  $D_{eff}$  to decrease. Part of this decrease results from hydrodynamic interactions between similar particles. To see this, compare the dotted lines, calculated without hydrodynamic coupling ( $m_{\alpha\beta} = 0$ ), to the dashed lines, calculated without interspecies coupling ( $m_{\alpha\beta} = \delta_{\alpha\beta}B/2$ ). The theory with the full hydrodynamic coupling (solid lines) demonstrates that interspecies hydrodynamic coupling is significant for nearly all non-zero  $\phi_S$ . By varying the coupling coefficient  $B$  in the off diagonal elements of Eq. (4.8) and leaving the well tested diagonal elements [24, 28, 33–35] at their exact value of 1.83 [1], we find that the data is best fit by  $B = 5.6 \pm 1.4$  in the medium system and  $B = 3.7 \pm 0.4$  in the large system. Batchelor's predicted value is  $B = 3.75$ . Batchelor's expression is valid for the infinite- $y$ , large  $k_0a_L$  limit, thus it is not surprising that it fails to describe the small-particle system, where  $k_0a_L = 3.3$ . By contrast, Batchelor's theory describes the data well for the large-particle system, where  $k_0a_L = 32$ .

We conclude that Batchelor's expressions appear to possess the correct concentration and asymmetry dependence in the limit for which they are intended (infinite- $y$ )

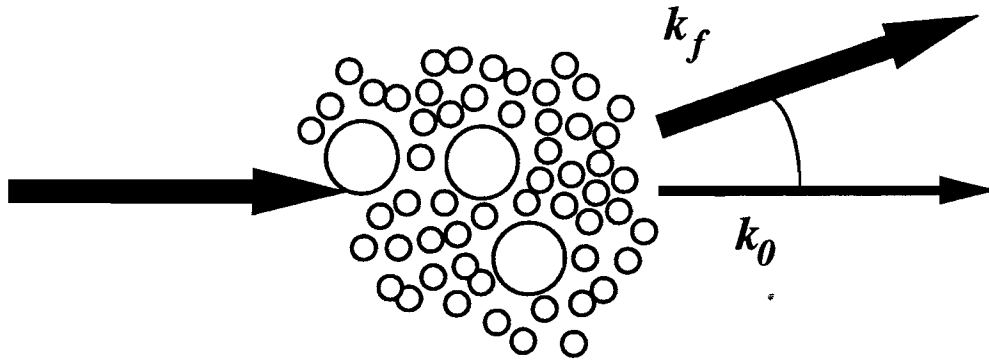


Figure 4.4: Scattering in a binary fluid.

and that a  $y$ -dependent theory for the hydrodynamic interaction is essential to understand smaller systems. Our results illustrate that multiple-scattering spectroscopies are practical probes of polydisperse systems and may be of further use in understanding the dynamics and kinetics of glass formation, freezing, and phase separation in complex fluids.

## 4.2 Calculating $l^*$ in a Binary Mixture

Photon transport in a polydisperse mixture is certainly more complex than in a monodisperse system. In Chapter 2,  $l^*$  was derived from considerations of the single scattering intensity  $I(\theta)$ . In a polydisperse system, the same derivation holds, but the intensity function is more complex. In this section, the previously mentioned result (4.6) will be developed.

The single scattering intensity is calculated as in (2.2) by adding the fields scattered from a group of particles

$$\mathbf{E}_{sc} = (\mathbf{E}_0/\sqrt{4\pi R^2}) \sum_i (f_1^i \hat{e}_1 + f_2^i \hat{e}_2) e^{i\mathbf{y} \cdot \mathbf{r}_i/a}, \quad (4.9)$$

where the polarization is resolved along the unit vectors  $\hat{e}_1$ , and  $\hat{e}_2$ , the scattering amplitudes are  $f$ , and an arbitrary phase is neglected. The scattered intensity is

obtained by squaring the field

$$\begin{aligned}
 I_{sc} &= I_0 \sum_{i,j} (f_1^i \hat{e}_1 + f_2^i \hat{e}_2)(f_1^{*j} \hat{e}_1 + f_2^{*j} \hat{e}_2) e^{i\mathbf{y} \cdot (\mathbf{r}_i - \mathbf{r}_j)/a} \\
 &= I_0 \sum_{i,j} (f_1^i f_1^{*j} + f_2^i f_2^{*j}) e^{i\mathbf{y} \cdot (\mathbf{r}_i - \mathbf{r}_j)/a}.
 \end{aligned} \tag{4.10}$$

The form factor for a monodisperse sample is  $F(\mathbf{y}) = (f_1 f_1^* + f_2 f_2^*)$ . In a binary sample the amplitudes are either  $f^L$  or  $f^S$ , and the form factors sum to either  $F_L(\mathbf{y})$ ,  $F_S(\mathbf{y})$ , or  $\text{Re}(f_1^L(\mathbf{y}) f_1^{*S}(\mathbf{y}) + f_2^L(\mathbf{y}) f_2^{*S}(\mathbf{y}))$ . The result is that the new intensity function is:

$$\begin{aligned}
 F(\mathbf{y})S(\mathbf{y}) \rightarrow & x F_S(\mathbf{y}) S_{SS}(\mathbf{y}) \\
 & + 2\sqrt{x(1-x)} \text{Re}(f_1^L(\mathbf{y}) f_1^{*S}(\mathbf{y}) + f_2^L(\mathbf{y}) f_2^{*S}(\mathbf{y})) S_{LS}(\mathbf{y}) \\
 & + (1-x) F_L(\mathbf{y}) S_{LL}(\mathbf{y}),
 \end{aligned} \tag{4.11}$$

where  $x = n_S/(n_L + n_S)$  is the fractional number density of the *smaller* balls, and the  $S_{ij}$  are partial structure factors (4.4). Some care must be taken when considering the cross term. For X-ray scattering, the scattered wave has no phase shift, meaning that the amplitudes  $f$  are real; the cross term can be calculated by simply taking the square root of  $(F_S F_L)$ . As a result, the x-ray scattering literature uses a simplified intensity function which is incorrect for Mie scattering. In Mie scattering, there is often a large phase shift, and the form factor in the cross term must be calculated using the complex scattering amplitudes and then added as in (4.11).

Making the substitutions to (4.2) indicated by the form factor in Eq. (4.11) and expressing the total number density  $\rho$  in terms of the volume fractions and diameters of the particles, we have calculated values for  $l^*$  which show good agreement with the data (Fig. 4.2). These calculations obey the rule

$$\frac{1}{l_{eff}^*} = \frac{1}{l_S^*} + \frac{1}{l_L^*} \tag{4.12}$$

at low concentrations. Previous work on multiple scattering binary systems [20] assumed Eq. (4.12), which neglects the interference term included in Eq. (4.11). At

higher concentrations, with  $\alpha \equiv a_S/a_L$  near 1, the results agree with the monodisperse calculation for  $\phi = \phi_S + \phi_L$ .

Ashcroft published [25, 26] the equations for the partial structure factors  $S_{ij}(y)$  based on Lebowitz's exact solution of the Percus-Yevick equation [14]. The actual calculation using Ref. [25] is difficult solely because of several typographical errors in the original paper which were later corrected [26]. There is also an ambiguous equation in the paper. When Ashcroft writes

$$a_1 = \frac{\partial}{\partial \eta_1} f(\eta, \eta_1, \eta_2), \quad (4.13)$$

he means

$$a_1 = \frac{\partial}{\partial \eta_1} f(\eta_1 + \eta_2, \eta_1, \eta_2). \quad (4.14)$$

### 4.3 Interpreting DWS Measurements of Bidisperse Colloids

In a DWS experiment on a monodisperse system, the intensity autocorrelation function of multiply scattered light is (see Section 3.4),

$$\langle I(0)I(\tau) \rangle / \langle I(0)I(0) \rangle = \int_0^\infty ds P(s) e^{-2k_o^2 D_{\text{eff}}(s/l^*)}. \quad (4.15)$$

This is a difficult starting point for complex systems because  $D_{\text{eff}}$  is obtained by *averaging* over both the structure factor and a hydrodynamic factor.

For a system with two distinct types of scattering particles, the results will be somewhat more difficult. The program for developing an analogue to (4.15) is to derive the statistics of the single scattered field, then generalize to the multiply scattered field.

If we could detect the singly scattered field autocorrelation function, it would be

$$\langle E^*(0)E(\tau) \rangle = I_o \left\langle \sum_{i,j} F^{ij}(y) e^{i\mathbf{y} \cdot (\mathbf{r}_k^i(0) - \mathbf{r}_i^j(\tau))} \right\rangle, \quad (4.16)$$

MANUSCRIPT

where the superscripts  $i$  and  $j$  denote particle type, and the  $F$ 's are form factors. We want to calculate the decay of the autocorrelation function in (4.16). In particular, we wish to calculate its first cumulant.

We repeat the calculation outlined in Section 3.6, beginning with the derivative of the field correlation function

$$\frac{d}{d\tau} \langle E^*(0)E(\tau) \rangle = I_0 y^2 \sum_i F^i(y) N_i D_i, \quad (4.17)$$

where  $F^i$  is either the large or small form factor. The cross terms include the integral  $\int v_L(t)v_S(t+\tau)dt$ , which is generally zero. Going beyond this approximation requires the use of techniques such as those employed by Nagele and Klein [36–38].

Following Ashcroft and Langreth's work [25] on the structure factors of binary liquids, we express  $\langle E^*(0)E(\tau) \rangle \equiv NI(y)$  as

$$I(y) = (1-x)F_L(y)S_{LL}(y) + 2\sqrt{x(1-x)}F^{LS}(y)S_{LS}(y) + xF_S(y)S_{SS}(y), \quad (4.18)$$

where  $x$  is the fractional number density of small particles, and  $F^{LS}(y)$  is given in (4.11) as  $\text{Re}(f_1^L(y)f_1^{*S}(y) + f_2^L(y)f_2^{*S}(y))$ . Combining (3.32), (4.17), and (4.18) we find

$$D_{\text{eff}}(y) = \frac{(1-x)F^L(y)D_L + xF^S(y)D_S}{I(y)}. \quad (4.19)$$

This result defines the effective diffusion coefficient that light scattering is sensitive to. Now we can interpret the DWS results using this  $D_{\text{eff}}$  and (4.15).

DWS, of course, measures not  $D_{\text{eff}}(y)$  but a  $y$ -averaged diffusion coefficient  $\langle D_{\text{eff}}(y) \rangle_\Omega$ . We will now repeat the development of the DWS correlation function in Section 3.3, including the complications of a binary sample. In a DWS measurement, fluctuations are due not to one, but many ( $\simeq 10^2 - 10^4$ ) independent scattering events. Thus, the average fluctuations have a field correlation function

$$\langle E^*(0)E(\tau) \rangle = \langle I(y) e^{-y^2 D_{\text{eff}} \tau} \rangle_\Omega^N, \quad (4.20)$$

where  $N = s/l$  is the number of scattering events. Working to first order in the

cumulant expansion we find

$$\langle E^*(0)E(\tau) \rangle = I(y)^{s/l} e^{-\langle y^2(xF^S(y)D_S + (1-x)F^L(y)D_L)/S(y) \rangle \Omega \tau s/l}. \quad (4.21)$$

We interpret the exponent as  $\langle y^2 \rangle_{\Omega} D_{\text{eff}} \tau s/l^*$ . The  $D_{\text{eff}}$  derived from the experiment is calculated as follows. All averages are with respect to the weighting function  $I(y)$ . Analogous to the monodisperse calculation (Eq. (3.11)), we use  $s/l = (s/l^*)(l^*/l)$ , where the first ratio is measurable, and the second ratio is calculated using,

$$\frac{l^*}{l} = \frac{2k_o^2 \int_0^{2k_o} I(y)y dy}{\int_0^{2k_o} y^2 I(y)y dy}. \quad (4.22)$$

Thus, the exponent in (4.21) is

$$- \frac{2k_o^2 \left[ xD_S \left( \int_0^{2k_o} y^2 F_S(y)y dy \right) + (1-x)D_L \left( \int_0^{2k_o} y^2 F_L(y)y dy \right) \right] s\tau}{\int_0^{2k_o} y^2 I(y)y dy} \frac{1}{l^*}. \quad (4.23)$$

For a many particle system, this generalizes to

$$- 2k_o^2 \frac{\sum_i x_i D_i \left( \int_0^{2k_o} y^2 F_i(y)y dy \right) s\tau}{\int_0^{2k_o} y^2 I(y)y dy} \frac{1}{l^*}. \quad (4.24)$$

Allowing this expression to define our averaging technique, we use square brackets  $[\ ]$  defined by

$$[X] = \frac{\int_0^{2k_o} X(y)y^3 dy}{\int_0^{2k_o} I(y)y^3 dy} \quad (4.25)$$

and write the final effective diffusion coefficient

$$[D_{\text{eff}}] = \sum_i x_i [F_i] D_i. \quad (4.26)$$

This is the quantity that DWS measures. It is an average of large and small diffusion coefficients weighted by the particles' form factors and  $S_{ij}(q)$ .

## 4.4 Binary Structure Functions

While we have shown the utility of the Percus-Yevick structure function for binary hard-spheres, it is instructive to actually look at graphs of the binary structure

functions. A large set of these graphs are produced in the original paper on the subject [25], but these graphs focus on attainable atomic liquids in which the ratio of diameters is never very large. In Fig. 4.5, we see partial structure factors for systems with larger diameter ratios. Note in particular the broad peak in  $S_{SS}(y)$  at low  $y$  and large diameter ratios. Theoretically, if that peak height was infinite, it would be an indication of phase separation. In Chapter 5, we will see that phase separation does occur and thus, the Percus-Yevick result underestimates the height of the zero- $y$  peak in  $S(y)$ .

## 4.5 Stokes Flow and Hydrodynamics in Binary Systems

In Section 4.1, we saw experimentally that interactions between particles moderated by the water in which they are suspended result in a decrease in the self-diffusion coefficient of Brownian particles. In this section, we will review some of theory of this effect. Along with the experimental results, we asserted that the theory for hydrodynamic coupling could be approximated by Eq. (4.8). In this section Eq. (4.8) will be more solidly motivated.

The complication of diffusion in concentrated systems is the connection between collective and self diffusion (section 3.6). The conceptual distinction between the two types of diffusion is straightforward: one refers to the motion of individual particles, and the other refers to collective density fluctuations. The constitutive connection is made by tying together well understood factors such as the simple physics of self-diffusion, the hydrodynamic interactions between the motion of one particle and the fluid flow at another particle, and the statistical forces arising from local concentration fluctuations. This constitutive connection is extremely difficult to describe, calculate, or understand. As a result of this confusion, the literature includes a mix of real-space and Fourier space descriptions which are difficult to

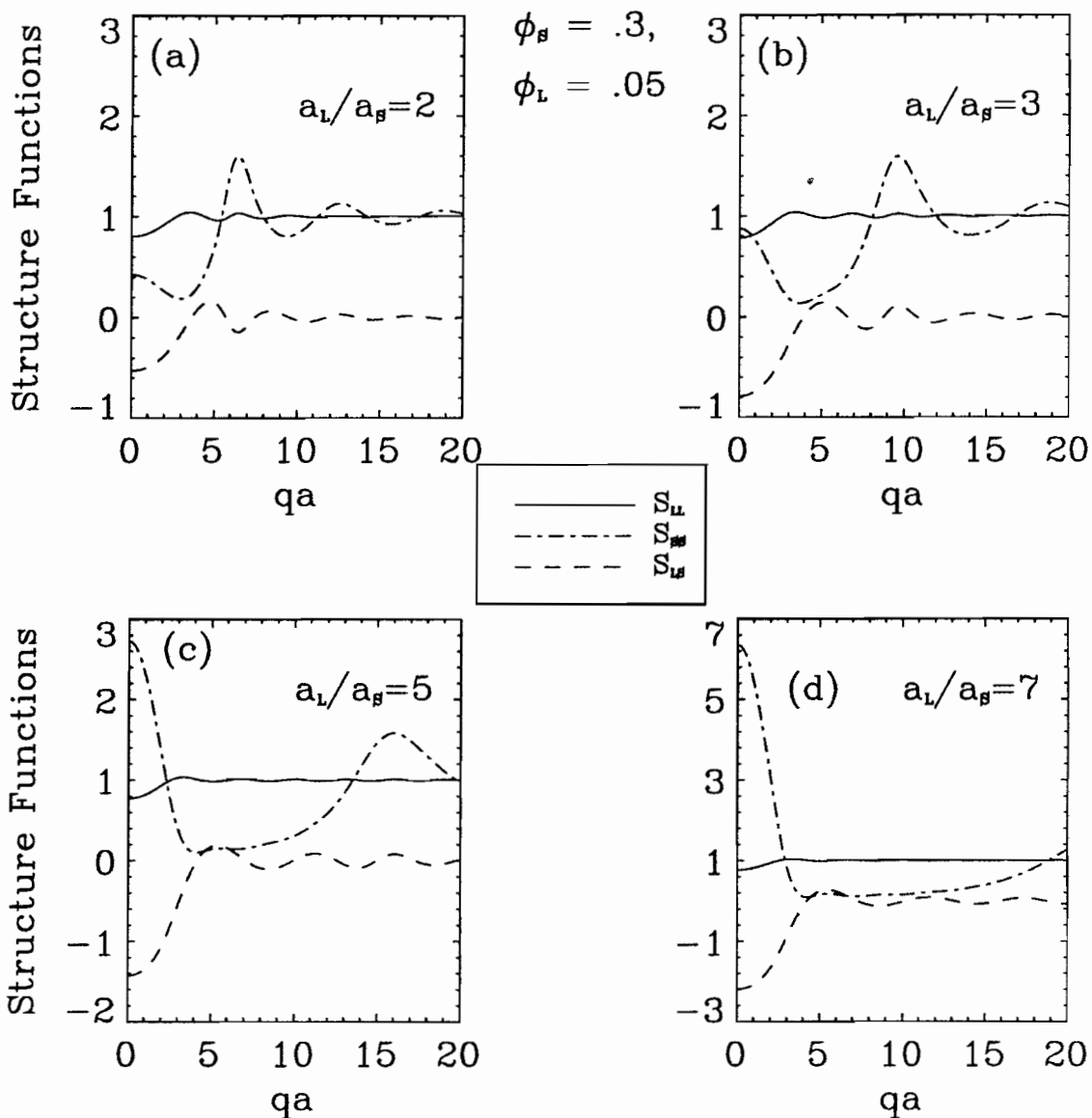


Figure 4.5: Partial Structure Factors for Binary Mixtures. In this figure the volume fraction of large particles is .05, and the volume fraction of small particles is 0.3. The Percus-Yevick structure factors are plotted as a function of wave-vector for (a) a diameter ratio of 2, (b) a diameter ratio of 3, (c) a diameter ratio of 5, and (d) a diameter ratio of 7. Note the change in scale as the low- $q$  peak grows with diameter ratio. This is suggestive of phase separation behavior seen in Chapter 5.

reconcile with each other. Further, the key result for monodisperse systems (that the self-diffusion coefficient is reduced by a factor of  $1 - 1.83\phi$ ) is embedded in an erroneous discussion [1]. This paragraph is my apology for failing to deeply understand or repeat the derivation of Eq. (4.8). The key feature of this theory is that it is a two particle, not a multi-particle theory. It is remarkable that it works as well as it does.

A strong and fundamentally correct description, however, of the derivation of Eq. (4.8) will now be reviewed. We begin near the end of the derivation in [1] with the fundamental result

$$D_1(\phi) = D_1(\phi = 0) \left\{ 1 - \left( \frac{1 + \lambda}{2\lambda} \right)^3 C(\lambda) \right\}, \quad (4.27)$$

where  $D_1(\phi = 0) = kT/6\pi\eta(a/2)$ , and  $\lambda = a_2/a_1$  is either the diameter ratio  $\alpha$  or  $1/\alpha$ , depending on whether we are calculating the diffusion coefficient for the large or small particle. Finally,  $C(\lambda)$  is an average drag coefficient that we will discuss below.

Stokes flow is laminar flow past a sphere; it is widely discussed in elementary fluid mechanics texts (*e.g.*, Ref. [39]). The Stokes drag  $\gamma_0 = 1/6\pi\eta(a/2)$  is widely employed for applications such as viscosity measurements based on the terminal velocity of a falling sphere. Batchelor's approach to the hydrodynamic interaction between two particles is to introduce the force on a particle by modifying the particle's drag coefficient. That is, if a particle is moving in a fluid that is not at rest, but at a velocity of  $u$ , the particle appears to have a drag coefficient of  $\gamma_0 - u$ . The velocity field is traditionally broken down into two parts of different symmetry.  $A_{11}$  and  $B_{11}$  refer to the factor by which the velocity field in the presence of a neighbor differs from the Stokes result.  $A$  and  $B$  refer to each of the two symmetries. Although quite complicated in detail, the drag coefficients have fairly simple asymptotic forms

$$A_{11} = 1 - \frac{60\lambda^3}{(1 + \lambda)^4 \rho^4} + \mathcal{O}(\rho^{-6}) \quad (4.28)$$

$$B_{11} = 1 + \mathcal{O}(\rho^{-6}), \quad (4.29)$$

where  $\rho = r/(a_1 + a_2)$  is the dimensionless distance between spheres. In the absence

of the second particle,  $A_{11}$  and  $B_{11}$  are just 1, indicating Stokes flow and the usual Einstein self-diffusion coefficient  $D_0 = kT/6\pi\eta(a/2)$ .

To calculate the new self-diffusion coefficient, Batchelor averages the drag coefficients  $A_{11}$  and  $B_{11}$  over all of the possible positions of particle 2. In so doing, he finds a geometric factor of  $[(1 + \lambda)/2\lambda]^3$  and a hydrodynamic factor of

$$C(\lambda) = \phi_2 \int_2^\infty [3 - A_{11}(\rho, \lambda) - 2B_{1,1}(\rho, \lambda)] \rho^2 d\rho. \quad (4.30)$$

By integrating (4.30) using the asymptotic forms of the mobility factors (4.29) we arrive at

$$C(\lambda) \approx \phi_2 \frac{30\lambda^3}{(1 + \lambda)^4}, \quad (4.31)$$

which, when combined with the geometric factor, results in a reduction in the diffusion coefficient by  $1 - \frac{3.75}{1+\lambda}\phi_2$ . This is the factor that appears in Eq. (4.8).

To evaluate the accuracy of using just the asymptotic forms of the mobility factors  $A_{11}$  and  $B_{11}$ , we can consider the one case in which they have been calculated exactly. For a monodisperse system, the integral in Eq. (4.30) has been numerically integrated using the full forms of  $A_{11}$  and  $B_{11}$ . The result is  $1.83\phi_2$ . Using our approximation, the result is  $1.85\phi_2$ , a difference of 2.5%. As we have measured the numerator (estimated as 3.75) for coupling between large and small balls to be  $3.7 \pm .4$ , the approximation introduced by relying on the asymptotic forms of  $A_{11}$  and  $B_{11}$  introduces errors far smaller than the experimental uncertainty.

# Bibliography

- [1] G. K. Batchelor, *Brownian Diffusion of Particles with Hydrodynamic Interaction*, J. Fluid Mech. **74**, 1 (1976).
- [2] P. Bartlett, R. H. Ottewill, and P. N. Pusey, *Freezing of Binary Mixtures of Colloidal Hard Spheres*, J. Chem. Phys. **93**, 1299 (1990).
- [3] T. Biben and J. P. Hansen, *Phase Separation of Asymmetric Binary Hard-Sphere Fluids*, Phys. Rev. Lett. **66**, 2215 (1991).
- [4] G. K. Batchelor and R. W. J. van Rensburg, *Structure Formation in Bidisperse Sedimentation*, J. Fluid Mech. **16**, 379 (1986).
- [5] Measurements of non-hard-sphere structure were performed by M.H.G. Duits, R.P. May, A. Vrij, and C.G. de Kruif, J. Chem. Phys. **94**, 4521 (1991); H.J.M Hanley, G.C. Straty, and P. Lindner, Physica A **174**, 60 (1991). Polydisperse hard-spheres have been studied by C.G. de Kruif, W.J. Briels, R.P. May, and A. Vrij, Langmuir **4**, 668 (1988).
- [6] T. Okubo, *Alloy Structures in Binary Mixtures of Highly Deionized Colloids at Sedimentation Equilibrium*, J. Chem. Phys. **93**, 8276 (1990).
- [7] A. van Veluwen, H. N. W. Lekkerkerker, C. G. de Kruif, and A. Vrij, *Influence of Polydispersity on Dynamic Light Scattering Measurements on Concentrated Suspensions*, J. Chem. Phys. **89**, 2810 (1988).

- [8] B. J. Alder, *Studies in Molecular Dynamics. III. A Mixture of Hard Spheres*, J. Chem. Phys. **40**, 2724 (1964).
- [9] B. U. Felderhof, *Hydrodynamic interaction between two spheres*, Physica A **89**, 373 (1977).
- [10] J. L. Barrat, M. Baus, and J. P. Hansen, *Freezing of Binary Hard-sphere Mixtures into Disordered Crystals: a Density Functional Approach*, J. Phys. C **20**, 1413 (1987).
- [11] H. Xu and M. Baus, *The Partial Freezing of Hard-sphere Mixtures*, J. Phys. C **20**, L373 (1987).
- [12] W. G. T. Kranendonk and D. Frenkel, *Computer Simulation of Solid-liquid Coexistence in Binary Hard Sphere Mixtures*, Mol. Phys. **72**, 679 (1991).
- [13] P. N. Pusey, H. M. Fijnaut, and A. Vrij, *Mode Amplitudes in Dynamic Light Scattering by Concentrated Liquid Suspensions of Polydisperse Hard Spheres*, J. Chem. Phys. **77**, 4270 (1982).
- [14] J. L. Lebowitz, *Exact Solution of Generalized Percus-Yevick Equation for a Mixture of Hard Spheres*, Phys. Rev. **133**, A895 (1964).
- [15] M. J. Stephen, *Temporal Fluctuations in Wave Propagation in Random Media*, Phys. Rev. B **37**, 1 (1988).
- [16] G. Maret and P. E. Wolf, *Multiple Light Scattering from Disordered Media. The Effect of Brownian Motion of Scatterers*, Z. Phys. B **65**, 409 (1987).
- [17] D. J. Pine, D. A. Weitz, P. M. Chaikin, and E. Herbolzheimer, *Diffusing-Wave Spectroscopy*, Phys. Rev. Lett. **60**, 1134 (1988).
- [18] N. W. Ashcroft and D. C. Langreth, *Structure of Binary Liquid Mixtures. II. Resistivity of Alloys and the Ion-Ion Interaction*, Phys. Rev. **159**, 500 (1968).

- [19] J. M. Ziman, *A Theory of the Electrical Properties of Liquid Metals I: The Monovalent Metals*, Philos. Mag. **6**, 1013 (1961).
- [20] D. J. Pine, D. A. Weitz, J. X. Zhu, and E. Herbolzheimer, *Diffusing-Wave Spectroscopy: Dynamic Light Scattering in the Multiple Scattering Limit*, J. Phys. France **51**, 2101 (1990).
- [21] A. Ishimaru, in *Wave Propagation and Scattering in Random Media* (Academic Press, New York, 1978).
- [22] L. Tsang, J. A. Kong, and T. Habashy, *Multiple scattering of acoustic waves by random distribution of discrete spherical scatterers with the quasicrystalline and Percus-Yevick approximation*, J. Acoust. Soc. Am. **71**, 552 (1982).
- [23] A. Ishimaru and Y. Kuga, *Attenuation constant of a coherent field in a dense distribution of particles*, J. Opt. Soc. Am. **72**, 1317 (1982).
- [24] S. Fraden and G. Maret, *Multiple Light Scattering from Concentrated Interacting Suspensions*, Phys. Rev. Lett. **65**, 512 (1990).
- [25] N. W. Ashcroft and D. C. Langreth, *Structure of Binary Liquid Mixtures I*, Phys. Rev. **156**, 685 (1967).
- [26] N. W. Ashcroft and D. C. Langreth, *Errata to Structure of Binary Liquid Mixtures I*, Phys. Rev. **166**, 934 (1968).
- [27] P. N. Pusey and R. J. A. Tough, in *Dynamic Light Scattering* (Plenum, New York, 1985).
- [28] X. Qiu *et al.*, *Hydrodynamic Interactions in Concentrated Suspensions*, Phys. Rev. Lett. **65**, 516 (1990).
- [29] B. U. Felderhof, *Diffusion of Interacting Brownian Particles*, J. Phys. A **11**, 929 (1978).

- [30] R. B. Jones, *Diffusion of Tagged Interacting Spherically Symmetric Polymers*, Physica A **97**, 113 (1979).
- [31] C. W. J. Beenakker and P. Mazur, *Diffusion of Spheres in a Concentrated Suspension II*, Physica **126A**, 349 (1984).
- [32] We derive this from asymptotic expressions in Ref. [1]. The full theory is significantly more complex, but the predictions are not very different ( $< 3\%$ ) for  $\alpha = 1$ .
- [33] A. G. Yodh, P. D. Kaplan, and D. J. Pine, *Pulsed Diffusing-Wave Spectroscopy: High Resolution through Nonlinear Optical Gating*, Phys. Rev. B **42**, 4744 (1990).
- [34] A. P. Philipse and A. Vrij, *Determination of Static and Dynamic Interactions Between Monodisperse Charged Silica Spheres in an Optically Matching Organic Solvent*, J. Chem. Phys. **88**, 6459 (1988).
- [35] A. van Veluwen, H. N. W. Lekkerkerker, C. G. de Kruif, and A. Vrij, *Measurement of the Short Time Self-diffusion Coefficient in Dilute and Concentrated Suspensions: Influence of Direct Particle Interactions*, J. Chem. Phys. **87**, 4873 (1987).
- [36] G. Nagele, O. Kellerbauer, R. Krause, and R. Klein, *Hydrodynamic effects in polydisperse charged colloidal suspensions at short times.*, Phys. Rev. E, Stat. Phys. Plasmas Fluids Relat. Interdiscip. Top. (USA). **47**, 2564 (1993).
- [37] R. Krause *et al.*, *Statics and tracer-diffusion in binary suspensions of polystyrene spheres: experiment vs. theory.*, Physica A (Netherlands). **178**, 241 (1991).
- [38] R. Krause *et al.*, *Static structure factors of binary suspensions of charged polystyrene spheres: experiment against theory and computer simulation.*, J. Phys., Condens. Matter. (UK). **3**, 4459 (1991).

[39] D. J. Tritton, *Physical Fluid Dynamics* (van Nostrand Reinhold Co., New York, 1977).

# Chapter 5

## Phase Separation in Binary Colloids

### 5.1 Introduction and Survey

Freezing and crystallization are generally driven by the deep potential minima of chemical and physical bonds that overwhelm the entropic tendency towards disorder. In some cases, however, entropy can actually induce order and cause a liquid to freeze. While this seems counterintuitive, such entropy-driven freezing transitions have been observed for many years in computer simulations of atoms interacting through a purely repulsive hard-sphere potential [1]. Recently, this freezing transition was observed experimentally in monodisperse, hard-sphere colloidal suspensions [2]. For liquids and suspensions made up of single-size spheres, freezing is observed when the volume fraction  $\phi$  of spheres exceeds approximately 0.49.

In this chapter, we show that for binary mixtures of hard-sphere colloidal particles, entropically-driven phase transitions can occur at substantially lower total volume fractions than for monodisperse samples. More importantly, we find that such phase transitions can involve coexistence between two bulk disordered phases (rather than freezing) or coexistence between bulk disordered phases and a *new*

*crystalline phase*, which precipitates on the walls of the sample. We believe this new ordered phase is also entropically driven, and we provide arguments suggesting that phase separation in hard sphere mixtures should always occur at the sample walls before occurring in the bulk, in agreement with our experimental observations. This entropically-driven ordering of particles at the sample walls may be relevant in paints, polydisperse colloids in porous media, and in catalytic systems, which sometimes employ dispersions at reactive surfaces.

Until recently, binary hard sphere mixtures of all size ratios were expected to be completely miscible in the fluid phase. Calculations of the equation of state and static structure factors within the Percus-Yevick approximation show no phase separation [3]. Recent experiments in colloidal suspensions, however, suggest that hard-spheres are sometimes immiscible, although the interpretation of the observations is clouded somewhat by the effects of strong gravitational settling [4,5]. There are also some unambiguous examples of phase separation in binary systems with softer inter-particle potentials, including liquid emulsions [6,7] and mixtures of colloidal particles with linear polymer molecules [8,9]. These experiments have nevertheless been modeled as mixtures of hard-spheres using an effective potential approach which relies on simple geometric arguments to calculate entropic forces [6-9]. These calculations, however, unrealistically treat the small particles as a non-interacting ideal gas. More recent and rigorous theoretical work [10,11] suggests that phase separation should occur in binary mixtures. Unfortunately, these results are either inconclusive because of uncertainty in the choice of a closure relation [10] or incomplete because of the computational effort required to specify where in the phase diagram separation should occur [11].

The effective potential models for structure and phase separation [6-9,12] are based on an argument of Asakara and Oosawa [13] that uses the fact that the free energy in a hard-sphere system is entirely entropic and depends on the volume accessible to the center of each particle. Adding a small volume  $\Delta V$  to an ideal gas of

$N_S$  small particles reduces the free energy,  $F = -kTN_S \ln(V/\lambda^3)$ , by approximately  $kTN_S \Delta V/V$ , where  $\lambda$  is the de Broglie wavelength and  $kT$  is Boltzmann's constant times the temperature. If the volume fractions  $\phi_S$  and  $\phi_L$  of small and large particles are comparable, and the ratio  $a_S/a_L$  of small to large particle diameters is small, there will be many more small particles than large particles. In this limit, the small particles will provide the dominant contribution to the free energy (and entropy) of the system. Since the center of each small particle is excluded from a sphere of diameter  $a_L + a_S$  around each large particle (see Fig 5.1a), the volume available to each small particle is reduced by the presence of the large particles. However, Asakara and Oosawa [13] pointed out that the total volume available to small particles *increases* when two large particles approach each other so that the spheres of excluded volume overlap (see Fig. 5.1a and b). This decreases the free energy of the mixture and produces an effective potential well with a depth of approximately  $(3/2)(a_L/a_S)\phi_S kT$ . Motivated by our observations of a new surface phase, we apply the same geometric argument to large particles near a flat wall (Fig 5.1c). To our surprise, we find that the potential of a large particle near a wall is nearly *twice* as deep as the potential between two large balls [14] when  $a_S/a_L \ll 1$ . A large particle caught in this entropic well, which has a depth of approximately  $3(a_L/a_S)\phi_S kT$ , will be confined to lie with its surface within one small ball diameter of the wall, thus making an effectively 2-dimensional fluid of large particles.

In our experiments, we investigated the phase diagram of nearly hard-sphere binary colloidal suspensions for nine different diameter ratios and for a large number of volume fractions of large and small spheres. Our approach is straightforward. We mixed commercially prepared polystyrene particles of various sizes and observed them visually over the course of several days. These systems are charge stabilized with a screening length of roughly 4 nm and total volume fractions generally less than 0.30. They are good, though imperfect models of hard-sphere systems. The mixtures were placed in 1-mm-thick cuvettes and observed over the course of several

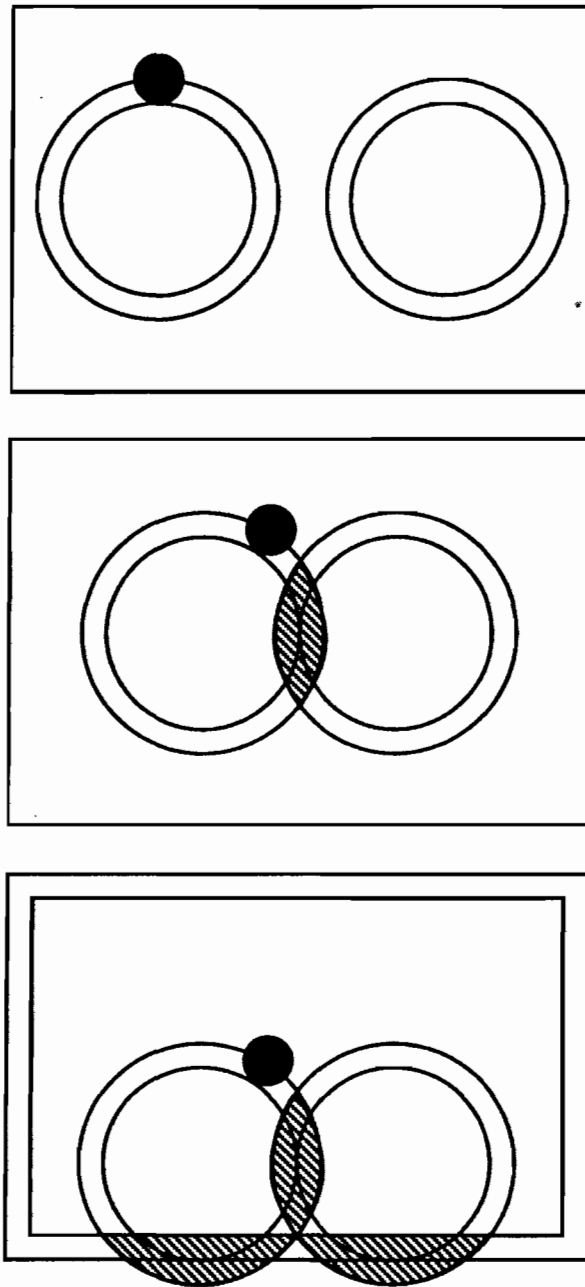


Figure 5.1: Geometric Explanation of Binary Hard-Sphere Phase Separation: The free energy of an ideal gas of  $N_S$  small particles is  $-kTN_S \ln V/\lambda^3$ , where  $V$  is the volume accessible to the center of each small particle. (a) That volume does not include a sphere around each large particle with a diameter equal to the sum of the large and small particle diameters. (b) When large particles approach each other, some of the excluded volume overlaps, effectively making a small increase in the volume available to the small particles. This decreases the free energy by approximately  $kTN_S(\Delta V/V)$ . (c) The same effect occurs as a large particle approaches a wall, but  $\Delta V$  is approximately twice as large.

hours. In some of our samples, we monitored the diffuse transmission of a laser beam through the samples as a function of time in order to detect changes in bulk structure [15]. We found, however, that the final states were readily visible by eye, making real-time monitoring of the diffuse transmission unnecessary. We observed four final states: (1) a single homogeneous disordered phase, (2) coexistence between two disordered bulk phases, (3) coexistence between a disordered bulk phase and a crystalline phase localized on the sample walls, and (4) coexistence between two disordered bulk phases and a surface crystalline phase. *Bulk* crystallization, characterized by Bragg scattering from an extended volume of the sample *not* restricted to a thin layer near the walls, was not observed. In samples in which phase separation occurred, the different phases were often visible by eye within 12 hours, and almost always within 48 hours. None of these separated states was observed in monodisperse samples at similar total volume fractions.

The homogeneous systems (state 1) exhibited neither change visible by direct visual observation nor change detectable with diffusing-wave spectroscopy [16, 17] over a period of at least two weeks.

Bulk separation into two disordered phases (observed in states 2 and 4) was characterized by the sample separating into upper and lower layers which differed in optical opacity. The two layers were separated by a sharp boundary. These layers could usually be seen under ambient light, but were occasionally detectable only when the cell was illuminated from behind with white light. The optical contrast between phases arises primarily because of the difference in the concentration of the large 460-nm-diameter spheres in the two phases; the large spheres have a very large optical cross section compared to the small 65-nm-diameter spheres [18].

The crystalline surface phase (observed in states 3 and 4) was characterized by the presence of Bragg scattering from discrete areas on the surface. Under an optical microscope, these areas appear as polycrystalline faceted regions exhibiting different colors, with facets as large as a few millimeters across (see Fig. 5.2). The colors

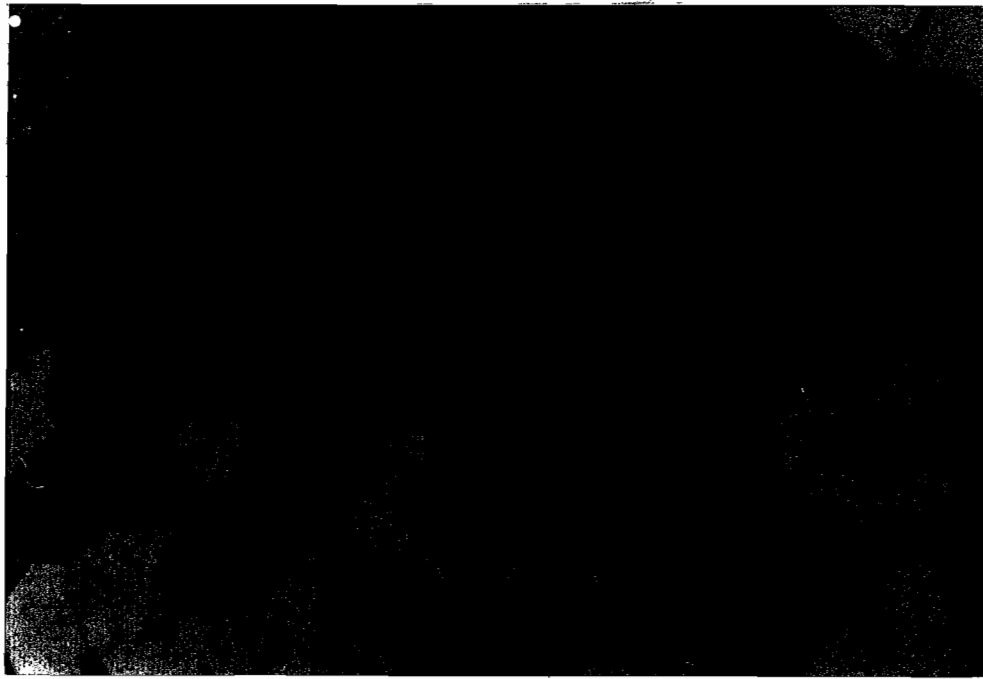


Figure 5.2: Surface crystallites as viewed under an optical microscope.

arise from Bragg scattering from the crystallite; different colors most likely indicate different crystalline orientations with respect to container walls. The structure of these crystals has not been determined. While the thickness of the crystallites is difficult to ascertain *in situ*, crystallites scraped from the wall, dried, and observed with an electron microscope were less than 5 large sphere diameters thick. Diffusing-wave spectroscopy was used to qualitatively examine the dynamics of the surface phase *in situ*. In contrast to correlation functions obtained from the non-crystalline regions, the diffusing-wave spectroscopy autocorrelation functions of light scattered from crystallites never decayed to zero. This indicates that the motion of the scattering particles is confined by the crystal lattice [17].

We believe that the surface crystals form because of a combination of factors: the enhanced concentration of large balls along the wall is caused by the large entropic

well near the wall described earlier, and the crystals arise because of entropic attraction between large spheres in the surface layer. Once nucleated, the two-dimensional crystallite may seed additional crystalline layers extending a short distance into the bulk. However, significant work is needed to establish the detailed structure of the surface phase and its growth into the bulk.

There are three axes in the phase diagram for these systems: the ratio of particle diameters  $a_S/a_L$  and the volume fractions of each species  $\phi_L$  and  $\phi_S$ . A number of diameter ratios were investigated (Tbl. 5.1); one system (460/65 nm) has been explored in detail. Phase separation was not observed in samples with both a diameter ratio less than 7 and total volume fraction less than 0.3. We found that the surface phase (Fig. 5.3) always separates at *lower* volume fractions than the bulk, consistent with the relatively stronger attraction of large particles to the wall in our model. At the highest volume fractions, above the upper line in Fig. 5.3, the dynamics of phase separation were very slow, taking more than five days, suggesting that the samples may have been in a glassy state or that they may not have reached thermodynamic equilibrium.

In samples above the upper line in Fig. 5.3 the solid grown on the cell walls consisted of small white spots, which did not display Bragg scattering. Monodisperse hard-sphere systems also display wetting by an ordered phase, but the wetting occurs at concentrations very near the bulk freezing transition [19], in sharp contrast to the binary system.

It is useful to compare our results with those of a similar experiment, reported recently by van Duijneveldt, Heinen, and Lekkerkerker (DHL) [4], in which binary mixtures of polymer-stabilized silica spheres in cyclohexane were studied. In the DHL experiment, bulk phase separation was observed similar to the bulk separation we observe. However, no surface crystalline phase was reported. In contrast to the system studied by DHL, the polystyrene system we use exhibits much slower particle settling, more optical scattering, and a somewhat less ideally hard-sphere interaction

PHOTOCOPIED

Table 5:1: Systems studied: systems in which phase separation was observed in at least one sample are denoted by S (surface phase separation) or B (bulk separation). All lengths in are in nanometers. Almost all samples were at total volume fractions below 0.30.

$a_L$ (nm)	$a_S$ (nm)	$\phi_L$	$\phi_S$	Final State
299	65	0.13	0.09	-
299	65	0.13	0.10	-
299	65	0.13	0.11	-
299	65	0.13	0.13	-
299	65	0.13	0.15	-
299	65	0.13	0.17	-
460	137	0.13	0.13	-
460	137	0.13	0.15	B
460	137	0.13	0.17	-
460	65	0.01	0.19	S
460	65	0.0125	0.0625	-
460	65	0.02	0.28	-
460	65	0.03	0.03	-
460	65	0.03	0.05	-
460	65	0.03	0.07	-
460	65	0.03	0.11	-
460	65	0.03	0.15	-
460	65	0.03	0.16	-
460	65	0.03	0.16	S
460	65	0.03	0.18	S
460	65	0.03	0.22	S
460	65	0.03	0.25	S
460	65	0.03	0.27	S
460	65	0.03	0.27	S?
460	65	0.05	0.01	-
460	65	0.05	0.05	-
460	65	0.05	0.09	-
460	65	0.05	0.13	-
460	65	0.05	0.14	-
460	65	0.05	0.15	?
460	65	0.05	0.15	S
460	65	0.05	0.15	S
460	65	0.05	0.16	S
460	65	0.05	0.18	S
460	65	0.05	0.20	S
460	65	0.05	0.225	SB

Table 5.2: Previous table continued.

$a_L$ (nm)	$a_S$ (nm)	$\phi_L$	$\phi_S$	Final State
460	65	0.05	0.25	S
460	65	0.052	0.278	S
460	65	0.06	0.312	-
460	65	0.06	0.364	B
460	65	0.0605	0.258	SB
460	65	0.07	0.25	SB
460	65	0.09	0.21	SB
460	65	0.112	0.165	SB
460	65	0.112	0.186	SB
460	65	0.13	0.01	-
460	65	0.13	0.01	-
460	65	0.13	0.01	-
460	65	0.13	0.05	-
460	65	0.13	0.05	-
460	65	0.13	0.05	-
460	65	0.13	0.07	-
460	65	0.13	0.07	-
460	65	0.13	0.09	S
460	65	0.13	0.1	-
460	65	0.13	0.10	-
460	65	0.13	0.10	-
460	65	0.13	0.10	S
460	65	0.13	0.11	S
460	65	0.13	0.11	S
460	65	0.13	0.12	S
460	65	0.13	0.12	S
460	65	0.13	0.12	S
460	65	0.13	0.13	S
460	65	0.13	0.13	S
460	65	0.13	0.13	S
460	65	0.13	0.15	SB
460	65	0.133	0.062	-
460	65	0.133	0.071	-
460	65	0.133	0.071	-
460	65	0.133	0.111	S
460	65	0.133	0.133	S
460	65	0.15	0.08	?
460	65	0.15	0.10	-
460	65	0.15	0.11	S

Table 5.3: Previous table continued.

$a_L$ (nm)	$a_S$ (nm)	$\phi_L$	$\phi_S$	Final State
460	65	0.15	0.11	S
460	65	0.15	0.12	S
460	65	0.15	0.13	S
460	65	0.15	0.14	S
460	65	0.15	0.14	S
460	65	0.15	0.15	SB
605	102	0.05	0.25	-
605	102	0.025	0.125	S
605	65	0.025	0.125	S
605	65	0.05	0.25	B
605	65	0.05	0.25	S
625	65	0.13	0.08	S
625	65	0.13	0.09	S
625	65	0.13	0.13	S
625	65	0.20	0.09	S
625	65	0.20	0.10	S
825	102	0.01	0.29	?
825	102	0.03	0.25	S
825	102	0.05	0.08	-
825	102	0.05	0.20	S
825	102	0.05	0.25	S
825	137	0.05	0.25	-
825	65	0.0125	0.0625	SB
825	65	0.025	0.125	S
825	65	0.025	0.125	S
825	65	0.03	0.01	-
825	65	0.05	0.05	-
825	65	0.05	0.25	B
825	65	0.13	0.07	S
825	65	0.13	0.08	B?
825	65	0.13	0.09	S
825	65	0.13	0.10	S
945	65	0.0125	0.0125	-
945	65	0.025	0.125	S,B
945	65	0.025	0.225	S
945	65	0.05	0.05	-
2000	65	0.05	0.225	B

potential. The details of the DHL experiment explain why the surface phase may not have been observed. First, the rate at which the surface phase separation proceeds in our experiments is slow compared to the settling times in the DHL experiments but fast compared to the monodisperse settling time in this experiment. The density of polystyrene, 1.05 g/ml, is much closer to that of our solvent, water, than the densities of the silica spheres, 1.81 and 1.51 g/ml, are to the density of cyclohexane, 0.78 g/ml. Since the settling rate of particles is proportional to the buoyancy, which is the difference in mass between a particle and an equal volume of solvent, settling proceeds much faster in the DHL system than in ours where the buoyancy is twenty times smaller. As a consequence, settling times in the silica system are a few hours, which is comparable to the time required for phase separation, while the settling times of the polystyrene system are significantly slower (*i.e.*, days), which allows the slow dynamics of phase separation to proceed. The optical scattering power of individual spheres is also much higher since the index mismatch for polystyrene in water  $n_{particle}/n_{solvent}$  is 1.59/1.32 rather than 1.46/1.43. The silica/cyclohexane system is generally prized for its weak scattering, which allows the use of single scattering optical techniques at high volume fractions. For surface sensitivity, strong scattering is desirable.

In order to investigate the reversibility of the bulk phase separation that we observed, we stirred samples by tumbling and placing them in an ultrasonic bath. Their behavior repeated exactly; even when monitoring the intensity of transmitted light through the sample, the same time dependence was observed to within a few percent.

The fluid-solid transition is also reversible. Crystallites, which can be removed from the surface by vigorous shaking, grow back when the shaking stops. To check for irreversible flocculation, we diluted the suspension surrounding the crystals and watched under a microscope; the crystallites dissolved in less than a minute, demonstrating convincingly that no irreversible flocculation had occurred. The surface

crystalline phase was observed for several values of  $a_S/a_L$  (see Tbl. 5.1) and in cells made from different materials, including glass, quartz, and polystyrene. The surface crystalline phase was observed on both flat and round cells walls; the radius of curvature of the wall was large compared to the size of the individual crystallites. The surface phase is robust.

The system we use consists of electrically charged polystyrene spheres, which are highly screened by small ions in solution. Because of the high degree of screening, we expect the interaction between spheres to be well approximated by a hard-sphere potential. A common approach for ascertaining how closely the interparticle potential approximates a hard-sphere potential is to find the volume fraction at which a monodisperse suspension of particles crystallize [2]. By comparing this to 0.49, the known volume fraction for the hard-sphere freezing transition, the effective hard-sphere size of the spheres can be determined. A sensitive measurement of this volume fraction is obtained from 0.205  $\mu\text{m}$  particles, in which crystallization is observed at  $\phi = 0.44$ . This result indicates that the effective radius of the particles is less than 4 nm larger than the physical radius [20].

We have observed phase separation in an essentially hard-sphere system. In addition to bulk phase separation, we find a striking, new ordered phase located on the cell walls (Fig. 5.2), which is observed at volume fractions as low as 0.2, substantially less than the value of 0.49 for the hard-sphere freezing transition in monodisperse suspensions. These phase transitions can be understood as entropically-driven transitions which arise from a small-sphere mediated *entropic* attractive interaction between large spheres. Several questions about the surface phase remain unaddressed. These include its structure and composition, details of the growth kinetics, and the equilibrium two dimensional, fluid like surface phase, which probably exists below the phase separation line in Fig. 5.3.

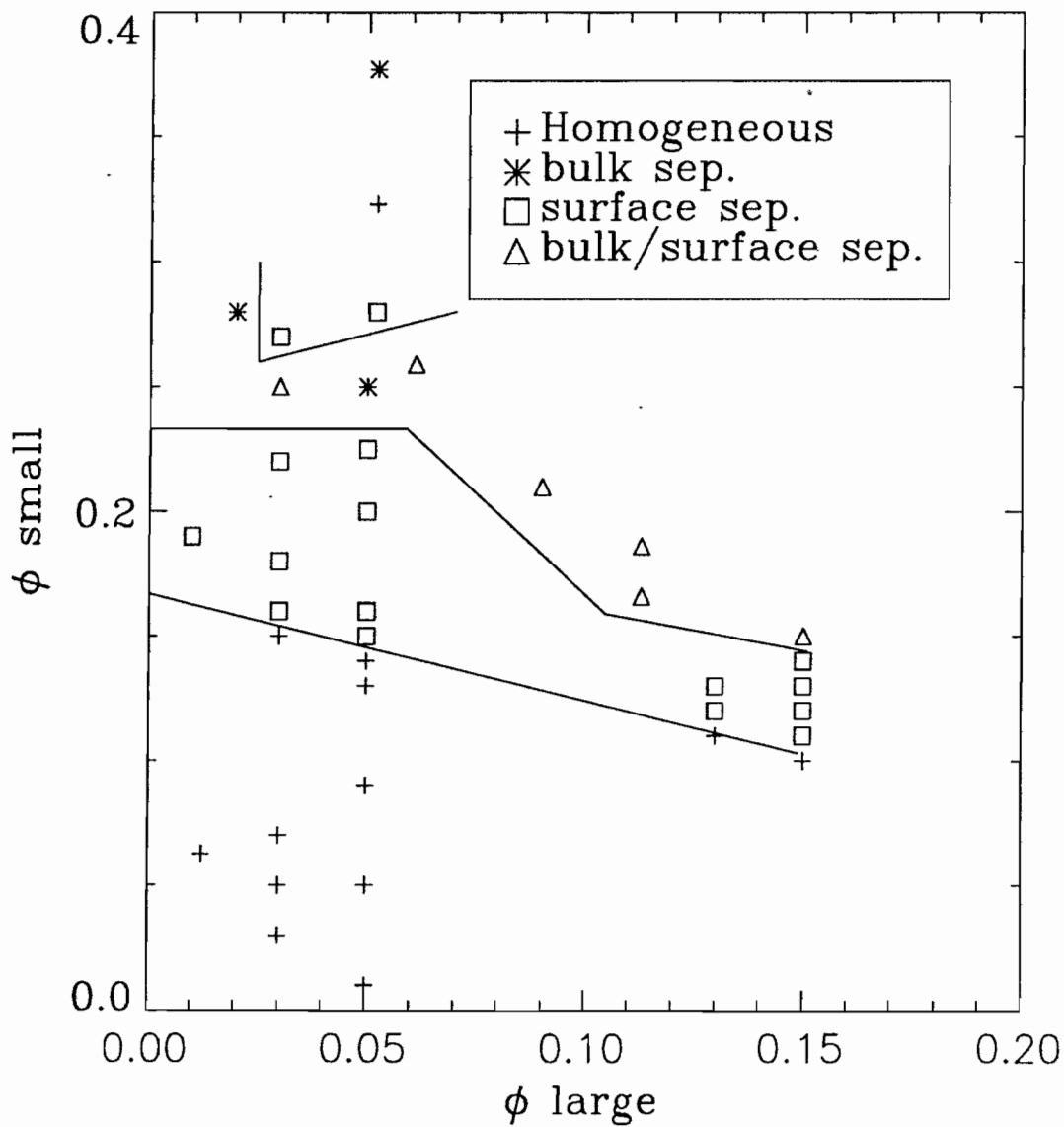


Figure 5.3: Phase diagram of 460/65 nm system. The dynamics of separation were very slow in the upper region, suggesting the existence of a glassy state.

## 5.2 Calculation of Excluded Volume

Although straightforward, a typing error in the originally published calculation [13] of the change in excluded volume due to large spheres approaching each other necessitates a careful presentation of the correct result.

The change in excluded volume influences the thermodynamics of a binary system through its free energy. We first review how a change in volume affects the free energy. The ideal gas is an entirely entropic system. The free energy per particle is

$$F = -kT \ln(V/\lambda^3), \quad (5.1)$$

where  $\lambda$  is the de Broglie wavelength. After a small change in volume  $\delta V$ , the free energy is

$$F + \delta F = E - TS = -kT \ln[(V + \delta V)/\lambda^3]. \quad (5.2)$$

The change in free energy to first order in  $\delta V/V$  is

$$\delta F = kT \frac{\delta V}{V}. \quad (5.3)$$

For a gas of small particles, the change in free energy is multiplied by the number of small balls  $N_S$ . In terms of the volume fraction occupied by the small balls  $\phi$  and the small ball diameter  $a_S$ , the change in free energy is

$$\delta F = \frac{kT\phi}{\pi a_S^3/6} \delta V. \quad (5.4)$$

In Fig. 5.1, we saw that when the surface of two large spheres are separated by less than a small sphere diameter, there is a change in the free volume available to the small spheres. This new volume is equal to the overlap volume between two spheres of diameter  $a_L + a_S$  centered on the large balls. This volume is straightforward to calculate. We need to calculate twice the shaded volume in Fig. 5.4. This volume can be found in any mathematical handbook [21]; it is:

$$V_{>} = \frac{\pi}{3} h^2 (3R - h). \quad (5.5)$$

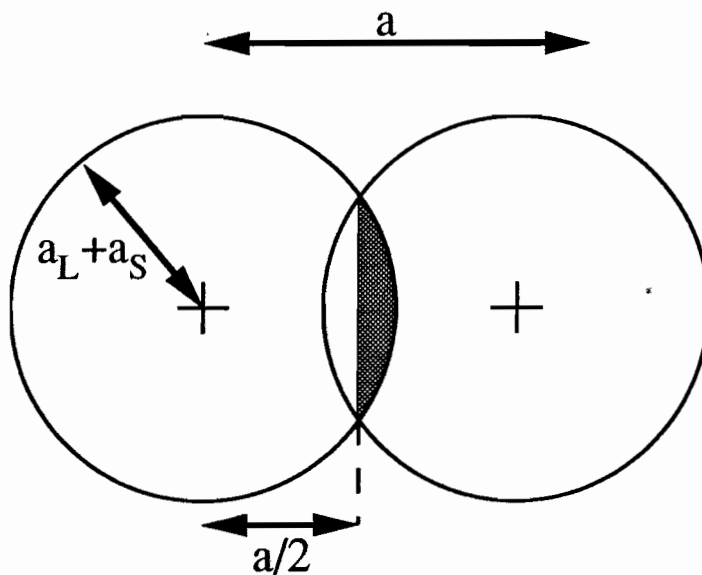


Figure 5.4: The volume of overlap between two spheres is twice the shaded volume in this figure.

With  $h = a/2$  and  $R = a_L + a_S$ , the total volume of overlap is

$$vV_{overlap} = 2V_{>} = (\pi/6)(a_L + a_S - a)^2 (a_L + a_S + a/2). \quad (5.6)$$

For a large sphere a distance  $a$  from a wall, the argument is the same. The large (presumably infinite) radius of curvature of the wall, however, results in a larger total overlapping volume

$$V_{overlap} = (\pi/3)(a_L + a_S/2 - a)^2 (a_L/2 + a_S + a). \quad (5.7)$$

To compare these overlapping volumes, we plot the free energy for small particles as a function of the separation between either two large balls or a large ball and a wall in Fig. 5.5. Clearly, the potential at the wall is deeper. To carefully compare these potentials, we plot them together, shifting the ball-ball curve so that the minima of the two potentials overlap (Fig. 5.6). In addition to shifting the curves, the ball-ball potential has been multiplied by a factor of two. The close, although imperfect, overlap of these lines indicates that the ball-wall potential is almost twice as deep as the ball-ball potential, and it is thus four times as strong per large particle! This

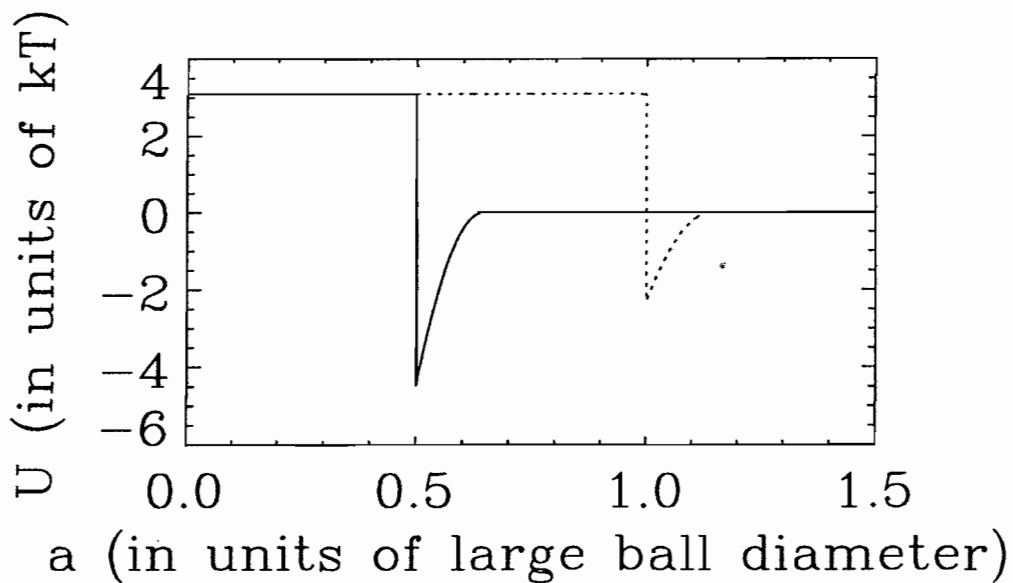


Figure 5.5: Entropic potential between (solid) a large sphere and the wall and (dotted) two large spheres. This calculation is for  $a_L/a_S = 7$  and  $\phi_S = .15$ .

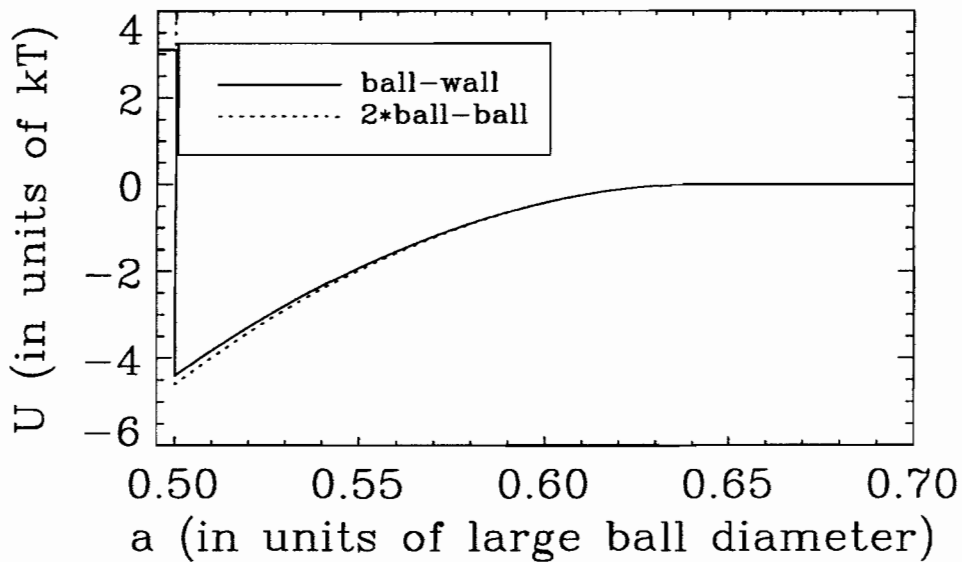


Figure 5.6: Comparison of ball-ball and ball-wall potentials. In this plot, the ball-ball potential is shifted and multiplied by 2 in order to demonstrate that the ball-wall potential is twice as deep as the ball-ball potential.

factor of two is not exact and is thus not formally apparent in the ratio of Eqs. (5.6) and (5.7). This potential is due entirely to the *entropy* of the small particles.

### 5.3 Coulomb Repulsion and van der Waals Attraction

There are many valid criticisms of theories of interaction between colloidal particles. These potentials are typically very difficult to calibrate and rely on poorly known materials properties. Statistical mechanical calculations on colloidal systems generally assume that the potentials will be pair-wise additive, which is not true for non-nearest neighbor Coulombic forces in a dense colloid. Nevertheless, these potentials are used in colloidal science. In this section, we will discuss the theoretical interaction potential between colloidal particles as carefully as we are able. Although we treat these potentials with skepticism, they have a number of qualitative features which can be a helpful guide to our thinking about colloids.

The polystyrene suspensions used in this study interact both through screened Coulomb and van der Waals forces. The screened Coulomb forces are generally described by the Debye-Hückle potential or the DLVO (Derjaguin-Landau-Vreeker-Overbeek) potential which uses the same basic physics but employs a more sophisticated treatment of the geometric boundary conditions. We begin by briefly commenting on Coulomb based interactions and then discuss van der Waals interactions.

The logical path through this problem begins with the Poisson equation, adds a statistical distribution of counter ions (the Boltzman distribution), then includes the finite size of the particle. Following the development of Ref. [22], we begin with the Poisson equation for the potential  $\phi$  of a charged particle in a solvent with counter ions:

$$\nabla^2\phi = \rho(r) \tag{5.8}$$

$$-\frac{\epsilon}{4\pi} \left[ \frac{1}{r^2} \frac{d}{dr} \left( r^2 \frac{d\phi}{dr} \right) \right] = \rho(r), \quad (5.9)$$

where the second line is for a spherical particle in spherical coordinates,  $r$  is measured from the particle's center, and the  $\rho$  is the charge density. Maxwell's equations do not tell us the charge density of counter ions in the fluid surrounding the particle. To comment on this, we use statistical mechanics, in this case the simplest possible use of statistical mechanics. That is, we calculate the expectation value of the charge density  $\rho(r)$  by using the Boltzman factor  $\rho(r) = n(r)ze \exp(-ez\phi(r))$ . The first term in the power series expansion of the Boltzman factor gives the total charge, which is already known. The second term gives the Debye-Hückle or *linearized* Poisson-Boltzman equation

$$\rho(r) = - \sum_i \frac{n_i z_i^2 e^2 \phi(r)}{kT}, \quad (5.10)$$

where the sum is over the species of counter ions in solution with ion number density  $n_i$  and valence  $z_i$ . The unit charge is  $e$ . Combining Eqs. (5.9) and (5.10) we arrive at the linearized Poisson-Boltzman equation

$$\frac{1}{r^2} \frac{d}{dr} \left( r^2 \frac{d\phi}{dr} \right) = \left( \frac{4\pi e^2}{\epsilon kT} \sum_i n_i z_i^2 \right) \phi(r). \quad (5.11)$$

The quantity in parenthesis on the right side of this expression has units of inverse length squared and is written  $\kappa^2$ , where  $1/\kappa$  is called the *screening length*. Solutions to the linearized Poisson-Boltzman Equation are of the form  $Ae^{-\kappa r}/r$ , where  $A$  is obtained from the boundary conditions. For a point charge with valence  $z$ , the screened potential is

$$\phi(r) = \frac{ze\kappa}{\epsilon} \frac{e^{-\kappa r}}{\kappa r}, \quad (5.12)$$

while for a charge of finite radius  $a$  the result is

$$\phi(r) = \frac{ze\kappa}{\epsilon} \frac{e^{\kappa a}}{1 + \kappa a} \frac{e^{-\kappa r}}{\kappa r}, \quad (5.13)$$

which is essentially the DLVO result.

This result is only for the electric potential, *i.e.* the energy needed to bring a unit charge to some distance  $r$  from the center of a polyball. If we accept the DLVO results, we find the *interaction energy*  $U$  between two particles of valence  $z$  and radius  $a$  [23]

$$U(r) = \frac{z^2 e^2 e^{-\kappa(r-2a)}}{\epsilon r + 2a}, \quad (5.14)$$

which can be written for two different sized spheres (with an unjustified and surely incorrect leap of faith about the derivation)

$$U(r) = \frac{z_L z_S e^2 e^{-\kappa(r-a_L-a_S)}}{\epsilon r + a_L + a_S}. \quad (5.15)$$

What we want to know is the value of  $r$  where  $U$  is equal to  $kT$ . Defining the separation between surfaces  $\delta = r - 2a$  for same-sized particles or  $\delta = r - a_L - a_S$  for different sized particles, we find

$$\kappa\delta = -\ln\left(4a \frac{kT\epsilon}{z_L z_S e^2}\right). \quad (5.16)$$

This result gives the interaction length in units of the screening length, a number that is *independent* of the screening length. As a calculational aid, note that  $e^2/kT\epsilon$  is the Bjerrum length of 7 Å in water at 300 °K. Experimental results for  $z$  for half micron diameter particles are in the range of 200-600 [24]. Evaluating (5.16) for 460 nm diameter spheres gives

$$\kappa\delta = 2\ln(z) - 7.18, \quad (5.17)$$

so that the final range of  $\kappa\delta$  runs from 3.4 for  $z = 200$  to 5.6 for  $z = 600$ . For 65 nm particles we find

$$\kappa\delta = 2\ln(z) - 5.22. \quad (5.18)$$

The probable range of  $z$  for the small spheres is between 5 and 20. Any charge less than 14 will produce a negative value for  $\kappa\delta$ . This theory predicts that  $\kappa\delta$  runs from 0 to 2 for the small particles.

After performing these calculations, we see that according to the DLVO potential, the effective diameter of our particles is probably about 5 screening lengths, or 25 nm

larger than their physical diameter. This is incorrect. As noted in Section 5.1, the phase behavior of monodisperse particles indicates that the actual hard-sphere diameter is closer to one than to five screening lengths larger than the particle itself.

The effects of neighboring polyballs and higher order terms in the Boltzman factor may significantly alter the interaction potential. Alexander, Chaikin, *et al.* [25] addressed these issues. They considered a crystal of polyballs and calculated the full (not the linearized) Poisson-Boltzman equation with boundary conditions imposed by a spherical Wigner-Seitz cell. The crucial result from Alexander, Chaikin, *et al.* is the demonstration that the layer of counter ions immediately surrounding a polyball is thinner and contains more ions than the linearized, or Debye-Hückle approach suggests. In particular, they find that within 140 Å of the surface, the counter ion concentration is much higher than Debye-Hückle predicts, meaning that more than 140 Å from the surface, the effective charge is significantly smaller than predicted by Debye-Hückle. The Alexander and Chaikin result suggests that the polyballs are much more like hard-spheres than (5.13) suggests.

## 5.4 Comparison to a Simple Theory

In their work on phase separation in a monodisperse microemulsion with micelles, Bibette, Roux, and Pouligny proposed a simple theory for the boundary in the phase diagram between a bulk solid and a bulk fluid phase [9]. Their calculation is based entirely on entropic energetics. In this section, we will compare our phase diagram to this simple calculation. A complete explanation of the phase boundary they find would require carefully repeating a large segment of their paper here. As we are referring and not adding to their work in this section, we will instead note the content of their results and briefly discuss some of the physical content of their results.

In order to calculate this phase boundary, a statistical criterion is needed to decide

whether the entropic attraction is strong enough to stabilize the crystalline phase against fluctuations. The entropic interaction between large spheres is attractive, thus, a solid is always energetically favored. Bibette, *et al.* use the Lindemann criterion for melting, which states that crystals melt if position fluctuations are larger than 10% of a lattice constant. The phase diagram is calculated by balancing the difference in the chemical potential of the solid and liquid phase against the entropy of the fluid and van der Waals attractions between particles in the crystal.

By imposing the conditions of equal pressure and equal free energy on the liquid and gas phases at the boundary in the phase diagram, Bibette, *et al.* find that the boundary is described by

$$\phi_s = \frac{a_S}{9a_L} \left( -\ln \phi_L + (\mu_S^0 - \mu_G^0) - 6w \right), \quad (5.19)$$

where  $\mu_S^0$  and  $\mu_G^0$  are the chemical potentials of the solid and gas phases, and  $w$  is the van der Waals contribution to the lattice free energy. This boundary represents a balance between the greater entropy of the fluid phase (the term logarithmic in  $\phi_L$ ) and the change in chemical potential and van der Waals energies between the two phases. The crucial features of the expression are the weak dependence on  $\phi_L$  and the linear dependence on the ratio of particle diameters. As discussed in Section 5.3, the van der Waals energy  $w$  is not well known. Bibette, *et al.* treat  $w$  as a free parameter of order 1.

After carefully following the development of the phase boundary Eq. (5.19) in Ref. [9], we have found a numerical error in the evaluation of  $\mu_S^0 - \mu_G^0$  (we find +7 *vs.*  $-5kT$ ), which results in a significant shift in the final phase diagram. We treat the entire expression  $(\mu_S^0 - \mu_G^0) - 6w$  as a free parameter  $C$  in order to compare our results to this simple theory (Fig. 5.7). The results agree in the sense that in both theory and experiment, the phase diagram depends only weakly on  $\phi_L$ . The value of the constant  $C$ , however, disagrees with Bibette, *et al.* who found a value of one in the emulsion/micelle system [9]. A value closer to nine describes our polystyrene/water system. Although at face value, this disagreement seems minor, recall that the

correct value of the difference in chemical potentials is negative. Thus, the van der Waals coefficient  $w$  must also be negative for this theory to be correct. Although the value of the van der Waals coefficient for polystyrene is uncertain, its sign is certainly positive. We conclude that the sensibility of this theory as presented is somewhat suspect and requires further investigation.

## 5.5 DWS Tests of Phase Separated Suspensions

How are the particle dynamics different in the separated phases? We addressed this question by doing DWS in a backscattering geometry (Fig. 3.8) on a few phase separated samples. We found no difference between the dense and the dilute fluid layers in the fluid/fluid samples. The fluid/crystal samples, however, dramatically demonstrated the constrained dynamics of the crystal phase. In Fig. 5.8, we see the difference between two correlation functions, one taken from the fluid and one taken from some crystals grown on the cell wall. The fact that the correlation function does not decay for light scattered from the crystals indicates that the particles in the crystal undergo constrained motion [17]. The incomplete decay is due to the fact that for constrained motion, there is a maximum value for  $\langle \Delta r^2(\tau) \rangle$ , and the autocorrelation function decays exponentially with  $\langle \Delta r^2(\tau) \rangle$ .

## 5.6 Preliminary Investigation of Surface Structure

The entropic crystal growth mechanism described in Fig. 5.1 suggests that the crystals should be close packed large spheres. A little reflection about a close packed array of large balls suggests two basic questions: How large are the spaces between spheres? and Can a small particle fit into this space? For a two-dimensional crystal, planar geometry can be used to figure out how large the space is. The answer in

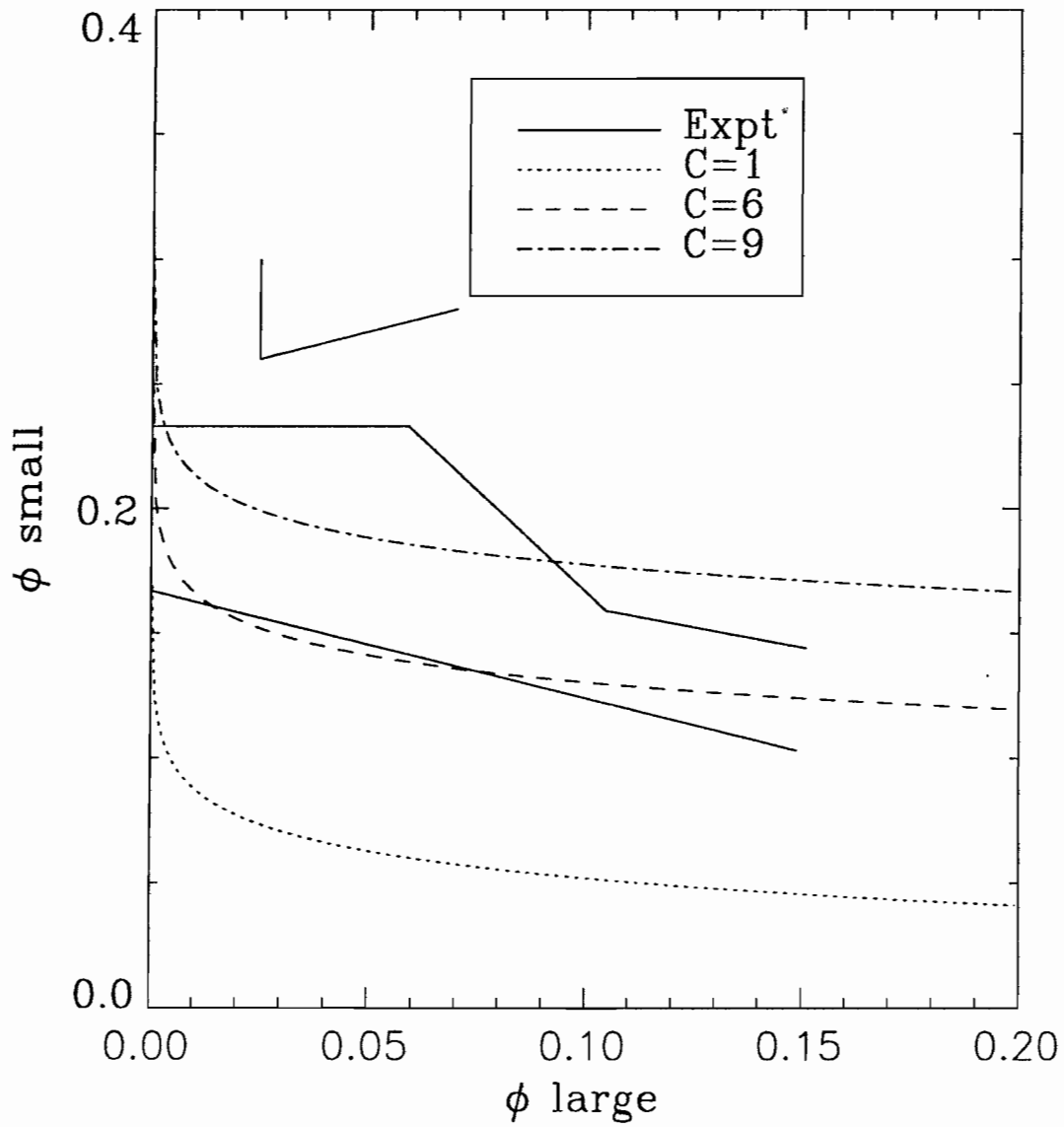


Figure 5.7: Comparison of experimental and theoretical phase diagram. The empirical phase boundaries from Fig. 5.3 are plotted along with the simple theory of Bibette, *et al.* [9] with different values of the adjustable constant from their theory.

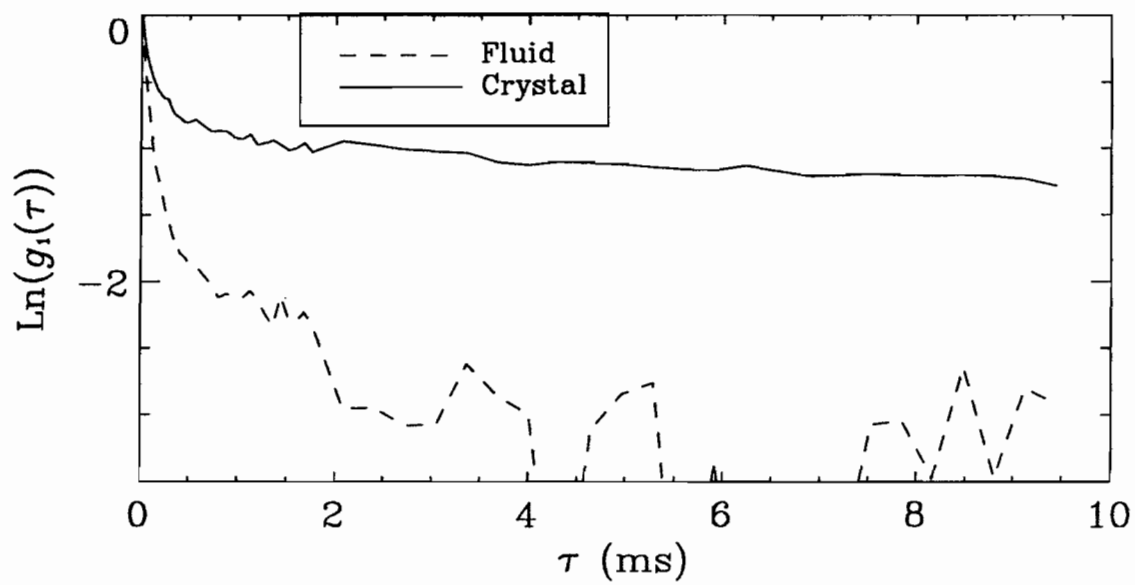


Figure 5.8: The DWS autocorrelation function is plotted for light scattered from a surface crystallite and from the bulk fluid region. The failure of the correlation function to decay is a signature of a crystalline phase [17].

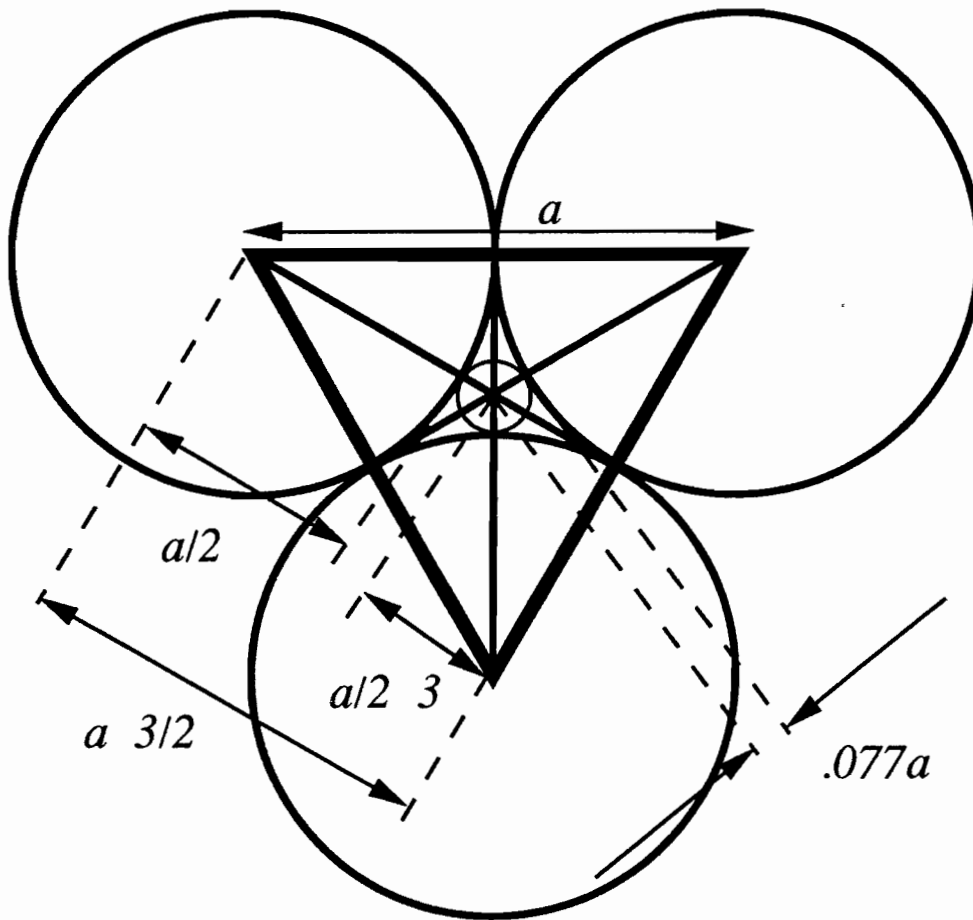


Figure 5.9: Two-dimensional geometry of interstitial spheres. If  $a_L/a_S$  is greater than  $1/(2 \cdot 0.077) = 6.4$ , then small spheres can fit into a two dimensional lattice of large spheres without modifying the large sphere lattice.

two dimensions is that for particle ratios  $a_L/a_S$  greater than 6.4 (Fig 5.9, a small particle will fit between large balls. In three dimensions, the space is significantly larger and more difficult to calculate (the minimum  $a_L/a_S$  in three dimensions is 2.3. ( Fig. 5.10)). An unoccupied interstitial volume will have a large cost in free energy, which suggests that the crystal structure may not be a simple close packed arrangement of large particles.

A few preliminary steps have been taken in our laboratory to learn about the structure of the binary systems. An attempt at light scattering from crystallites showed possible signatures of Kossel lines, but no conclusive evidence for Kossel

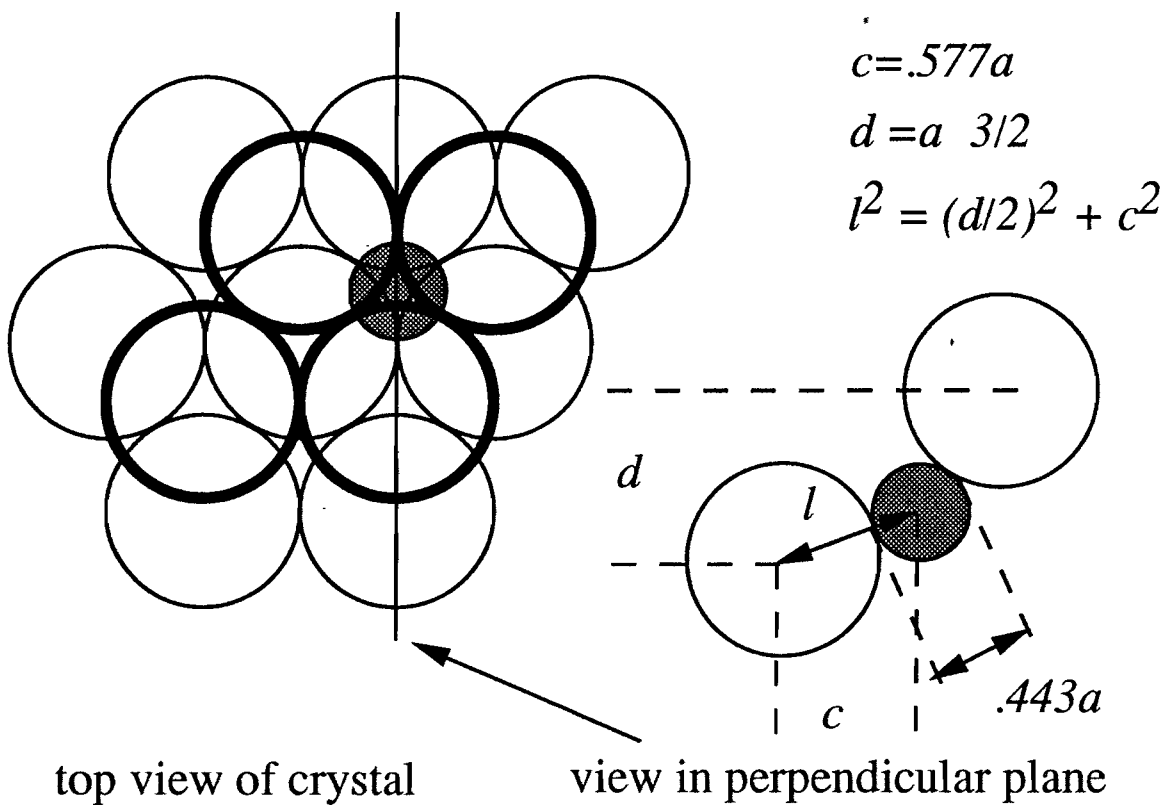


Figure 5.10: Three dimensional geometry of interstitial spheres. In a close packed lattice, the second plane of spheres could occupy either the so-called B or C sites. The unoccupied sites have a large space which interstitial particles can insert themselves into. We calculate the maximum size of interstitial spheres by examining the indicated plane perpendicular to the surface of the cell and using the results from Fig. 5.9.

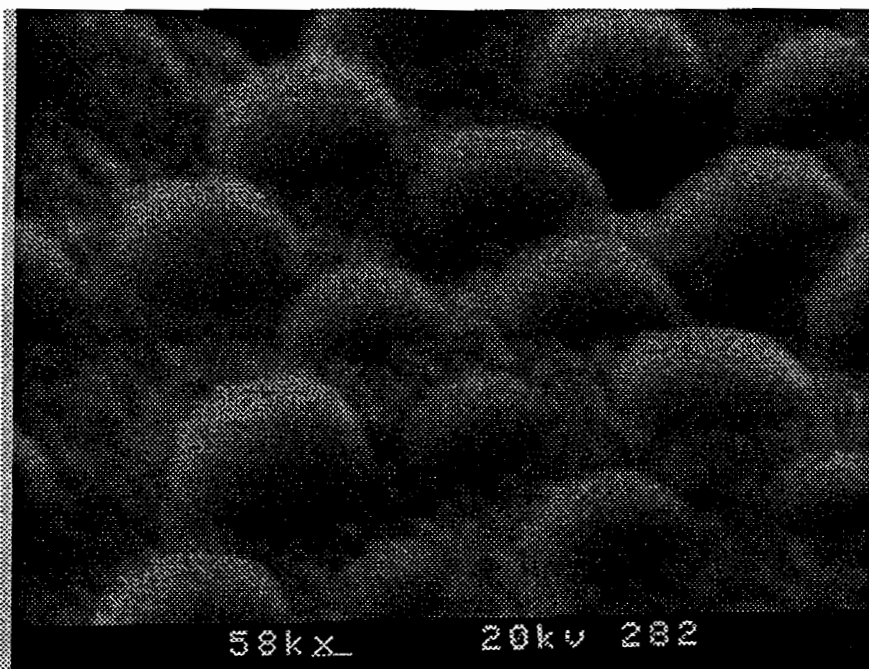


Figure 5.11: SEM image of binary crystal. The roughness between large particles is actually small particles.

lines has been attained. A more interesting approach was an attempt to view the crystallites under an electron microscope. With the assistance of Harry Deckman at Exxon, crystals were scraped from the wall of the cell, placed on a silicon wafer, plasma coated with 50 Å of gold, and then examined in a scanning electron microscope (SEM). Each step in sample preparation may have changed the crystal structure. Scraping the crystals from the cell wall will perturb them strongly. Plasma coating involves drying under vacuum. The drying process will result in balls from the bulk fluid being deposited on the crystal, and it will also cause balls to contact each other, and thus cause irreversible flocculation due to van der Waals forces. It is, therefore, difficult to interpret the SEM images. In these images, the small 65 nm diameter balls were at the resolution limit of the SEM. They can be seen, however, and it appears that the small balls do occupy interstitial positions and that the orientation of the large and small balls crystal axes coincide.

# Bibliography

- [1] J. P. Hansen and I. R. McDonald, *Theory of Simple Liquids*, 2nd ed. (Academic Press, London, 1991).
- [2] P. N. Pusey and W. van Meegen, *Phase Behaviour of Concentrated Suspensions of Nearly Hard Colloidal Spheres*, *Nature* **320**, 340 (1986).
- [3] J. L. Lebowitz, *Exact Solution of Generalized Percus-Yevick Equation for a Mixture of Hard Spheres*, *Phys. Rev.* **133**, A895 (1964).
- [4] J. S. van Duijneveldt, A. W. Heinen, and H. N. W. Lekkerkerker, *Phase separation in bimodal dispersions of sterically stabilized silica particles*, *Europhys. Lett.* **21**, 369 (1993).
- [5] S. Sanyal, N. Easwar, S. Ramaswamy, and A. K. Sood, *Phase separation in binary nearly-hard-sphere colloids: evidence for the depletion force*, *EuroPhys. Lett.* **18**, 107 (1992).
- [6] A. P. Gast, W. B. Russel, and C. K. Hall, *An Experimental and Theoretical Study of Phase Transitions in the Polystyrene Latex and Hydroxyethylcellulose System*, *J. Coll. Int. Sci.* **109**, 161 (1986).
- [7] A. P. Gast, C. K. Hall, and W. B. Russel, *Polymer-induced phase separations in nonaqueous colloidal suspensions*, *J. Coll. Int. Sci.* **96**, 251 (1983).
- [8] J. Bibette, D. Roux, and F. Nallet, *Depletion Interactions and Fluid-Solid Equilibrium in Emulsions*, *Phys. Rev. Lett.* **65**, 2470 (1990).

- [9] J. Bibette, D. Roux, and B. Pouligny, *Creaming of emulsions: the role of depletion forces induced by surfactant*, J. Phys. II France **2**, 401 (1992).
- [10] T. Biben and J. P. Hansen, *Phase Separation of Asymmetric Binary Hard-Sphere Fluids*, Phys. Rev. Lett. **66**, 2215 (1991).
- [11] D. Frenkel and A. A. Louis, *Phase separation in binary hard-core mixtures: An exact result*, Phys. Rev. Lett. **68**, 3363 (1992).
- [12] P. Bartlett and R. H. Ottewill, *Geometric Interactions in binary colloidal dispersions*, Langmuir **8**, 1919 (1992).
- [13] S. Asakura and Oosawa, *Interaction between particles suspended in solutions of macromolecules*, J. Polymer Sci. **32**, 183 (1958).
- [14] Note that  $\Delta V$  was incorrectly typed in Eq. (2) of ref. [13]. The overlapping volume between two spheres of radius  $(a_L + a_S)/2$  separated by  $a_L < a < (a_L + a_S)$  is  $(\pi/6)(a_L + a_S - a)^2 (a_L + a_S + a/2)$ , and between a sphere of radius  $R$  whose center is  $a_L/2 < a < a_L/2 + a_S$  away from a wall the overlapping volume is  $(\pi/3)(a_L + a_S/2 - a)^2 (a_L/2 + a_S + a)$ . This argument sets no lower limit on the size of small particles.
- [15] S. Fraden and G. Maret, *Multiple Light Scattering from Concentrated Interacting Suspensions*, Phys. Rev. Lett. **65**, 512 (1990).
- [16] D. J. Pine, D. A. Weitz, J. X. Zhu, and E. Herbolzheimer, *Diffusing-Wave Spectroscopy: Dynamic Light Scattering in the Multiple Scattering Limit*, J. Phys. France **51**, 2101 (1990).
- [17] A. Meller and J. Stavans, *Glass transition and phase diagrams of strongly interacting binary colloidal mixtures*, Phys. Rev. Lett. **68**, 3646 (1992).
- [18] The scattering cross section for green light is 2500 times larger for a single 460 nm polystyrene sphere than a 65 nm one. At equal volume fractions, the

larger number of small particles reduces this imbalance but the total cross section is still 7 times larger for the 460 nm particles.

- [19] D. J. Courtemanche and F. van Swol, *Wetting State of a Crystal-Fluid System of Hard Spheres*, Phys. Rev. Lett. **69**, 2078 (1993).
- [20] The interparticle potential falls exponentially with distance due to screened coulomb repulsion and algebraically due to van der Waals attraction. Accurate estimates of either potential are difficult to obtain, especially in the highly screened limit. We have observed that increasing the ion concentration from .01M to .02M has a small effect on the location of the homogeneous/surface phase line, while increasing the ion concentration to .05M causes irreversible flocculation in several days. The secondary minimum in the combined potential, however, is generally believed to be much less than  $kT$ , while the entropic attraction between large particles and the cell walls are several  $kT$ .
- [21] M. R. Spiegel, *Schaum's Outline Series Theory and Problems of Mathematical Handbook of Formulas and Tables* (McGraw-Hill, New York, 1968).
- [22] J. O. M. Bockris and A. K. N. Reddy, in *Modern Electrochemistry v.1* (Plenum Press, New York, 1970).
- [23] W. Hess and R. Klein, *Generalized Hydrodynamics of Systems of Brownian Particles*, Adv. Phys. **32**, 173 (1983).
- [24] H. M. Lindsay and P. M. Chaikin, *Elastic Properties of Colloidal Crystals and Glasses*, J. Chem. Phys. **76**, 3774 (1982).
- [25] S. Alexander *et al.*, *Charge Renormalization Osmotic Pressure and Bulk Modulus of Colloidal Crystals: Theory*, J. Chem. Phys. **80**, 5776 (1984).

## Chapter 6

### Diffuse-Transmission

# Spectroscopy, a Static Probe of Structure

The arrangement of particles in a colloidal suspension is closely related to bulk physical properties, including colloidal stability and rheology. Colloid structure is also closely connected to microscopic properties such as the interparticle interaction potential. Structural correlations are most easily probed by light scattering in single scattering samples such as dilute suspensions or suspensions of particles whose index of refraction nearly matches that of the solvent. Colloid structure can also be probed using a synchrotron by small angle X-ray scattering or by small angle neutron scattering in systems where isotopic substitution is practical. Many useful and interesting colloids, however, are neither dilute index matched, nor easily amenable to isotopic substitution. Such colloids are often highly multiply scattering, appearing white like milk or white paint.

In this chapter we introduce a new technique, diffuse-transmission spectroscopy (DTS), that *employs* multiple scattering to probe colloid structure. We present DTS measurements from concentrated suspensions of polystyrene spheres in water.

DTS uses a tungsten lamp and monochromator to obtain a transmission spectrum from which structural information can be deduced. We demonstrate that diffuse transmission data are useful for particle sizing, determination of volume fraction, and monitoring of interparticle potentials. The DTS data set is not adjustable; it allows direct comparison with structural models.

The cornerstone of our approach is the photon diffusion approximation, which describes photon transport in highly multiple scattering media. In the diffusion approximation, photon transport is governed by a single parameter, the photon transport mean free path  $l^*$ . We will review the connection between interparticle structure and  $l^*$ , focusing on how that connection can be exploited to probe structure.

Fluid structure can be described by the particle pair correlation function or by its Fourier transform, the structure function. We will restrict our attention to Fourier space, which is a more natural choice for scattering experiments. The structure factor is related to real space particle positions  $\mathbf{r}_i$ , according to

$$S(\mathbf{q}) = (1/N) \langle \sum_{i,j} e^{i\mathbf{q}\cdot(\mathbf{r}_i - \mathbf{r}_j)} \rangle - N\delta(\mathbf{q}), \quad (6.1)$$

where  $N$  is the number of particles, and the delta function  $\delta(\mathbf{q})$  removes the peak at zero wave vector. For a fluid, the structure factor is isotropic, meaning that the structure factor depends on the amplitude, not the direction of the scattering wave vector, *i.e.*,  $S(\mathbf{q}) = S(q)$ .

The Percus-Yevick approximation is the standard analytic approach to calculations of the structure of monodisperse hard-spheres [1]. In Fig. 6.1, we see the Percus-Yevick structure factor for three volume fractions  $\phi = 0.05$ ,  $\phi = 0.30$ , and  $\phi = 0.40$  plotted versus the dimensionless scattering wave vector  $y = qa$ , where  $a$  is the particle diameter. This plot covers the range of  $y$  relevant to our systems, which are nearly hard-sphere suspensions of micron sized charged polystyrene spheres in water with sufficient ionic content (0.01 molar) to screen the Coulomb interactions over roughly 4 nm.

We will now discuss single and multiple scattering, showing that there can be wave

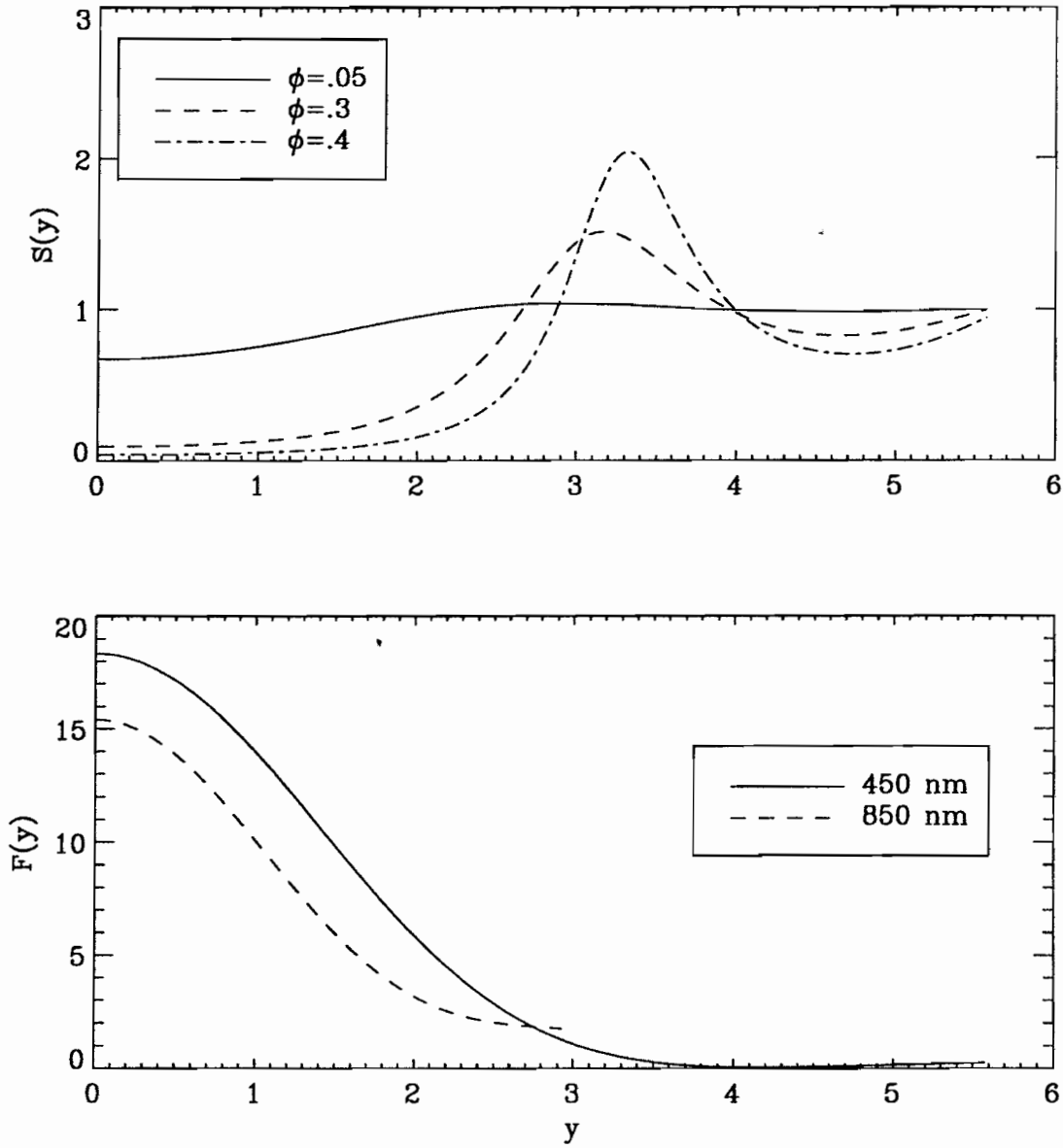


Figure 6.1: Plot of  $S(y)$  from Percus Yevick theory for various volume fractions. Below is the form factor at a wavelength of 450 nm and 50 times the form factor at 850 nm. Note that the form factor for scattering through angles between zero and  $\pi$  covers a different range of scattering wave vectors at each wavelength because the largest dimensionless scattering wave vector is  $4\pi a/\lambda$ . Thus, the change in diffuse transmission between 450 and 850 nm depends on the value of the structure factor between the dimensionless  $y$  values of 3 and 5.6. This dependence is exploited by diffuse transmission spectroscopy.

vector dependent measurements made by multiple scattering. In single scattering experiments, wave vector resolution is obtained by selecting a scattering angle. In multiple scattering experiments, photons scatter many times through different wave vectors, making the wave vector resolution that we obtain more elusive.

The scattering wave vector  $\mathbf{q}$  is simply the difference between the input and output wave vectors  $\mathbf{k}_0$  and  $\mathbf{k}_f$ . For elastic single scattering,

$$|\mathbf{q}| = |\mathbf{k}_f - \mathbf{k}_0| = 2k_0 \sin(\theta/2), \quad (6.2)$$

where  $\theta$  is the angle between  $\mathbf{k}_0$  and  $\mathbf{k}_f$ , and  $k = 2\pi/\lambda$  for photons with wavelength  $\lambda$  in the scattering medium. We see that  $q$  ranges from zero to  $2k_0$ .

The intensity function for scattering through a wave vector  $q$  is

$$I(q) = F(q, k_0 a) S(q), \quad (6.3)$$

where the form factor  $F(q, k_0 a)$  describes scattering from an isolated particle. The form factor depends on the contrast in index of refraction between particle and solvent, the ratio of the particle diameter to the photon wavelength  $k_0 a$ , and the scattering wave vector  $q$ . The dependence of  $F$  on  $k_0 a$  is usually not made explicit; however, this dependence is central to the technique of diffuse-transmission spectroscopy. For scattering problems with  $k_0 a$  of order unity, the form factor must be computed using Mie theory [2]. In Fig. 6.1b, we exhibit the form factor as a function of dimensionless wavevector  $y$  at two different wavelengths. At shorter wavelengths, a higher range  $q$  in the structure factor is probed by diffuse transmission.

Multiple scattering is generally considered a problem to avoid; however, we restrict our attention to highly multiple scattering systems and *exploit* it. There has been significant recent attention to the use of the photon diffusion approximation to describe photon transport in media as diverse as clouds [3], biological tissue [4, 5], foams [6], paper-size [7], and dairy products [8]. In the diffusion approximation, it is assumed that each photon scatters many times and that its transport can be modeled as a random walk. The average distance between scattering events  $l$  is  $l = 1/\rho\sigma_{sc}$ ,

where  $\rho$  is the number density of scattering particles, and  $\sigma_{sc}$  is the scattering cross section per particle for scattering from correlated groups of particles

$$\sigma_{sc} = \frac{1}{k_0^2} \int_0^{2k_0a} F(y, k_0a) S(y) y dy. \quad (6.4)$$

This form for the scattering cross section is obtained from an integral over scattering angles by change of variables. The form factor is generally peaked at small angles (small- $q$ ); thus, the direction of propagation of the photon is not randomized after each scattering event. There is a longer length, the photon random walk step-length, or the photon transport mean free path  $l^*$  which is related to the average distance between scattering events  $l$  by the average scattering angle [2, 9, 10]

$$\frac{l^*}{l} = \frac{1}{1 - \langle \cos(\theta) \rangle}. \quad (6.5)$$

Combining Eqs. (6.5) and (6.4), we arrive at an expression for the random walk step-length

$$\frac{1}{l^*} = \frac{\pi \rho}{(k_0a)^4 k_0^2} \int_0^{2k_0a} y^2 F(y, k_0a) S(y) y dy. \quad (6.6)$$

The photon transport mean free path or the random walk step-length is calculated by integrating over the *product* of the form factor, which is well known for spherical particles, and the structure factor, which we wish to study.

Using measurements of  $l^*$  to deduce  $S(y)$  ultimately requires a strategy for inverting Eq. (6.6). The first insight into the dependence of  $l^*$  on the structure factor is that the upper cutoff of the integral in (6.6) depends on the ratio of the particle diameter to the photon wavelength. Thus, for a fixed particle size, the value of  $l^*$  at wavelengths with wave vector  $k_1$  and  $k_2$  depends in part on the structure factor between the dimensionless wave vectors  $2k_1a$  and  $2k_2a$ . This point is illustrated in Fig. 6.1 where we see that the value of  $l^*$  calculated at the larger wave vector depends on an integral over a larger range of the structure factor.

Some groups measure material properties of colloidal particles by single scattering measurements of the total cross section (scattering plus absorption) [11–13]. In

diffuse transmission spectroscopy, we are making a conceptually similar measurement of the transport cross section ( $l^* = 1/\rho\sigma_{tr}$ ). In the limit where  $S(y) = 1$ , the scattering cross section is the first moment of the intensity function  $F(y)S(y)$  (see (6.6)). The transport cross section we are measuring is simply the third moment of the intensity function (*i.e.*,  $\int_0^{2k_0a} F(y)S(y)y^3dy$ ).

## 6.1 Experiment

Our experimental goal is to determine  $l^*$  as a function of wavelength. There are a number of approaches to measuring  $l^*$  in a highly multiply scattering material. The simplest approach, discussed below, is to measure the transmission coefficient of a slab of colloid. More complicated techniques include the measurement of the angular width of the coherent backscattering cone [14–18] or measuring the time dependence of a pulse of light stretched during transmission through the colloid.

The transmission coefficient of a slab of colloid is the simplest quantity to measure since it requires neither pulsed lasers, collimated light sources, nor detectors with fine temporal or spatial resolution. The transmission coefficient is also fairly simple to interpret. For a slab of colloid with thickness  $L$  and transport mean-free path  $l^*$ , the transmission coefficient is

$$T = \left(\frac{l^*}{L}\right) \frac{\frac{2}{3} \left(\frac{1+R}{1-R}\right) + \alpha}{1 + \frac{4}{3} \left(\frac{1+R}{1-R}\right) \frac{l^*}{L}}, \quad (6.7)$$

where  $\alpha$  is a parameter of the diffuse model of photon transport which is roughly one [2, 9, 19], and  $R$  is the diffuse reflection coefficient. This result is obtained by solving the one dimensional diffusion equation which describes photon transport through a slab of infinite transverse extent and comparing the transmitted to the reflected flux. The diffuse reflection coefficient is obtained from an angular average of the Fresnel reflection coefficient [20] and a sum over multiple reflections [19]. The approximately linear dependence of the diffuse transmission coefficient on the photon transport mean free path (6.7) is experimentally ensured by keeping the ratio of  $L$

to  $l^*$  large and minimizing the reflection coefficient by submerging the sample cell in an index matching fluid (water).

Our apparatus for measuring the wavelength dependent transmission coefficient (Fig. 6.2) uses a tungsten lamp, a monochromator, an integrating sphere, and a silicon photodiode. This apparatus could probably be implemented simply by making small changes to a commercial spectrophotometer fitted with an integrating sphere. The integrating sphere allows us to collect light from many output angles and to sample those angles uniformly. The light passing into the monochromator is modulated using a chopper, and a lock-in amplifier is used to measure the current from an unbiased photodiode at the chopper frequency. The system responds linearly over a wide range of transmission coefficients from 1 to at least  $10^{-4}$ . The sample is immersed in water which reduces the diffuse reflection coefficient from roughly 0.10 to 0.02 [19]. The integrating sphere we used consists of Spectralon reflectance material from Lab Sphere (North Sutton, New Hampshire). Spectralon is hydrophobic and can be immersed in water without changing its reflective properties; however, by submerging the entire sphere, we found that the photon path lengths in the sphere were so long that the weak photon absorption of water dominated the spectrum [21]. We therefore, choose to hold the cell horizontally and immerse the sphere's input port in water, retaining the advantages of an index matching bath for our cell.

Accurate absolute measurements of transmission require the measurement of a reference signal. In this experiment, normalization was accomplished by sequentially measuring the transmission through two samples, the one under study and another consisting of the same colloid at a significantly lower volume fraction where the structure factor is relatively less important (compare the solid and dashed lines in Fig. 6.1a). The less dense colloid will have many of the same variations with wavelength, including variations of the form factor, the lamp intensity, and the detector efficiency with wavelength. The reference cell will also have the same angular output

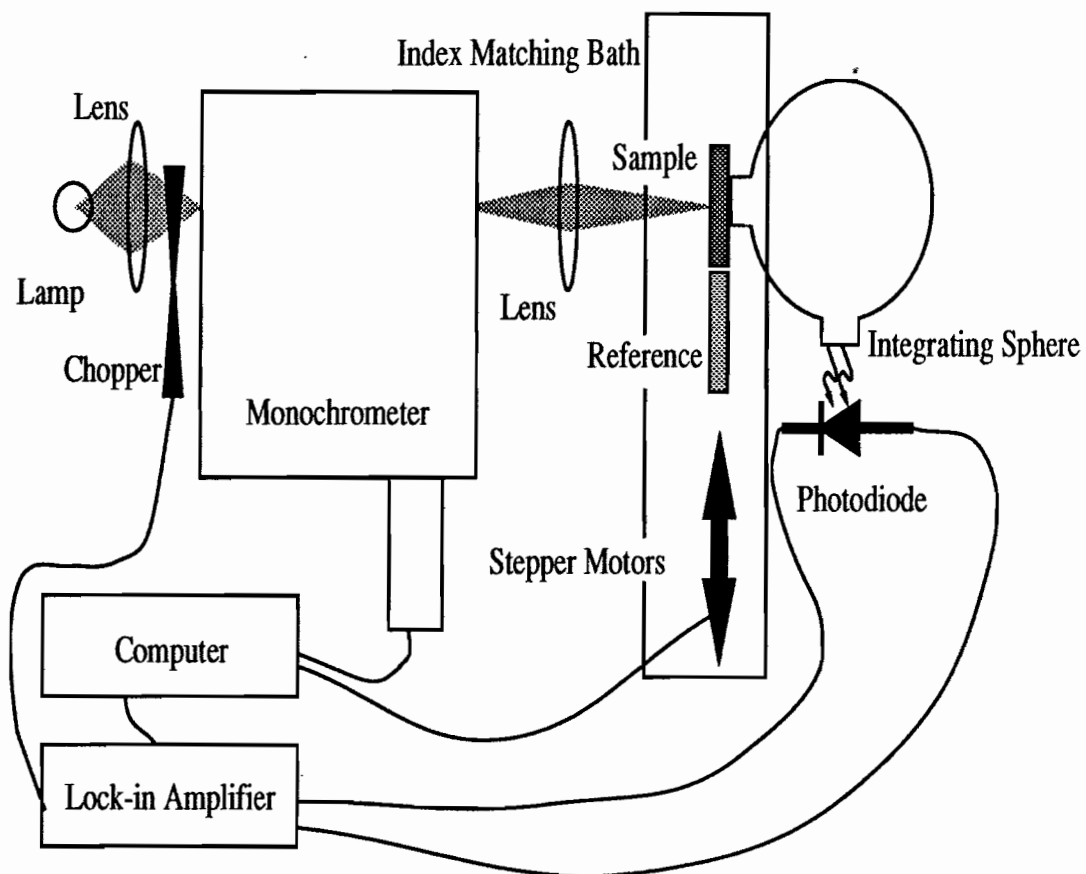


Figure 6.2: Apparatus for diffuse transmission spectroscopy. Computer controlled stepper-motors switch the sample and reference as well as changing the photon wavelength. Detection is accomplished using a lock-in amplifier and chopping the light entering the monochromator. The sample is immersed in water to reduce the diffuse reflection coefficient. Note the similarity of this apparatus to commercially available spectrophotometers fitted with an integrating sphere.

distribution of transmitted light as the sample under study. By using this normalization scheme, we produce a data set with *no adjustable experimental parameters*. If a non-diffuse sample is used for normalization, there will be an adjustable parameter, the angular collection efficiency. In this case, uncertainty in the collection efficiency will obscure the most sensitive feature of the data set, the absolute transmission. The final advantage of using a diffuse light source for normalization is that uncertainty in the numerical values of  $R$  and  $\alpha$  in the numerator of the relation between  $T$  and  $l^*$  (6.7) is normalized out of the data set. In the data presented here, we ensure the applicability of the diffusion approximation by choosing reference samples such that  $L/l^*$  is always greater than 10 [19,22]. The data were obtained between 450 nm and 850 nm. The lower wavelength limit was set by the rapidly varying spectra of our lamp, monochromator, and photodiode; the upper wavelength limit was set by a weak photon absorption band in water.

We will now discuss some of the experimental details of the DTS technique. While these details must be considered, they contribute very little to the final DTS spectrum and do not affect our interpretation of DTS data. A consideration of these issues, however, highlights the importance of the use of a suitable reference sample. Once a photon enters the integrating sphere, the probability that it will strike the detector is independent of the photon's initial direction. Since the input and output ports on the integrating sphere are the same size, the photon is just as likely to re-enter the sample as it is to strike the photodiode. The transmission coefficient is always much less than one, so most of the light that re-enters the sample will be reflected back into the integrating sphere. There is a finite probability, however, that a photon will escape after re-entering the sample. By considering the possibility of a photon escaping after any number of reflections, we find that the measured transmission coefficient  $T_m$  is related to the actual transmission coefficient  $T$  by

$$T_m = \frac{cT/2}{1 - c(1 - T)/2}, \quad (6.8)$$

where  $c$  is the collection efficiency of the integrating sphere. The collection efficiency

is essentially the solid angle subtended by the sphere's input aperture divided by  $2\pi$ . A conservative estimate of  $c$  in the present apparatus is between 0.75 and 0.80.

The quantity measured in DTS is the ratio of transmissions of two cells  $T_r/T_s$ , the reference, and the sample cells. Using the transmission calculated from the diffusion Eq. (6.7) and the correction due to multiple reflections from the integrating sphere off the sample cell (6.8), we arrive at the measured quantity

$$\frac{T_r}{T_s} = \frac{l_r^*}{l_s^*} \left( \frac{1 + \frac{4}{3} \frac{1+R}{1-R} \frac{l_s^*}{L}}{1 + \frac{4}{3} \frac{1+R}{1-R} \frac{l_r^*}{L}} \right) \frac{1 - c(1 - T_s)}{1 - c(1 - T_r)}. \quad (6.9)$$

To first order in  $l^*/L$ , this simplifies to

$$\frac{T_r}{T_s} = \frac{l_r^*}{l_s^*} \left( \frac{1 + A l_s^*/L}{1 + A l_r^*/L} \right), \quad (6.10)$$

where

$$A = (1 - c/2) \frac{4}{3} \left( \frac{1 + R}{1 - R} \right) + \left( \frac{2}{3} \frac{1 + R}{1 - R} + \alpha \right) c/2 \quad (6.11)$$

is not known accurately, but is close to 1.5 (for  $c = .8$ ,  $R = .03$ , and  $\alpha = 1$ ). The final results will change by only a few percent depending on the precise value of  $A$ . This uncertainty has little effect on our interpretation of the data. *Unnormalized* measurements, however, depend strongly on the collection efficiency  $c$ , the diffuse reflection coefficient  $R$ , and the correct value of  $\alpha$ , which in turn depends on the size of the scattering particles [18]

The DTS spectrum is calculated using Mie theory [2]. The value of  $l^*$  depends strongly on the ratio of indices of refraction between the particle and the continuous medium. For the index of refraction of water, we rely on Ref. [21]. The index of polystyrene is obtained from Refs. [23,24].

## 6.2 Results

Using nearly hard-sphere polystyrene particles in water (ionic concentration 10mM), we have tested the principles of DTS. We present data from three systems with

particle diameters between 205 and 460 nm and volume fractions of about 0.30 (see Tbl. 6.1). Each particle size allows us to probe a different region of the structure factor because the dimensionless value of  $y$  tested with each particle size is different.

The sensitivity of DTS to interparticle structure is demonstrated in Fig. 6.3 where we plot data for the three systems along with calculations based on Mie scattering theory and the Percus-Yevick approximation for  $S(q)$ . The vertical axis is the ratio of the transmission coefficient of the sample under investigation and a relatively dilute reference sample. The horizontal axis is the dimensionless wave vector corresponding to the high- $y$  cutoff of the integral in (6.6) which determines  $l^*$ . In this figure, which is a direct comparison, not a fit, we see that the Percus-Yevick structure factor does a remarkably good job of matching the relative value of  $l^*$  between different sample concentrations. Furthermore, we see that structure plays a significant role in the diffuse transmission data set. In particular, if the structure factor were flat ( $S(q) = 1$ ), then these curves would be the horizontal lines (dashed) with an ordinate equal to the ratio of the volume fractions of the sample and reference. In addition to the agreement in magnitude between the data and the Percus-Yevick structure factor, there is good agreement in the location and direction of the bends and curves in the 205 and 299 nm systems. These may be used for particle sizing. It is clear in Fig. 6.3 that the comparison between the data and the Percus-Yevick structure factor is fairly poor in the largest (460 nm) system. We believe that the reasons for this failure are twofold. First, DTS calculations rely on accurate structure factors for  $y$  less than the minimum value of  $2k_0a$ . For the 205 and 300 nm systems this is not a problem, as the first peak in the structure factor is being probed, and the range of  $y$  for which we need *a priori* knowledge is quite small. For larger systems such as the 460 nm system, the second peak in  $S(y)$  is being probed, which requires that we have accurate *a priori* knowledge of the first peak in  $S(y)$  (note that we were unable to use DTS to accurately measure the size of the 460 nm particles). The second reason is that the second peak in  $S(q)$  corresponds to a much shorter

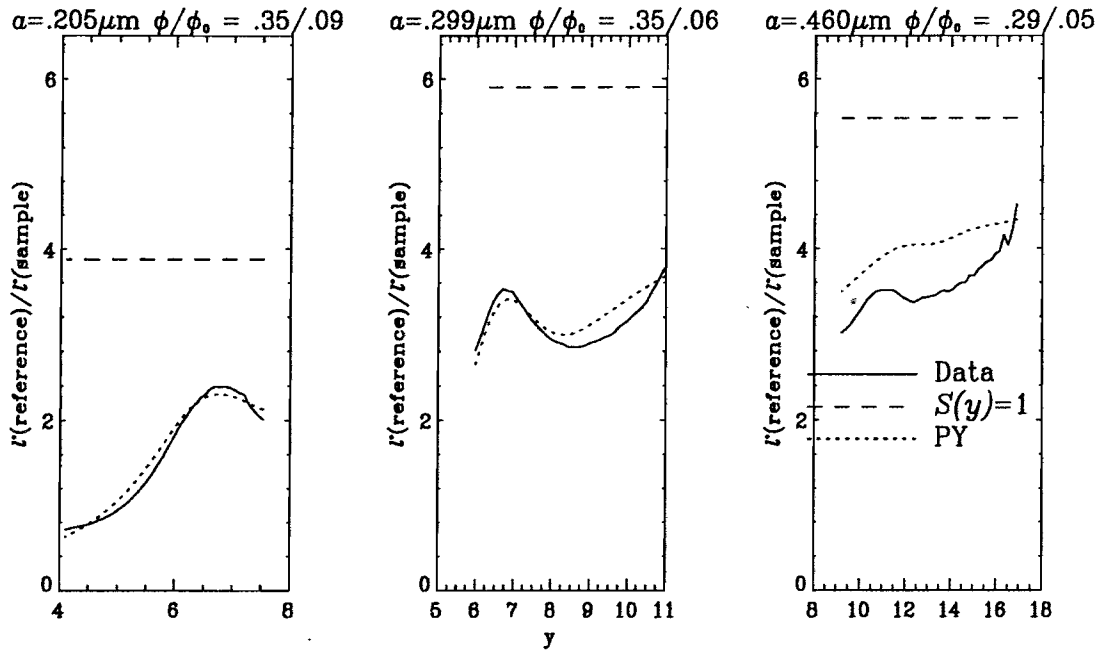


Figure 6.3: Direct comparison of diffuse transmission spectrum with Percus-Yevick calculation. A calculation ignoring structure is included in the dashed line. The separation between the dashed and dotted lines indicates how strongly the diffuse transmission spectrum depends on structure. There are no adjustable parameters in this graph. It is a comparison, not a fit.

length scale where the non hard-sphere nature of the charged particles is more likely to affect the data.

The DTS spectrum is a powerful tool for particle sizing. In Fig. 6.4, we plot the location of the peak in the DTS spectrum along with the calculated peak position (from the Percus-Yevick approximation) for different size particles. The position of this peak is the spectrum's most size-dependent feature. Based on this figure, we find that DTS can be used to estimate particle size to within 5%. This size resolution should be attainable for all samples in which the *first peak* in the structure factor is included in the scan range. Incidentally, in the course of this experiment, we used this technique to identify a 7% error in the particle size stated by the manufacturer of the 299 nm particles. This sizing error was verified by dynamic light scattering and electron microscopy.

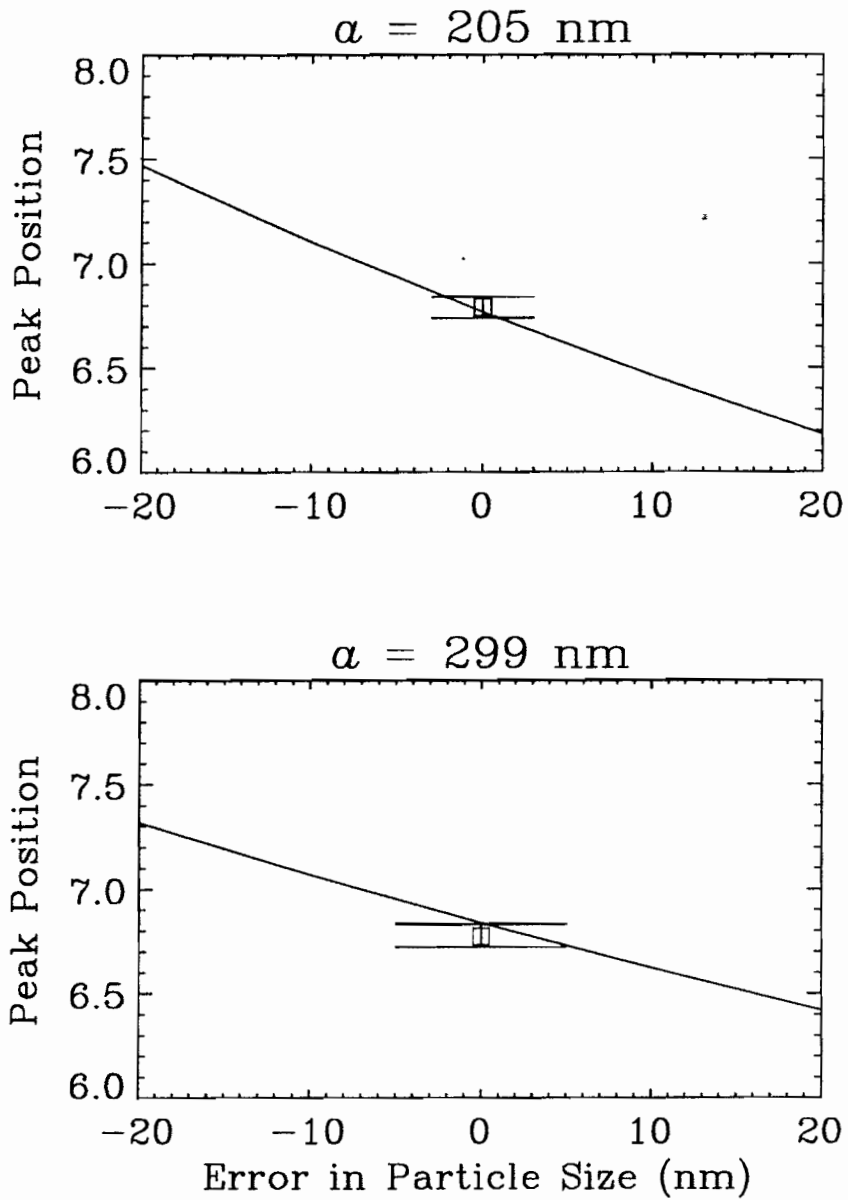


Figure 6.4: Sensitivity of DTS to particle size. The most sensitive feature to match with these data sets is the first peak in the DTS spectrum. At this point,  $l_{ref}^*/l_{sample}^*$  has zero slope. The calculated peak (solid line) matches the measured peak position quite closely. By matching of this peak, particle size can be determined with 5% accuracy.

We now compare the diffuse transmission spectra of samples that are identical except for their interparticle interaction potential. This comparison will highlight the dependence of the diffuse transmission spectrum on particle structure. A charged suspension of polystyrene spheres was prepared by rinsing a suspension of 205 nm polystyrene spheres over ion-exchange resin. After formation of a colloidal crystal, ions were added by diluting this crystal with an ion laden solution of NaCl. Four samples were prepared at the same volume fraction, but different ion contents (Tbl. 6.2). The diffuse transmission spectrum was measured using the most hard-sphere like sample as the reference. If the interparticle potential was unchanged by the change in screening length ( $l_{sc} \approx 4.3/\sqrt{[I]} \text{ \AA}$  [25]), the measured spectrum would be flat and equal to one. In fact, we see in Fig. 6.5 that the interparticle potential dramatically and progressively changed as the ion content increased. These were all non-crystalline samples which appeared white, not opalescent to the eye. Their diffuse transmission spectra, however, highlights their structural differences. This figure shows the sensitivity of DTS to changes in interparticle potential. In the event of crystallization, it is known that there will be peaks in the DTS spectrum [26] which we have observed in our apparatus. The diffusion approximation, however, does not apply to colloidal crystals. Further work with different analytic tools is necessary for crystalline samples.

Diffuse transmission at a single wavelength has been used previously to determine  $l^*$  as a function of volume fraction [10,18]. At low volume fractions,  $l^*$  is proportional to  $\phi$  and for large particles, where  $k_0 a \gg 1$ ,  $l^*$  is proportional to  $\phi$  even for fairly high volume fractions. Measurements of the dependence of diffuse transmission on volume fraction for a given system can easily be calibrated and then used for system characterization. When determining volume fraction by measuring transmission at a single wavelength, it is possible to be misled by changes in particle size or interparticle potential. By monitoring the diffuse transmission spectrum, such changes can be ruled out. Generally, horizontal shifts in the DTS spectrum indicate changes in

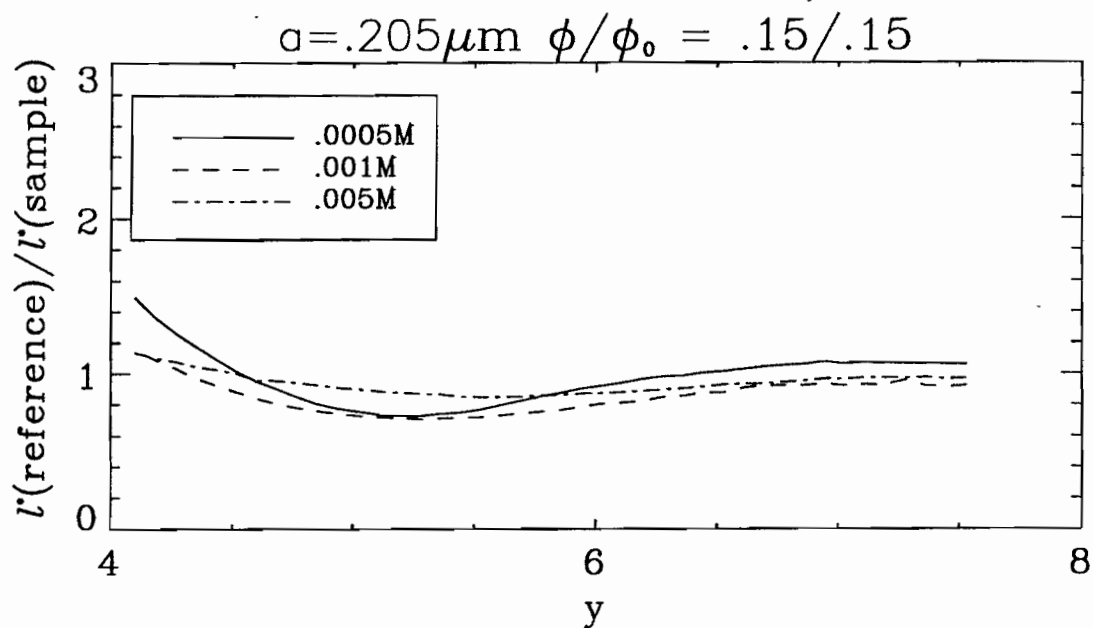


Figure 6.5: The dependence of diffuse transmission on interaction potential is seen by comparing measurements made with samples with different screening lengths. The reference sample for these data sets had the same concentration of particles, but a shorter screening length. If there was no change in structure, or if DTS was not sensitive to such a change, the spectra would be flat lines. The progressive changes with increasing screening length demonstrate the sensitivity of DTS to interparticle potential. The screening length is approximately  $50\sqrt{[I]}\text{\AA}$ , where the ion concentration is  $[I]$ .

particle size; vertical shifts indicate changing concentration, and changes in the shape of the spectrum indicate a change in the interparticle potential.

Ideally, the DTS data set can be inverted to provide not just comparisons with model calculations, but complete structure factors. We briefly present our attempts at inverting the DTS spectrum. A more complete discussion can be found later in this chapter. Inverting the equation for  $l^*$  as a function of wave-vector ( $k_0a$ ) and the structure factor (6.6) is a difficult problem. The complexity of the Mie scattering expression for the form factor and its dependence on  $k_0a$  prevent a simple analytic inversion. Further, unconstrained fits of the structure factor find rapidly varying, unphysical structure functions because at each point in  $S(y)$  the structure factor can be adjusted by the fit to exactly match the measured value of  $l^*$  at  $k_0a = y/2$ .

In order to restrict  $S(y)$  to more physical values while performing a meaningful inversion, we have examined expansions of the structure factor of the form

$$S(y) = a_0f_0(y) + a_1f_1(y) + a_2f_2(y) + \dots , \quad (6.12)$$

where the weights in the expansion  $\{a_i\}$  determine  $S(y)$ , and the functions are chosen somewhat arbitrarily. We have focussed on fits in which  $f_0(y)$  is the Percus-Yevick structure factor that we compared directly to the data in Fig. 6.3. Further terms in the expansion were alternately chosen to be powers of  $y$ , spherical Bessel functions, and Percus-Yevick structure factors calculated for different particle sizes. All of these functions gave qualitatively similar results. In Fig. 6.7, we plot the fits and associated structure functions for a polynomial expansion of the structure function

$$S(y) = a_0S_{PY}(y) + a_1 + a_2y + a_3y^2 . \quad (6.13)$$

We see good qualitative agreement with our data; the fits suggest that the first peak in  $S(y)$  is somewhat sharper than the Percus-Yevick structure factor.

The integrals necessary to invert the diffuse transmission spectrum are quite complicated, and an understanding of error propagation is similarly difficult. We estimate the sensitivity of the technique by applying it to calculated data for the

Percus-Yevick structure function with added noise. Two types of noise are included: systematic noise is introduced through a several percent variation in the height of the curve, and point by point noise with a smaller amplitude is also added. For each noisy set of calculated data, a structure function is fit. By repeating this process many times, an estimate can be made of the sensitivity of DTS to noise and experimental errors. In Fig. 6.6, we plot the best polynomial fits to our data along with the one standard deviation limits on the Percus-Yevick structure function based on inversion of noisy calculated data sets. The measured structure function for the smaller systems (205 and 299 nm) falls just outside the expected range, indicating that the first peak in  $S(y)$  is somewhat sharper than the Percus-Yevick  $S(y)$ . In the larger system, the disagreement cannot be attributed to the types of noise considered here.

We have also used this noise calculation to determine the number of parameters that can be usefully fit to the data. By repeating inversions of noisy calculated data and then fitting to different numbers of parameters, we have found that the uncertainty in  $S(y)$  increases dramatically when more than four parameters are used in the fit. That is, in fits to five or more parameters, the fits display greater sensitivity to the noise than to the underlying shape of the data set. This limit on the number of useful parameters matches our experience fitting many actual data sets.

### 6.3 Conclusion

We have seen that the diffuse transmission spectrum is a sensitive measure of structure in colloidal systems. DTS is a useful measure of the structure factor near its first peak. At higher peaks in the structure factor, however, the averaging process of diffuse transmission obscures features in the data, making the structure function difficult to recover. It is also clear that DTS can be used in a variety of systems

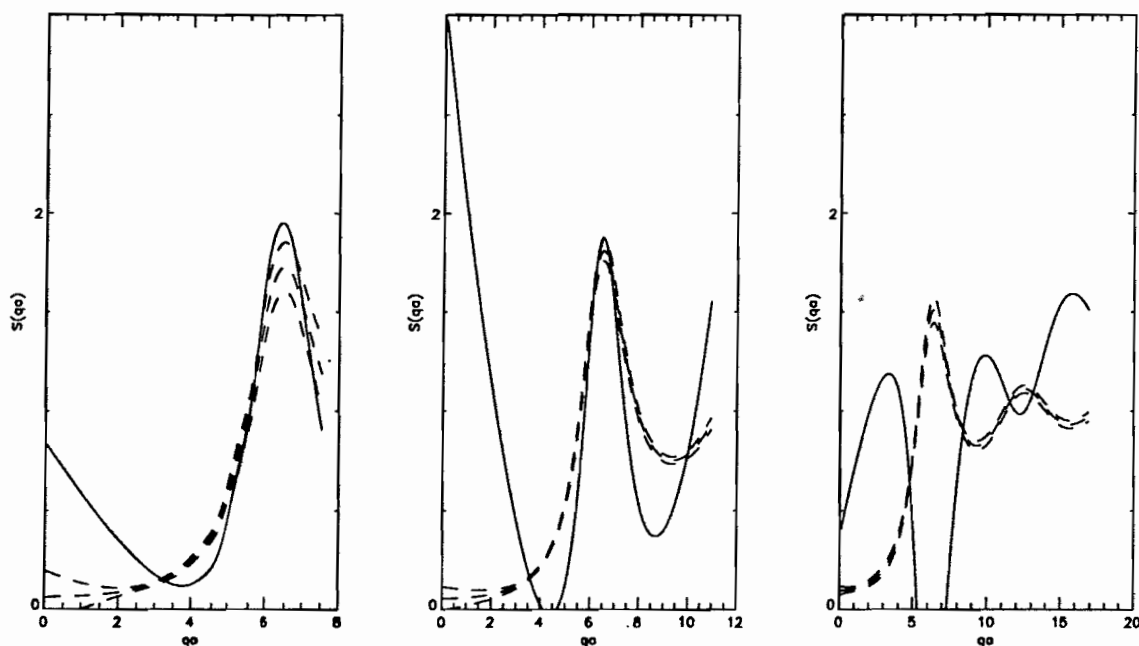


Figure 6.6: The best fit  $S(y)$  from a polynomial expansion of  $S(y)$  (solid lines) is presented along with the one-standard deviation limits on the range of measured structures (dashed lines), if the Percus-Yevick structure was correct.

to monitor changes in composition, concentration, and interaction potential without diluting the sample. DTS provides a less ambiguous signal of these changes than transmission measurements at a single wavelength, making it possible to distinguish between changes in interaction potential, particle size, and concentration. Further work is necessary on techniques for inverting diffuse transmission data and the application of diffuse transmission to more systems.

Table 6.1: To probe different length scales, we study three systems with different particle diameters.

Diameter nm	Sample $\phi$	Reference $\phi$
205	.349	.090
299	.354	.060
460	.299	.054

Table 6.2: Samples used in Fig. 6.5. All samples appeared white, not opalescent.

Diameter nm	Sample $\phi$	Ion Concentration (mM/l)	Screening Length $\text{\AA}$
205	.152	9.7	44
205	.136	5.9	56
405	.149	1.0	136
205	.149	0.51	190

## 6.4 Direct Matrix Inversion

In this section, we will detail the technique for inverting the data set directly by expressing it as a matrix product. We will see that numerical considerations, due primarily to the fact that the form factor is sharply peaked (although not singular) in the backscattering direction, make such inversion impossible.

If we regard our data set as a column vector  $\mu$  whose elements are  $l^*(k_i)$ , we can rewrite the integral expression for  $l^*$  (6.6) as a sum

$$\frac{1}{l^*(k_i)} = \frac{\pi\rho}{(k_i a)^4 k_i^2} \sum_{k_j \leq 2k_i} (k_j a)^3 F(k_j a, k_i a) S(k_j), \quad (6.14)$$

provided that the intervals  $\delta k = k_j - k_{j-1}$  are sufficiently small. In this case, we may write the form factor as a matrix of  $m$  rows and  $n$  columns,  $\mathcal{F}$  whose elements are defined by

$$\mathcal{F}_{i,j} = \frac{\pi\rho}{(k_i a)^4 k_i^2} F(k_j a, k_i a), \quad (6.15)$$

where  $\mathcal{F}_{i,j} = 0$  when  $k_j > 2k_i$  (*i.e.*, scattering angles greater than backscattering). After expressing the structure factor as a column vector  $\mathcal{S}$  with  $n$  elements  $S(k_j a)$ , we see that the data are calculated by the matrix product

$$\mu = \mathcal{F}\mathcal{S}, \quad (6.16)$$

where  $\mu$  has  $m$  elements. This expression is particularly useful because by inverting  $\mathcal{F}$ , which is calculable and depends only on the optical properties of the materials in the suspension, we can determine an analytic best fit for the structure function.

There are two numerical problems with this approach. The first problem is that the structure function is unconstrained. The best fit to the data is obtained with an unphysical structure function which rapidly oscillates between very large positive and negative values. This oscillation allows each determined point in  $S(q)$  to adjust the next calculated value of  $l^*(2k_0a)$  to exactly match the measurement. The second notable problem is conceptual and relates to the shape of the form factor and the dimensions of the  $\mathcal{F}$  matrix. Since the form factor is sharply peaked in the backscattering direction, it is essential that we choose the values of  $k_j$  at which the form factor is evaluated such that for each measurement at a wave vector of  $k_i$ , there is a  $k_j = 2k_i$ . That is, the number of columns in  $\mathcal{F}$  must satisfy  $m \geq n$ . On the other hand, the sum in (6.14) requires that  $\mathcal{F}$  be evaluated at wave vectors near 0, smaller than the smallest value of  $2k_i$ . In order to extend the sum to small wave vectors, the dimensions of  $\mathcal{F}$  must satisfy  $n > m$ . These two requirements indicate a fundamental contradiction between the logically necessary choice of dimensions for  $\mathcal{F}$  and the numerically necessary dimensions for evaluation of the sum in (6.14). This contradiction prevents use of the simplest inversion technique.

## 6.5 Inversion by Expansion of $S(q)$

Another approach can be taken to the data set, which will produce analytic best fits while constraining the structure factor against large oscillations and avoiding the contradictory demands of direct matrix inversion discussed in Section 6.4. In this approach, we express the structure factor as an expansion and determine the coefficients of this expansion by fitting to the data. The first step is to write the structure factor as a sum

$$S(y) = a_0 f_0(y) + a_1 f_1(y) + \dots + a_n f_n(y). \quad (6.17)$$

The original integral expression for  $l^*$  is now a sum over integrals that can be calculated

$$\frac{1}{l^*(k_i)} = a_0 I_0(k_i) + a_1 I_1(k_i) + \dots + a_n I_n(k_i), \quad (6.18)$$

where the integrals  $I_j(k_i)$  are defined by

$$I_j(k_i) = \frac{\pi \rho}{(k_i a)^4 k_i^2} \int_0^{2k_i a} y^3 F(y, k_i a) f_j(y) dy. \quad (6.19)$$

We construct a matrix  $\mathcal{I}$  of the integrals  $I_{i,j}$  and column vector  $A$  whose coefficients are the  $a_i$ 's in (6.17). We then write the experiment in the matrix form

$$\mu = \mathcal{I} A, \quad (6.20)$$

where  $\mu_i = 1/l^*(k_i)$ . At this point, inverting matrix  $\mathcal{I}$  will allow determination of the coefficients  $a_i$  of the expansion. Some of the same caveats that applied to the direct matrix technique in the previous section apply here as well. Although we have measured many points in each curve, the small number of features in the curves indicates that each measured point is going to provide less than one point in the structure factor. That is to say, by fitting the structure factor to too large a set of functions, we will generate fits that are better than the data warrant, often obtaining unphysical forms of the structure factor (for instance,  $S(y) < 0$ ). Using this technique, the error in  $S(y)$  for  $y$  less than the smallest  $2k_0 a$  will be substantial. The significant numerical problems with the direct matrix inversion in the previous section is avoided by use of this expansion. Rather than finding a best fit to an approximate integral, we find an approximate  $S(y)$  based on exact integrals.

The simplest functions which are likely to produce meaningful results are a combination of the Percus-Yevick structure factor (Fig. 6.1) and a simple polynomial

$$S(y) = a_0 S_{PY}(y) + a_1 + a_2 y + a_3 y^2 + \dots \quad (6.21)$$

By using the first four terms in this expansion, we obtained the results in Fig. 6.7. Significantly, we see that in the 205 and 299 nm system, the first peak in  $S(y)$  is

quite similar and more sharply peaked than the PY theory predicts. We also see that the fit is very insensitive to the shape of the structure factor for  $y$  less than the minimum measured value of  $2k_0a$ . The fit unphysically adjusts this part of the structure factor to force better agreement with the data.

Another reasonable expansion would include spherical Bessel functions. Bessel functions are similar to the actual structure factor in the sense that they have damped oscillations. We use the set of functions

$$S(y) = a_0 S_{PY}(y) + a_1 + a_2 j_0(2y) + a_3 j_1(2y) + \dots, \quad (6.22)$$

where  $j_i$  is the  $i$ th spherical Bessel function. The results in Fig. 6.8 are qualitatively the same as for fits to simple polynomials. The peaks in  $S(y)$  are more pronounced but with the same location.

A final set of fitting functions consists of several Percus-Yevick structure factors. These functions will remain physical and not change rapidly near  $q = 0$ . The disadvantage of using these functions is the loss of freedom to discover unexpected behavior in the structure factor. In this case, we use the expansion

$$S(y) = a_0 S_{PY}(y) + a_1 S_{PY}(1.2y) + a_2 S_{PY}(.8y) + a_3 S_{PY}(1.4y) + \dots \quad (6.23)$$

Again, we find good agreement for the first peak in the structure factor with somewhat sharper peaks than Percus-Yevick predicts (Fig. 6.9).

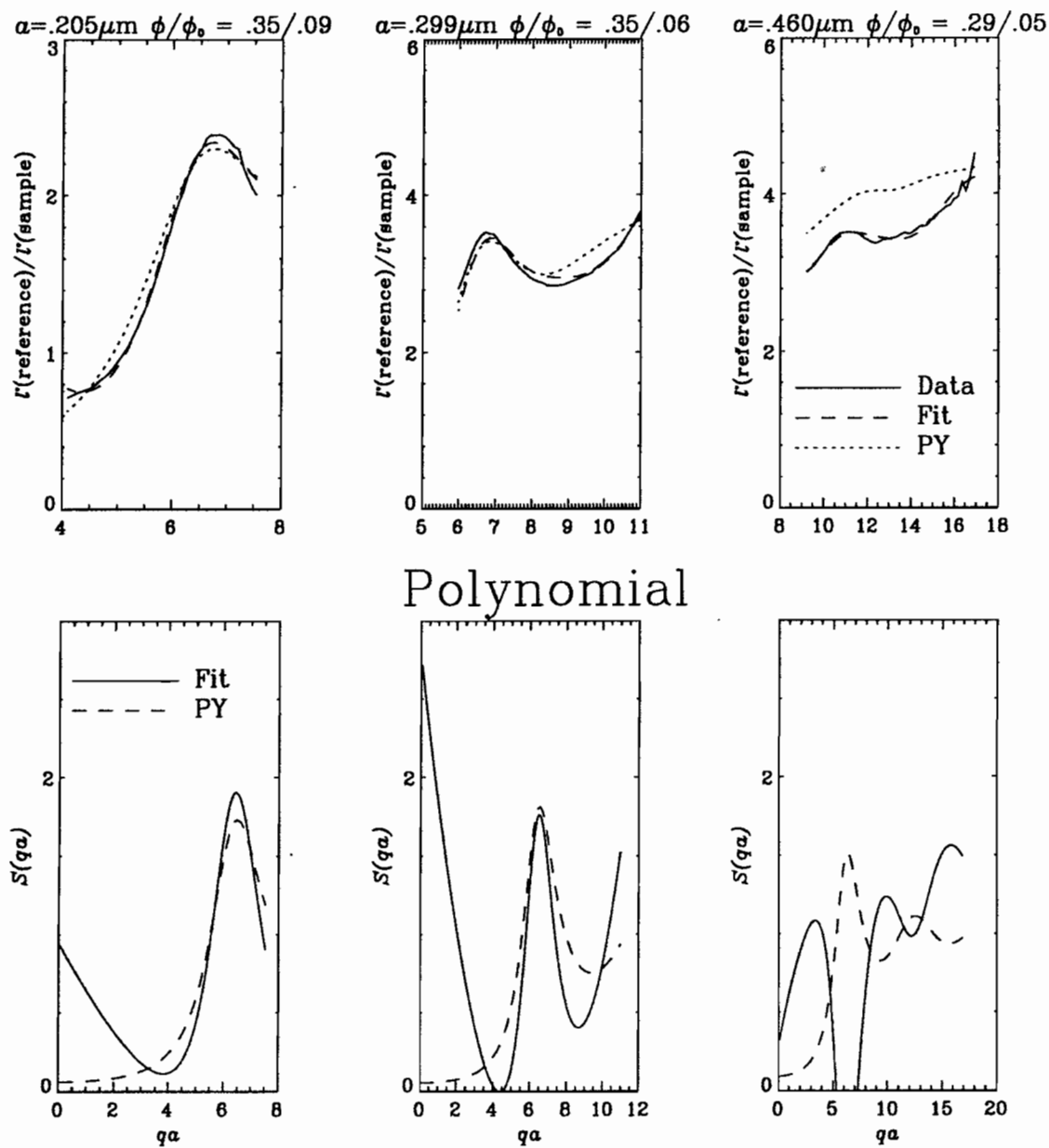
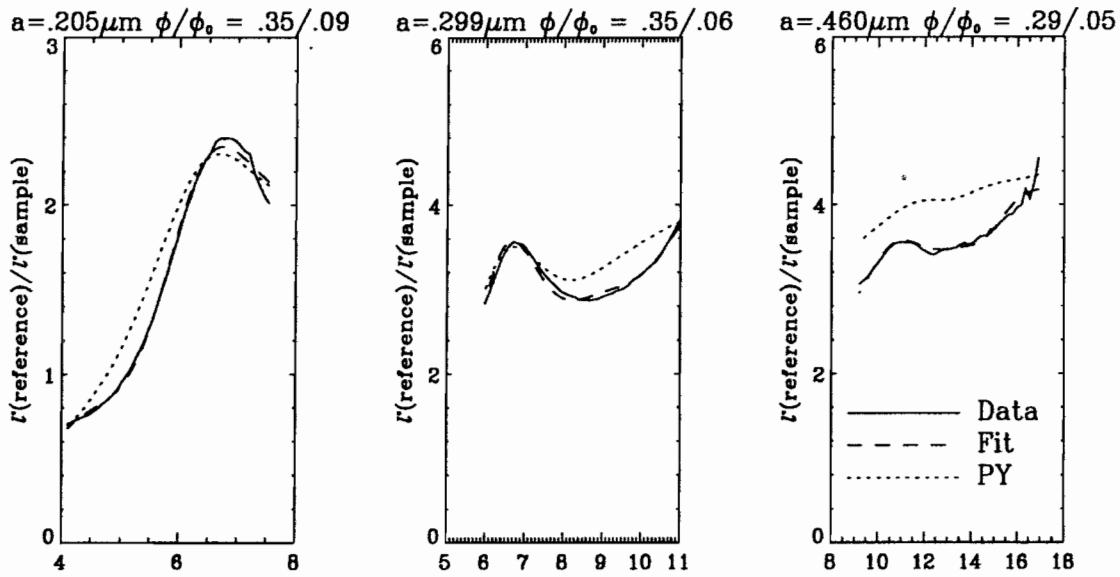


Figure 6.7: The diffuse transmission spectrum is fit with a structure function composed of the Percus-Yevick structure functions plus a polynomial. In the range we expect to have sensitivity to, the fits are reasonably good.



### Bessel Functions

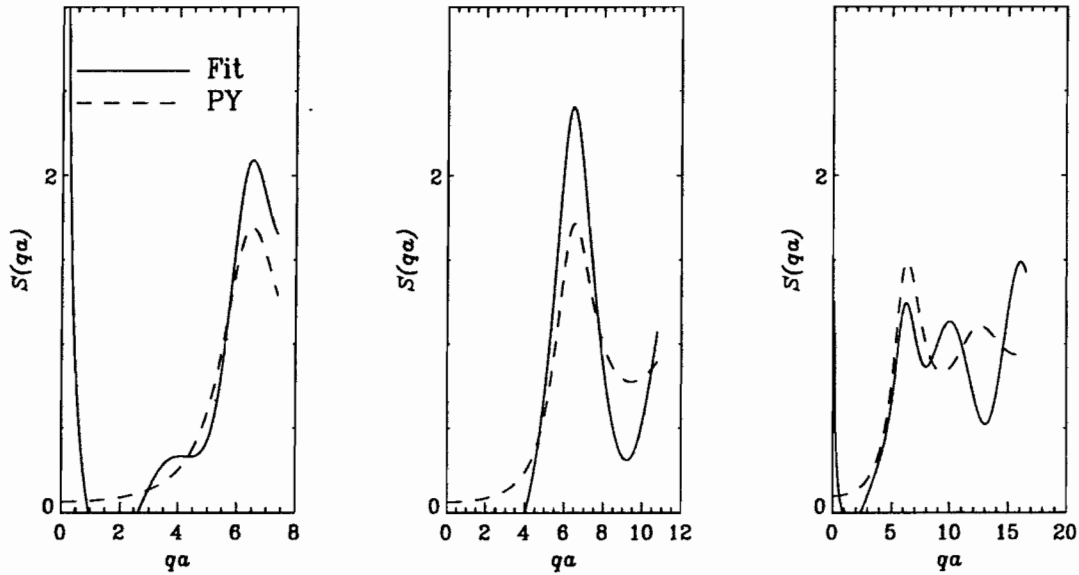
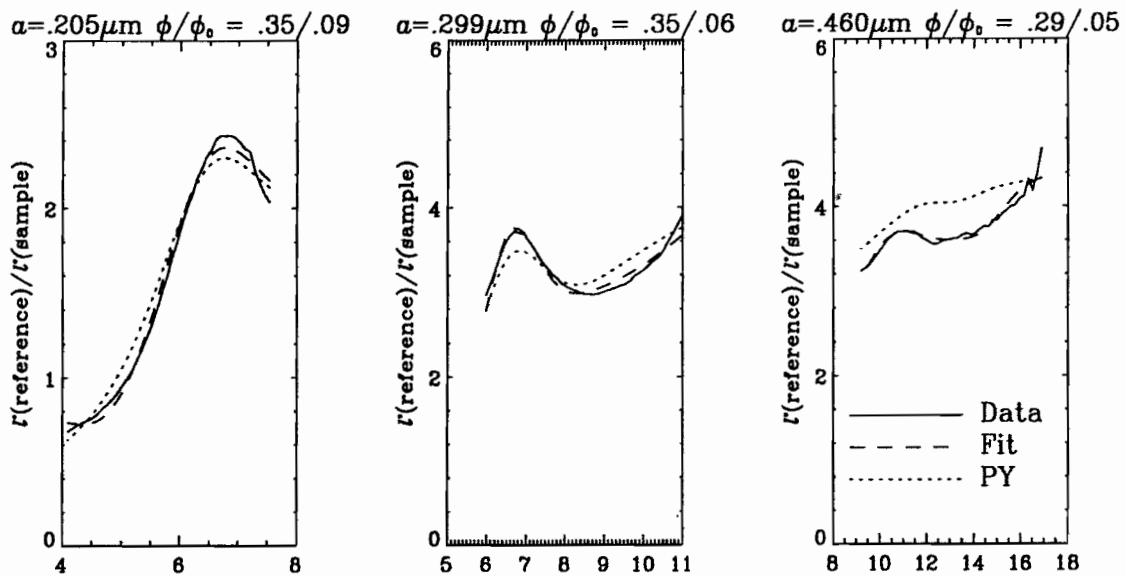


Figure 6.8: The diffuse transmission spectrum is fit with a structure function composed of the Percus-Yevick structure function plus a set of spherical Bessel functions. The results are fundamentally the same as for fits to a set of polynomials.



### Percus–Yevick

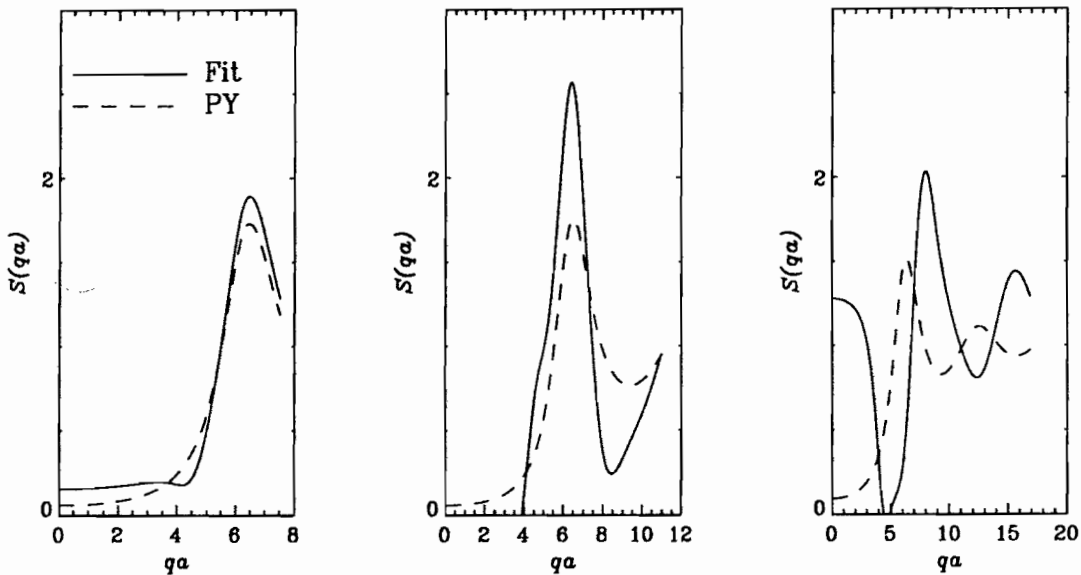


Figure 6.9: The diffuse transmission spectrum is fit with a structure function composed of a set of Percus-Yevick structure functions scaled as in Eq. (6.23). This is a more controlled strategy than the use of polynomials or Bessel functions. It is not, however, qualitatively superior.

# Bibliography

- [1] M. S. Wertheim, *Exact Solution of the Percus-Yevick Integral Equation for Hard Spheres*, Phys. Rev. Lett. **10**, 321 (1963).
- [2] A. Ishimaru, in *Wave Propagation and Scattering in Random Media* (Academic Press, New York, 1978).
- [3] C. F. Bohren, *Multiple scattering of light and some of its observable consequences*, Am. J. Phys. **55**, 524 (1987).
- [4] M. A. O'Leary, D. A. Boas, B. Chance, and A. G. Yodh, *Refraction of diffuse photon density waves*, Phys. Rev. Lett. **69**, 2658 (1993).
- [5] D. A. Boas, M. A. O'Leary, B. Chance, and A. G. Yodh, *Scattering and Wavelength Transduction of Diffuse Photon Density Waves*, Phys. Rev. E **47**, R2999 (1993).
- [6] D. J. Durian, D. A. Weitz, and D. J. Pine, *Multiple Light-scattering Probes of Foam Structure and Dynamics*, Science **252**, 686 (1991).
- [7] P. D. Kaplan, A. G. Yodh, and D. F. Townsend, *Noninvasive study of gel formation in polymer-stabilized dense colloids using multiply scattered light*, J. Coll. and Int. Sci. **155**, 31 (1993).
- [8] D. G. Dalgleish and D. S. Horne, *Studies of gelation of acidified and renneted milks using diffusing-wave spectroscopy*, Milchwissenschaft **46**, 417 (1991).

- [9] D. J. Pine, D. A. Weitz, J. X. Zhu, and E. Herbolzheimer, *Diffusing-Wave Spectroscopy: Dynamic Light Scattering in the Multiple Scattering Limit*, J. Phys. France **51**, 2101 (1990).
- [10] P. D. Kaplan, A. G. Yodh, and D. J. Pine, *Diffusion and Structure in Dense Binary Suspensions*, Phys. Rev. Lett. **68**, 393 (1992).
- [11] D. A. Weitz and D. J. Pine, in *Dynamic Light Scattering* (Oxford University Press, New York, 1993).
- [12] G. E. Elicabe and L. H. Garcia-Rubio, in *Polymer Characterization* (American Chemical Society, Washington DC, 1990).
- [13] P. R. Sperry, H. B. Hopfenberg, and N. L. Thomas, *Flocculation of latex by water-soluble polymers: experimental confirmation of a nonbridging nonadsorptive volume-restriction mechanism*, J. Coll. and Int. Sci. **82**, 62 (1981).
- [14] P. W. Anderson, *The Question of Classical Localization A Theory of White Paint?*, Philos. Mag. B **52**, 505 (1985).
- [15] E. Akkermans, P. E. Wolf, R. Maynard, and G. Maret, *Theoretical Study of the Coherent Backscattering of Light by Disordered Media*, J. De Phys. **49**, 77 (1988).
- [16] M. Kaveh, M. Rosenbluh, I. Edrei, and I. Freund, *Weak Localization and Light Scattering from Disordered Solids*, Phys. Rev. Lett. **57**, 2049 (1986).
- [17] P. E. Wolf and G. Maret, *Weak Localization and Coherent Backscattering of Photons in Disordered Media*, Phys. Rev. Lett. **55**, 2696 (1985).
- [18] S. Fraden and G. Maret, *Multiple Light Scattering from Concentrated Interacting Suspensions*, Phys. Rev. Lett. **65**, 512 (1990).

- [19] P. D. Kaplan, M. H. Kao, A. G. Yodh, and D. J. Pine, *Geometric constraints for the design of diffusing-wave spectroscopy experiments*, Appl. Optics **32**, 3828 (1993).
- [20] J. X. Zhu, D. J. Pine, and D. A. Weitz, *Internal reflection of diffusive light in random media*, Phys. Rev. A **44**, 3948 (1991).
- [21] G. Hale and M. Querry, *Optical constants of water in the 200-nm to 2000- $\mu$ m wavelength region*, Appl. Optics **12**, 555 (1973).
- [22] K. M. Yoo, F. Liu, and R. R. Alfano, *When Does the Diffusion Approximation Fail to Describe Photon Transport in Random Media?*, Phys. Rev. Lett. **64**, 2647 (1990).
- [23] Personal communication, L.H. Garcia-Rubio, University of South Florida.
- [24] T. Inagaki, E. T. Arakawa, R. N. Hamm, and M. W. Williams, *Optical properties of polystyrene from the near-infrared to the x-ray region and convergence of optical sum rules*, Phys. Rev. B **15**, 3243 (1977).
- [25] X. Qiu, *Diffusion in equilibrium and non-equilibrium interacting liquids*, Ph.D. thesis, University of Pennsylvania, 1990.
- [26] Y. Monovoukas, G. G. Fuller, and A. P. Gast, *Optical Anisotropy in Colloidal Crystals*, J. Chem. Phys. **93**, 8294 (1990).

# Chapter 7

## Experimental Necessities

It is traditional to relegate the experimental details, which have more the flavor of engineering than physics, to a series of appendices at the end of the thesis. The truth is, however, that experimental details are hardly vestigial like our own appendices. A few of these details, the ones that I remember, are thus been included in this final chapter. Most of these points were learned from others who saved me countless hours of additional frustration. As far as I can determine, they are not found in textbooks so the usual academic apparatus of citations is absent in much of this chapter.

### 7.1 Chemical Technique

Chemists are so good at the techniques needed for handling colloidal samples that they will surely greet this section with smirks. As I was not trained as a chemist, however, these details were hard to learn and deserve a few words.

#### 7.1.1 Measuring Small Volumes of Colloidal Samples

Although it is a leap of faith that the disposable plastic used to measure chemicals is really clean, the first tip is to use only disposable instruments. The only alternative method, cleaning the fine pores in glass pipettes, is not only time consuming, but

more significantly, it is guaranteed to be impossible. The reason is time. After emptying a pipette of colloid, any fluid drops which remain in the tube dry very quickly. Once they have dried, they will never re-suspend and must be physically removed from the glass wall. In cuvettes this is accomplished by scraping the wall with a piece of teflon. The fine bore of a pipette will not admit a teflon scraping tool.

There is a positive reason for using disposable instruments as well. Modern pipettes, such as the Eppendorf, pipetteman, and Rainen brands, available from any chemical instrument supply house, are incredibly accurate (repeatable to within a percent of the specified volume) when used carefully. Using them carefully involves taking the following precautions:

- *Move plunger slowly.* This is far more important for colloids which are dense and often viscous than for water. There are pipettes with stepper-motor driven plungers. These are superb.
- *Be aware of backlash.* The mechanism used to set pipette volume consists of mechanical gears, which have backlash. Be consistent about setting the volume by turning down to the correct volume.
- *Watch for air bubbles.* If you pipette an air bubble, your volume of fluid is wrong.
- *Never use the bottom 20% of a pipette's range.* In the bottom 20% of the range I have found that the accuracy steadily degrades, becoming as poor as 5% of specified volume.
- *Buy pipette tips in racks.* They are 20% more expensive, but are immeasurably easier to use than tips that come loose in bags. Ease of measurement and accuracy are almost synonymous for repetitive tasks such as sample preparation.

- *Train yourself on a balance.* Everyone should spend a few months doing all of their pipetting over a balance. The balance gives a definite measure of dispensed mass. We will all make pipetting errors, and only by working over a balance can we learn to identify them.
- *Calibrate pipettes regularly.* Our pipettes have had their seals broken due to colloid spilled into the pipette chamber. Only by regularly checking your instrument can you be sure that it is measuring accurately.

When dispensing a colloidal crystal, which is especially viscous, work *slowly* and try to avoid picking up ion exchange beads (crystal preparation will be discussed below). The ion exchange beads will settle to the bottom if the crystal is agitated in an ultrasonic cleaner.

### 7.1.2 Cleaning Glassware

The entire subject of cleaning is fraught with superstition and compulsive behavior. Nevertheless, it is important to be very clear and consistent about how each piece of glassware is cleaned. Many new experiments seem to be unrepeatably [1]. It is far superior to examine confusing data with the certainty that the difference between data sets is not due to careless cleaning. As almost none of this thesis involves use of colloidal crystals, my requirements for cleanliness were less stringent than for crystals with their fixed and extremely low ion concentration. See Ref. [2] for an example of stringent cleaning requirements.

My procedure for cleaning cells has evolved to the following:

- *Clean cell.* Like washing dishes, the cell should be free of debris, unbroken, and transparent to begin with. Stubborn polystyrene residues can be removed with acetone or, as a last resort, toluene.
- *Ultrasound in Soap Water.* There is little point to doing this for more than a

few seconds. Cells will eventually break in the ultrasound, so time should be minimized.

- *Heat in Soap Water.* I use Alcojet brand non-ionic surfactant to avoid adding ionic surfactants which interact with colloidal particles. I bring the cells to at least 80°C for at least 20 minutes. Others heat to 95°C for a full hour.
- *Rinse Several Times.* Rinse at least three times with ionically pure water of resistivity several million ohm-cm or more.
- *Ultrasound in clean water.* Again, for just a few seconds.
- *Heat in clean water.* The same heating cycle.
- *Rinse again.*
- *Rinse with Methanol.* Spectroscopic or HPLC grade methanol will not add contaminants but will help remove water from cell.
- *Blow Dry with Nitrogen.* I use a small syringe style particle filter to remove any contaminants from the nitrogen. There are heavier duty gas filters which may be more appropriate.

For working with colloidal crystals, the methanol step and nitrogen step may be skipped in favor of storing the cell in ionically pure water with ion exchange beads.

### 7.1.3 Polystyrene Spheres

The spheres used in this thesis are polystyrene in water. All were obtained from Seradyn ((800)428-4007). The spheres should be stored in a refrigerator whenever possible to avoid degradation by bacteria. The density of polystyrene is 1.05 g/cm<sup>3</sup>, so that large spheres settle quickly in the sample bottle. Eventually, these settled spheres become difficult to re-suspend. To prevent settling, spheres larger than 0.5 μm are tumbled at 1 rpm (although 1 rph would be sufficient).

Other potential suppliers of polystyrene spheres include: Bang Laboratories, in Indiana, ((317)844-7176), and Dow Diagnostics.

#### 7.1.4 Making Colloidal Crystals

Add ion exchange beads to a mixture of colloidal particles. Ion exchange beads attract free ions, cleansing their environment of the free ions. There are two kinds of beads, one attracts positive the other negative ions. Use approximately twice as many ion exchange beads (Rexyn I-300, Fischer Scientific Catalogue number R208-500) as seems reasonable, keeping in mind that at the end you will want to extract some of the sample, leaving the beads behind. Rock or tumble overnight. Place in ultrasonic cleaner to shake ion exchange beads to bottom of container. Use glass, quartz, or plastic to contain colloids. Metal surfaces will supply ions to the solution destroying crystals and even causing isotropic, fluid colloids to flocculate.

We assume that after thorough ionic cleansing, the ion concentration is entirely due to water's dissociation reaction



with the rate constant  $10^{-14}$ . That is,  $[\text{H}^+] = 10^{-7}$ . Clearly, this is a wishful assumption, and our uncertainty in ionic content is lowest at high ionic concentration, where a known quantity of ions is added, than at low ionic concentration where we merely hope that the ion exchange resin has completely cleaned the sample. If better information about ionic content is required for future experiments, conductivity measurements will be required.

#### 7.1.5 The Metler Balance

Modern electronic balances are easy to use and offer a tare feature which is a tremendous convenience. I used these high quality balances in other labs whenever practical. Sometimes, however, it is absolutely necessary to have a balance on the bench. We

were able to borrow a mechanical balance perhaps because it had become very inaccurate. While it was repeatable to 0.2 mg, it was inaccurate by as much as 10 mg. We spent some time staring at the balance and eventually figured out how to calibrate it, bringing the accuracy to 1 mg without changing the repeatability of 0.2 mg. The procedure is repeated here.

The crucial point is understanding the stability of a mechanical balance. This is an exercise in physics, so we will assume that the balance is constructed of rigid, massless rods from which massless trays are suspended by frictionless strings. While looking at Fig. 7.1, consider the effect of displacing the top balance by a small angle. The torques on each arm are identical, so the balance will simply stay tilted. This is not a useful balance because it will tip completely unless the arms are perfectly balanced; it will not reach a characteristic position even when the trays are balanced. By adding a mass to the balance arm, and centering it above the pivot point, we break the symmetry of the first balance. Now, moving the balance by a few degrees results in tipping the added mass in the direction of the tilt which will cause the balance to tip completely. This balance is unstable. A useful balance is constructed by adding a mass *below* the pivot. In this case, tipping the balance by a few degrees will move the center of mass of the balance arm in the opposite direction, providing a restoring force. Moreover, adding a small extra mass to one of the pans will cause the balance to tilt by a calculable amount. Mechanical balances are thus loaded below their pivot point!

The Metler balance has a series of knobs which must be set to within 0.1 g before using the optical scale to determine the sample mass. We use a small, cheap electronic balance to aid in setting the dials. The Metler balance always has the same mass on the sample side of the balance. It is equipped with a series of weights which are removed to compensate for the additional weight of the sample. Examining the innards of the Metler balance, we find a single carefully machined bolt which adjusts the torque of the counter balance. To calibrate the balance, this torque bolt must be

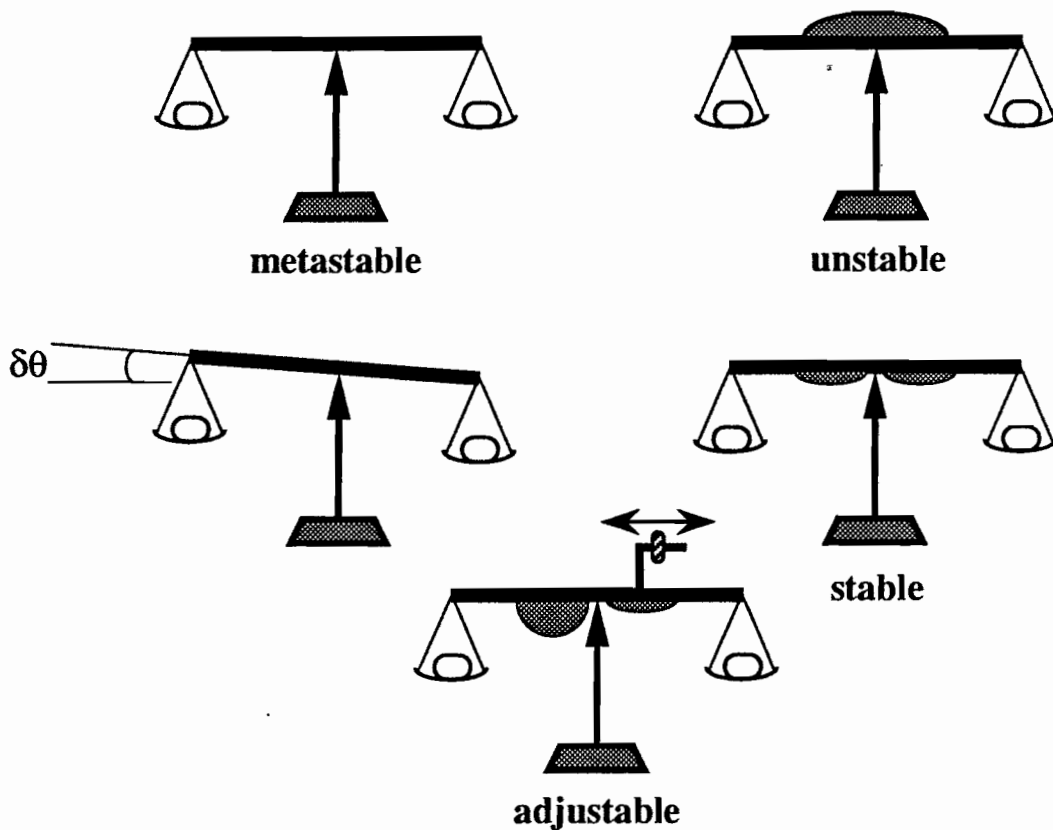


Figure 7.1: Calibration of Metler Balance. Understanding the procedure requires a simple insight into the function of a mechanical balance. If the balance arm is massless, then a mechanical balance is meta-stable, which is not useful. If a balance has its center of mass above the pivot point, it will be unstable. A balance with a center of mass below the pivot point, however, will be not only stable, but the equilibrium position of the balance when its pans contain unequal masses is calculable. Based on this principle, there is a single, calibration bolt which allows us to change the position of the CM of the balance arm.

adjusted so that the the optical scale reads 0 mg or 100 mg when the 0.1 g changes by one. The procedure is:

- *Select a calibration mass.* This mass must be an even number of tenths of a gram to within 5 mg.
- *Remove top cover of balance.* First remove all knobs, then lift cover and replace knobs.
- *Zero the balance with no mass.* This zero must be repeated at each iteration of the calibration.
- *Weigh calibration mass.* The result should be near the 00 line on the optical scale.
- *Decrease knob setting by 0.1 g.* Now the optical scale should be near the 100 line on the optical scale.
- *Adjust calibration bolt.* If the top of the optical scale reads higher than the bottom, the calibration bolt should be moved away from the pivot point.
- *Repeat sequence until difference between top and bottom are within tolerance.*  
I was able to get agreement between top and bottom of 1 mg.

### 7.1.6 Clean Water

Quantifiably clean water is essential for work with colloidal crystals. In the preparation of hard-sphere colloidal fluids, so many ions are added that there is no necessity to clean the water of anything but particles. We have purchased an Aries loop to clean ions from our tap water. The Aries loop produces water with resistivity greater than 13 M $\Omega$ -cm resistivity, typically 15 M $\Omega$ -cm (the maximum attainable resistivity is 18.3 M $\Omega$ -cm). The Aries cleaning system consists of a single carbon cartridge and two ion-exchange cartridges. In addition, it has a pump to recirculate water through

the system. Recirculation guarantees that water has passed through the cartridges before being used. Water that sits stagnant is rumored to harbor bacteria;. We use a .2  $\mu\text{m}$  final filter to remove bacteria; it has been suggested that there may still be viruses in the water.

Aries cartridges are changed by the vendor Marcor. To extend the life of these cartridges, we have added two carbon filters and one particle filter to pre-clean tap water. These additional filters have worked well and should be changed regularly. The carbon filters cost roughly 5% of the price of an Aries filter change and should thus be used liberally.

The friction of water passing through the cartridges creates a significant amount of heat that the Aries system is not designed to dissipate. We have been forced to add a fan to the front panel.

## 7.2 Optical Technique

### 7.2.1 Photomultiplier Tubes and Fiber Optics

There are three photomultiplier tubes in the DWS apparatus. Two of them are matched tubes Thorn EMI model 9863/100 chosen for their speed, sensitivity, and low dark count. One of them is a cheaper Hamamatsu tube model R586 which is slower and less sensitive, but has a very low dark count. The Hamamatsu tube is suitable for backscattering experiments with correlation functions with decay times longer than several microseconds.

Each tube is used with an amplifier/discriminator circuit with TTL output. These circuits produce one TTL pulse between 40 and 80 ns long for each incident photon. The TTL pulses drive the autocorrelator and our pulse counter. Purchasing these circuits for less than a thousand dollars is fairly difficult. We bought one from Brookhaven Instruments. They must be cajoled to sell them as special items, and

they only want to do that if you are using it with their correlator. All of our amplifier/discriminator circuits have Swiss LEMO connectors for their power supplies. These connectors are not all identical and are difficult to purchase, but they work very well. Be aware of these connectors when buying new amplifier/discriminators.

Recently, Hamamatsu has made significant progress in the manufacture and production of miniature photon counting modules which contain high voltage power supplies and amplifier/discriminators with TTL output.

We couple the PMT's to our experiment with optical fibers. Using fibers is far easier than positioning the PMT in the optical path. Fibers are easier to align and can be moved repeatedly from one spot to another with minimal effort. Further, by removing the fiber from the PMT, alignment can be checked at high-light levels without damaging the tube or changing any optical alignment. The fibers in the current apparatus are all multi-mode with 50  $\mu\text{m}$  cores. Fibers themselves are extremely cheap (several dollars), but we paid extra for protective cladding with factory aligned SMA connectors. The SMA connectors allow rapid, repeatable insertion and removal of a fiber from the experiment. The extra cost makes fibers comparable in price, but not convenience, to traditional optics. Our fibers were purchased from General Fiber Optics in Cedar Grove, New Jersey, (201) 239-3400.

The PMT's used to acquire a transmission autocorrelation function are fitted with a fiber splitter. This allows a single fiber to collect light that is divided evenly between the two tubes. The fiber splitter is far easier to use than a beam splitter because all of the careful alignment is part of the manufacturing process. Ideally, a single mode fiber would be used, but we could not find a manufacturer with a light source for alignment at 514 nm, the Argon-Ion laser wavelength.

Finally, we shield our PMT's from most room light by using a spike filter. Spike filters, available, for example, from Corion, transmit only light with wavelengths within 5 or 10 nm of their center. Whenever possible, we mount the spike filters inside the PMT housing. The small, 0.5 in diameter spike filters cost less than larger

ones, and after mounting in the PMT are extremely convenient. The use of spike filters allows us to operate with the fluorescent room lights on at a penalty of less than fifty counts per second.

The electrical connectors on the Thorn/EMI PMT's require a few words of description. The high voltage connector on most PMT's is an MHV connector. SHV connectors are required for high voltage applications in nuclear reactors because MHV connectors can be jammed onto BNC plugs. The high voltage power supply we purchased from Products for Research has one MHV and one SHV output to match our PMT configuration.

### 7.2.2 Collection Geometry

In order to detect fluctuations in the field scattered in a DWS experiment, light from a small area of the sample must be collected. To first order, this is simple to understand. This is because the total output of a large number of random sources will not fluctuate significantly. In order to limit the amount of light collected so that fluctuations will be significant, we must either collect light from a very small area of the sample over a large solid angle or collect an extremely small angle from a larger area of the sample. The criterion for scattering experiments is that the product of the area imaged and the solid angle collected be close to a square-wavelength, which is the scale on which the optical field can fluctuate. The simplest way to limit the amount of collected light is to use a single mode fiber for collection. A single mode collects a very narrow angular range of light from a small area of the sample. It is also possible to limit light collection by using a pair of pinholes.

In a two pinhole geometry (Fig. 7.2), the area imaged is  $(\pi/4)d_1^2$ , and the solid angle collected is  $(d_1/L)^2$ . We want the quantity  $dA d\Omega/\lambda^2 \leq 1$ . For a two pinhole geometry, this suggests that  $d_1 d_2/\lambda L \leq 1$ . We use an iris of approx 0.05 cm and a fiber with a 50  $\mu\text{m}$  core separated by about 5 cm. For half-micron light, this is a good collection geometry.

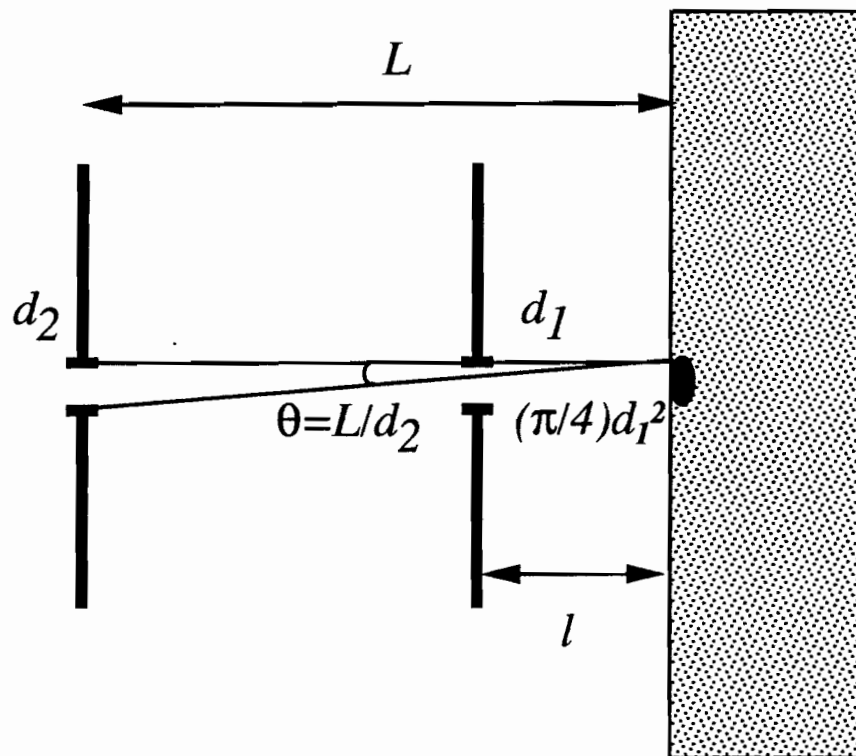


Figure 7.2: To calculate the product of the area light is collected from and the solid angle, we allow the second iris, a distance  $L$  from the sample, to define an angle and the first iris, placed  $l \ll L$  from the sample, to define a collection area.

In the DWS backscattering apparatus (Fig. 3.8), a similar argument suggests that the area imaged is given by the diameter of the fiber core multiplied by the magnification of the lens used, and the solid angle is defined by the pinhole diameter and the distance of the pinhole from the sample. We typically use a 50  $\mu\text{m}$  fiber with a magnification of 0.5 and an 0.05 cm diameter iris placed about 5 cm from the sample. This is quite good for light scattering.

### 7.2.3 Electronic Autocorrelators

In this section, we will discuss strategy for effective use of our electronic autocorrelator, the Brookhaven-Instruments model 2030. There are two items at our experimental control, the total count rate and the channel spacing. There are newer model correlators from Brookhaven-Instruments and the German manufacturer ALV which have fixed, logarithmic channel spacing. This spacing strategy is superior to the uniform channel spacing of earlier models. Autocorrelation functions tend to decay nearly logarithmically, so by giving the bin width logarithmic spacing, each channel can contribute the same amount of information to the final autocorrelation function. The most important lesson from using the logarithmically spaced correlators is that many experimental problems have signatures in the long time tail of the autocorrelation function. As a result, when using our correlator, close attention should be paid to the agreement between the measured and calculated baselines. While this detail will not diagnose most problems, it will provide evidence that they exist. Further, it is important to ensure that the autocorrelation function decays completely. The BI-2030 channels can be divided into four groups with different channel spacing. This feature should always be used. When fitting correlation functions, a logarithmic scale is often used. As a result, getting the last 0.1% of the decay is quite important.

The acquisition rate of an autocorrelation function depends on the square of the count rate and on the experimental value of  $\beta$  which corrects the Siegert relation

$$g_2(\tau) = 1 + \beta |g_1(\tau)|^2 . \quad (7.2)$$

Increasing the signal by decreasing  $\beta$ , *i.e.* by increasing the size of the collection optics, does not increase the rate at which useful data are acquired. We generally operate with  $\beta$  between 0.15 and 0.35. When  $\beta$  falls below 0.10, there is generally an experimental problem, such as laser instability, misalignment of collection optics, or light which has not passed through the sample striking the photomultiplier tubes.

While it is desirable to increase the signal rate, there is also a maximum useful signal rate. Above this maximum signal rate, the effects of dead time in the collection electronics and overflow in the autocorrelator will distort the measured autocorrelation function. The maximum safe count rate for the photomultiplier tubes is around 500,000 cps. Above 100,000 cps, however, dead time effects of the amplifier/discriminator circuit can become significant. The BI-2030 is a 4-bit autocorrelator meaning that it can acquire up 0-15 counts in a single sample time. If there are more than 15 counts, however, some are lost and error is thus introduced into the autocorrelation function. To avoid seeing this effect, the maximum count rate should average no more than two counts per sample time. For slower autocorrelation functions, especially in the backscattering geometry, the minimum bin time may be 100  $\mu$ s, limiting the total count rate to 200,000 cps. The correlator display has a box with the total number of overflows. This number should be checked on every run, and the final number should be far less than 0.1% of the number of sample times.

The autocorrelator can be controlled using the GPIB bus using the commands detailed in its manual. Be aware of two undocumented features of the GPIB interface. First, the normal strategy of addressing the correlator in the GPIB "device mode" does not work. The correlator only responds to "direct mode" GPIB addressing. In the "device mode" a full set of GPIB commands must be issued. Rather than simply issuing a GPIB write command, the computer must first issue the commands, "computer talker, correlator listener, GPIB write 'xxxxx.'" or "correlator talker, computer listener, GPIB read. The final undocumented feature is distressing. After

dumping its data to the computer, the correlator hangs and must be reset. This can be avoided by carefully reading one additional null byte that the correlator sends at the end of its data file.

#### **7.2.4 Argon-Ion Lasers**

We have two Argon-Ion lasers in the laboratory. Both have been used for Diffusing-Wave Spectroscopy. The older laser is roughly 25 years old and still operates well, having occasional water leaks and blown fuses. The newer one is closer to 5 years old and has had some significant electrical problems.

As noted in Section 3.5, the coherence properties of the laser will affect the final correlation function. For practical purposes, it is thus necessary to operate the lasers with an etalon in place to ensure a sufficiently long coherence length or a sufficiently narrow spectral laser line for DWS in the transmission geometry. Without the etalon, the laser's gain bandwidth is approximately 6 GHz, which corresponds to a coherence length of about 5 cm. With the etalon, the bandwidth is far narrower, 76 MHz, which corresponds to a coherence length of about 5 m. For thick samples, the newer laser should be used as its etalon is easier to align and produces a much more stable laser mode. For DWS in a backscattering geometry, with pathlengths of typically less than a millimeter, either laser without an etalon will work well.

All DWS work in this thesis was done with the 514 nm line of the Argon-Ion laser. Other lines are presented in Tbl. 7.1.

#### **7.2.5 Index of Refraction for Water and Polystyrene**

Mie scattering calculations depend strongly on the ratio of the index of refraction of the particle and the solvent. Although water and polystyrene are common materials, most handbooks do not publish the wavelength dependence of their indices of refraction.

The index of refraction for water has been carefully measured by many groups.

Table 7.1: Ar<sup>+</sup>-ion laser lines. Information from manual for Coherent I-200-25/7. Powers are quoted without etalon.

Wavelength (nm)	Power (W)
455	
458	
465	
472	
477	
488	8.0
497	
502	
515	10.0
529	

The best published data include not only careful experiments, but a Kramers-Kronig analysis of data at many wavelengths [3]. By fitting the data from Ref. [3] between wavelengths of 350 and 1200 nm, we find that the index of refraction of water at 18°C is well described by the equation

$$n^2(\lambda) = 1.76148 - \frac{0.013414}{\lambda^2} + \frac{0.0065438}{\lambda^2 - (0.11512)^2}, \quad (7.3)$$

where  $\lambda$  is the vacuum wavelength in microns.

The index of refraction of polystyrene spheres was measured at four wavelengths in Ref. [4]. A more complete study of the index of refraction of polystyrene was performed much earlier [5], but the data were not compiled so that they could be easily used. Garcia-Rubio and co-workers at the University of South Florida have compiled, but not yet published these older data in more useful form. Their data fit the following form quite well:

$$n(\lambda) = 1.55165 + \frac{0.00766301}{\lambda^2} + \frac{0.000291013}{\lambda^4}. \quad (7.4)$$

## 7.3 Computer Practice

It is no longer reasonable to attempt to do physics without a computer. Although I have been an avid computer user for fifteen years, the ever changing technology makes good computer practice a fluid and unattainable ideal. While a few of the most basic skills, like programming in *C* and Fortran are still useful, even their utility is fading with the advent of a variety of specialized high-level programming environments. In the course of completing this thesis, two commercial packages significantly reduced my programming time, ASYST for the PC and PV-WAVE (also known as IDL) on UNIX systems. In this section, we will review some of the computer practices used in the course of this work. There is little doubt that within a few years they will be archaic.

### 7.3.1 Laboratory Automation

Computer control of the autocorrelator, lock-in-amplifier, pulse counter, and stepper-motor systems was accomplished using ASYST on I.B.M. compatible personal computers (Intel 80286 and 80386 microprocessors) running the Microsoft DOS operating system. ASYST is an interpreted environment which uses so-called RPN or stack based logic. Syntactically, all arguments to ASYST command or operators precede the operations (*e.g.*, to add two and two, type '2 2 +'). The advantage of ASYST is that it provides simple commands for accessing GPIB controlled equipment, the parallel port and the serial port. The disadvantages of ASYST are its poor interface with external files and other software (*e.g.*, graphical output cannot be saved to a file in any commonly used format), and its reliance on a stack based syntax.

To use the parallel port to control home built electronics, we used the technical information in Tbl. 7.2, which describes the memory location of the port as well as the function and electronic configuration of each bit.

Table 7.2: Configuration of parallel port. Numbers correspond to pins on the 25pin D-shell parallel port connector. Logic is inverted for numbers with a bar. x means that a bit is unused. The base address for port LPT1 is 888(decimal). Pins 18-25 are logic ground.

Address	MSB ←								LSB	function
base	9	8	7	6	5	4	3	2	output	
base + 1	$\overline{11}$	10	12	13	15	x	x	x	input	
base + 2	x	x	x	0	$\overline{17}$	16	$\overline{14}$	$\overline{1}$	in/out	

### 7.3.2 Data Analysis

Although some elementary analysis can be done in ASYST, the difficulty of integrating ASYST with other software and computers has driven most of our data analysis to UNIX systems. Portability and the existence of good programming tools, including a debugger, make the UNIX system especially useful.

#### Using *make*

Compiling complex programs on UNIX systems is best accomplished through use of the *make* utility. This utility allows the programmer to specify which files her program depends on and how to use those files to compile the program. As I have had difficulty generating enthusiasm for *make* amongst my colleagues, a few words about writing *make* files are included here.

The instructions to *make*, in a file called *makefile* (Fig. 7.3), have two parts. The header, in which variables may be defined and compiler flags set, and the body, which consists of a list of instructions. The sample makefile, listed below, will assemble *C* or Fortran programs. Note that all file names are specified in the header; the rest is quite generic. Most people are surprised to see that the Fortran compiler *f77* is called for *C* and Fortran programs. In UNIX systems, these compilers are closely related. Fortran is sometimes translated into *C* by the compiler. The *C* and Fortran code is compiled by the generic dependency lines below and the final invocation of *f77* invokes the linker with the correct arguments for Fortran. Some of the programs

## A Generic makefile

```
FLAG=-g
NAME=program
OBJ= $(NAME).o subprog1.o subprog2.o

$(NAME) :$(OBJ) makefile
    f77 $(FLAG) -o $(NAME) $(OBJ) -ln

% .o :: % .c
    cc $(FLAG) -c $*.c

% .o :: % .f
    f77 $(FLAG) -c $*.f
```

Figure 7.3: A generic makefile. This makefile will work with *C* and/or Fortran.

used in this thesis, in particular, the fitting routines in Chapter 6, use both *C* and Fortran in the same program. As long as the programmer can keep track of the two languages' convention for exchanging arguments (Fortran always passes by reference, *C* generally passes by value), there is no confusion in this bilingual environment. The final word about *make* which will be included here is that indentation in the dependency section of the *makefile* MUST be accomplished by use of tabs, not spaces.

### 7.3.3 Pulse Counter

A 16-bit TTL pulse counter was constructed for measuring the absolute intensity of transmitted light in the DWS apparatus (Chapter 3). The counter (Fig. 7.4) consists of five chips. The first chip, a NAND gate (74LS00) enables the counter and buffers the TTL pulses generated by the amplifier/discriminator circuit on the PMT. There are two dual 4-bit counters (74LS393) which are organized as follows. The low byte is broken into 2 4-bit parts which are on the left sides of the two counter chips. The high byte is also broken into two 4-bit parts which are on the

right sides of the counter chips. The counters are cascaded by connecting the highest order bit of each counter to the input of the next counter. Finally, the 16-bit output needs to be multiplexed onto the 8-bit input of the parallel port (Tbl. 7.2). This is accomplished with two dual 4-bit buffers. The dual buffers (74LS241) have different logic on their enable pins (1 and 19), so by tying these pins together, the MUX line (in the schematic) alternately enables one 4-bit buffer or the other. The outputs are then tied together so that the final output is either 4 bits from the high byte or 4 bits from the low byte, depending on how the MUX line is set. That is, if the MUX line is high (low), then the circuit's output will be the high (low) byte.

### 7.3.4 Stepper-Motor Controller

To control the stepper-motors in Chapter 6, a stepper-motor controller was constructed. Its design is outdated, as most of the functions in this circuit can now be accomplished by a single chip.

The controller (Fig. 7.5) uses the output from four computer i/o bits to address the motor phase and five output bits to select the motor. All selection is accomplished with Darlington transistors. The fifth motor runs at 12V rather than 5V and so the transistor logic was slightly modified, but the Darlington configuration retained. Half of the diodes are protection from the inductive load of a stepper-motor phase and half of them prevent unintended current loops.

An improvement to this design would be to add a buffer between the computer and the circuit. There are currently 11 connections, so two 8-bit buffers would certainly suffice.

The translation stage which moved the sample in Chapter 6 is an old computer floppy disk drive. The floppy drive has a position sensor which was operated by providing power to the LED and then simply using the parallel port to detect the current from the position sensor's phototransistor.

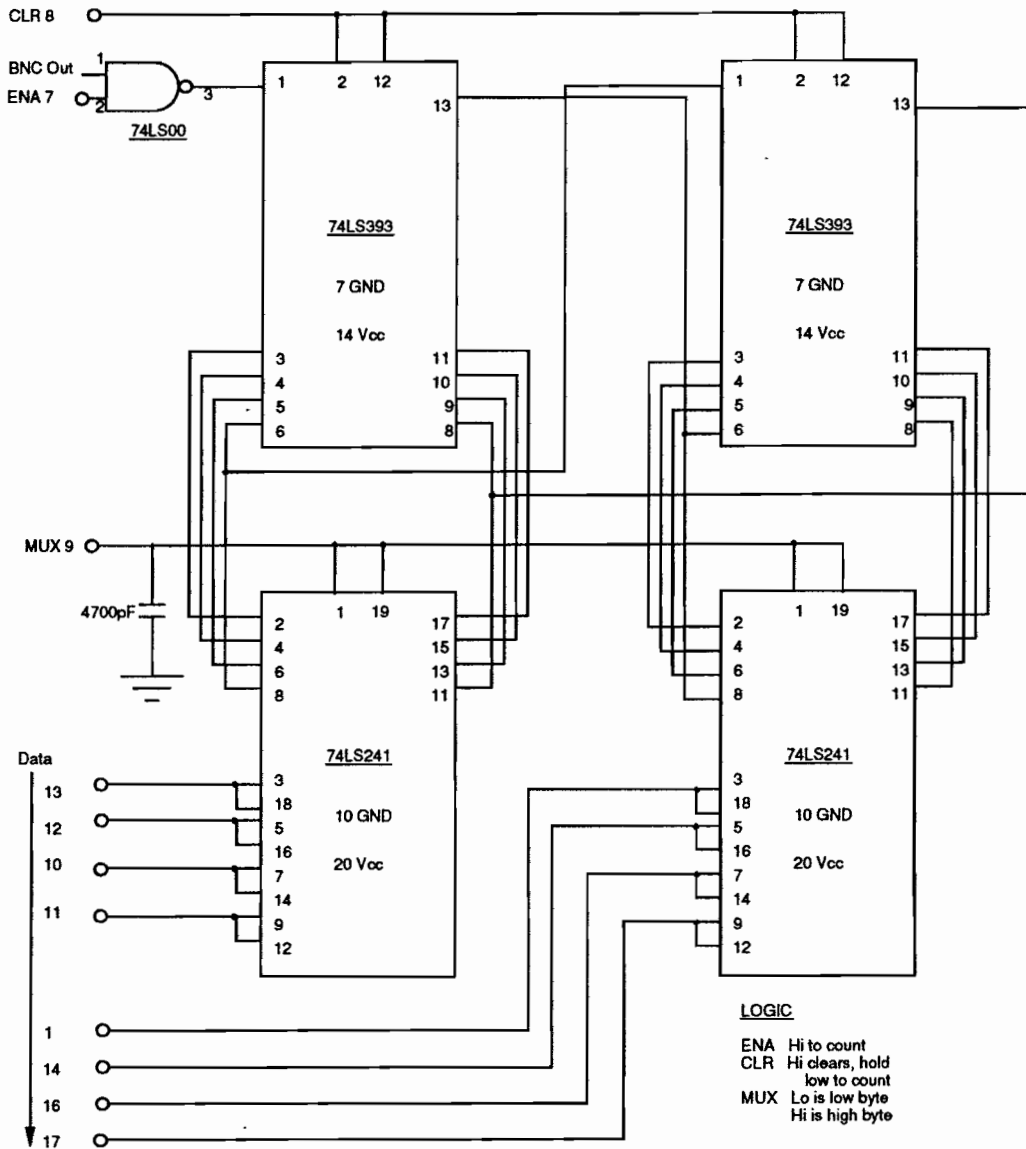


Figure 7.4: Schematic of Pulse Counter. See Tbl. 7.2 for pin connections on the computer.

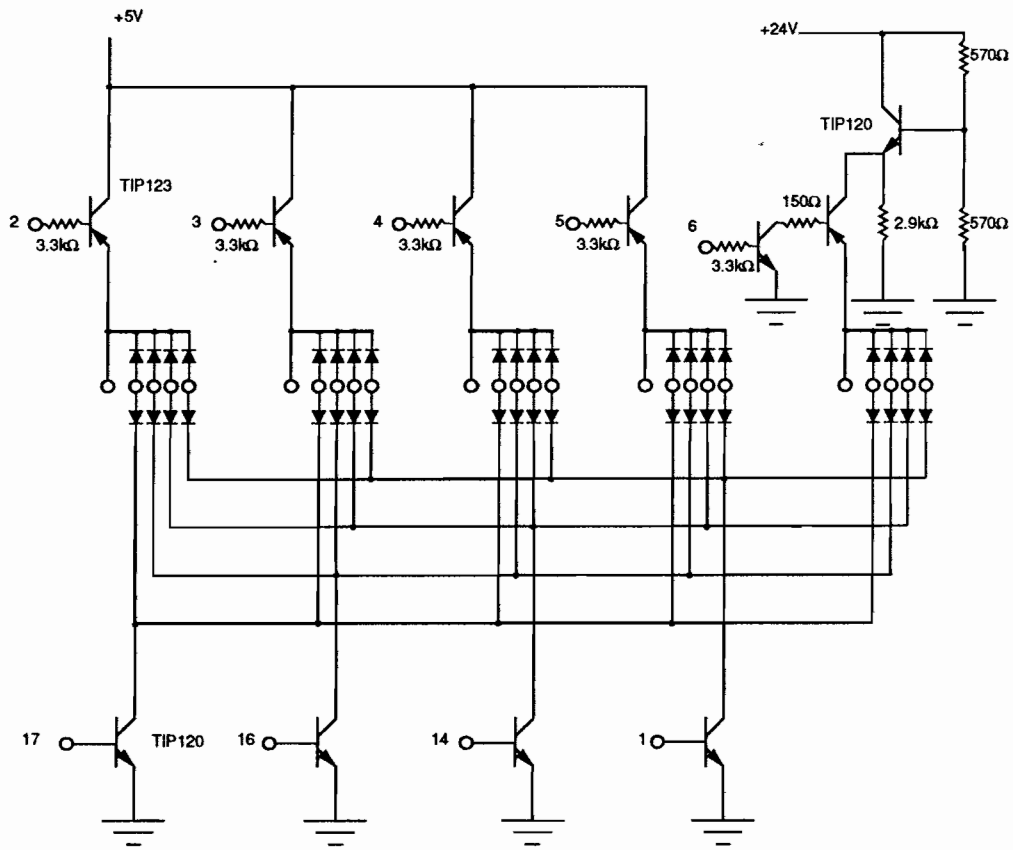


Figure 7.5: Schematic of Stepper Motor Controller. See Tbl. 7.2 for connections on the computer.

### 7.3.5 Mie Calculations

The basic program for calculating Mie scattering form factors (see Section 2.2) and the photon transport mean free path was written by David Pine. I have modified the program by including it in a loop over parameters such as particle size, wavelength, and volume fraction. The text of the basic program is included in Appendix A, along with the text of subroutines for calculating the Percus-Yevick binary hard-sphere structure factor. The program uses a combination of user input for the particle diameter and volume fraction, and input from a file, `mie.dat`, which contains the photon wavelength, temperature, and some technical parameters of the calculation. Cross sections are calculated using a Romberg integration subroutine from Ref. [6]. The transport mean free path  $l^*$  is calculated using the Percus-Yevick hard-sphere structure factor.

# Bibliography

- [1] L. X. Finegold, *Advances in Irreproducible Physics*, Bulletin of the American Physical Society **38**, no.1, 354 (1993).
- [2] X. Qiu, *Diffusion in equilibrium and non-equilibrium interacting liquids*, Ph.D. thesis, University of Pennsylvania, 1990.
- [3] D. Frenkel and A. A. Louis, *Phase separation in binary hard-core mixtures: An exact result*, Phys. Rev. Lett. **68**, 3363 (1992).
- [4] M. J. Devon and A. Rudin, *A simple technique for measuring the refractive index of polymer latexes at various wavelengths*, J. Appl. Polymer Sci. **34**, 469 (1987).
- [5] T. Inagaki, E. T. Arakawa, R. N. Hamm, and M. W. Williams, *Optical properties of polystyrene from the near-infrared to the x-ray region and convergence of optical sum rules*, Phys. Rev. B **15**, 3243 (1977).
- [6] W. H. Press, B. P. Flannery, S. A. Teukolsky, and W. T. Vetterling, *Numerical recipes in C : the art of scientific computing* (Cambridge, New York, 1988).

# Appendix A

## Listing of Mie Scattering Program

```
      program taumie
c
c Program modified by Jiuzhi Xue to calculate the transport mean
c free path and to calculate  $\langle q^2 F(q) \rangle \langle q^2 F(q) S(q) \rangle$ 
c
c Original Program by D. Pine
c
c Calculates F(q) using Mie theory for form factor
c
c Calculates S(q) for hard spheres using Percus-Yevic approximation
c W. Hess & R. Klein, Adv. Phys. vol. 32, p. 173 (1983)
c
      implicit real*8 (a-h,o-z)
      parameter (npts=200)
      real*8 m,T
      character*20 fname
      complex*16 as(100),bs(100)
```

```

external f,fs,fqq,fsqq
common a1,a2,a4,ph
commonblk1 y0,as,bs,nc
data pi3.14159265358979d0,zero1.d-8,tol1.d-8
data nterms100

c
c Get information about suspension
c rindex=index of solvent
c bindex=index of balls
c
    open(unit=4,file='mie.dat',status='old')
    read(4,*) nterms
    read(4,*) tol
    read(4,*) nrads
    read(4,*) rindex
    read(4,*) bindex
    read(4,*) wavlen
    read(4,*) phi
    read(4,*) T
    close(4)
    rindex = tlnh2o(T,wavlen)
    bindex = tlnps(T,wavlen)
    wavlen=wavlen*1.d4
    print *, ' nH2O = ',rindex,' n polystyrene = ',bindex
    m=bindexrindex

c
c Get volume fraction from user
c

```

```

        write(*,10)
10 format(' What is the volume fraction of spheres?')
        read(*,*) ph
        phi = ph
        write(*,*) 'particle diameter in microns'
        read (*,*) diam
        y0=(4.d0*pi*rindexwavlen)*(diam2.d0)
c
c Calculate coefficients for S(q)
c
        a1=-(1.d0+2.d0*ph)**2(1.d0-ph)**4
        a2=6.d0*ph*(1.d0+0.5d0*ph)**2(1.d0-ph)**4
        a4=0.5d0*ph*a1
c
c mie coefficients for the scattering amplitude
c
        ap=.5*y0
        bp=ap*m
        call coeff(nterms,ap,bp,as,bs,m,tol)
        nc=nterms
c
c Calculate  $\langle F(q) \rangle \langle F(q) S(q) \rangle$  by numerical integration
c
        call qromb(f,zero,y0,aveq)
        call qromb(fs,zero,y0,aveqs)
        scorec=aveqaveqs
        aveq1=aveqs
        write(*,300) scorec

```

```

300 format(' <F(q)><F(q)*S(q)> =',f7.4)
c
c Calculate <q*q*F(q)> and <q*q*F(q)*S(q)> by numerical integration
c
      call qromb(fqq,zero,y0,aveq)
      call qromb(fsqq,zero,y0,aveqs)
      tmfp0=y0**6*diam(aveq*ph*48.)
      tmfp1=y0**6*diam(aveqs*ph*48.)
      tcorec=aveqaveqs
      write(*,400) tcorec
400 format(' <q*q*F(q)><q*q*F(q)*S(q)> =',f7.4)
      write(*,420) tmfp0, tmfp1
420 format(' l* =',f12.4,' microns if S(q)=1',,
& ' l* =',f12.4,' microns with PY hard sphere S(q)')
      print *,'l*l =',2.*y0**2*aveq1aveqs
      print *,'sigma scatt (um2) = ',(3.14159*diam**3)(6.*tmfp0*ph)
      print *,'sigma trans (um2) = ',(3.14159*diam**3)(6.*tmfp1*ph)
      print *,'Qext (sigma scattgeom cx) =',diam(6.*tmfp0*ph)
      print *,'integrating over fqq up to y0=',y0
c
c Write results to data file
c
c open (unit=7,file='tauint.out',status='NEW',err=5000)
499 continue
c 499 write(7,500) ph,diam,wavlen,rindex,y0,scorec,tcorec,tmfp0,tmfp1
500 format(' phi =',g14.7,,
& ' diameter =',g14.7,' microns',,
& ' wavelength =',g14.7,' microns',,

```

```

& ' index of refraction =',g14.7,,
& ' 2ka =',g14.7,,
& ' <F(q)><F(q)*S(q)> =',g14.7,,
& ' <q*q*F(q)><q*q*F(q)*S(q)> =',g14.7,,
& ' l* =',g14.7,'microns æS(q)=1|',,
& ' l* =',g14.7,'microns')
c close(7)
      stop

5000 write(*,*) ' Error: tauint.out already exists.'
      write(*,*) ' please supply a new filename : '
      read(*,5010) fname
5010 format(A20)
      open (unit=7,file=fname,status='NEW')
      goto 499
      end

c-----
c Calculates S(qa) (from Percus-Yevick result)
c
      function sq(qa)
      implicit real*8 (a-h,o-z)
      common a1,a2,a4,ph
      qqaa=2.d0*qa
      qqaa=qqaa*qqaa
      sn=dsin(qqa)
      cs=dcos(qqa)
      sum1=sn - qqa*cs
      sum2=2.d0*qqaa*sn - (qqaa-2.d0)*cs-2.d0

```

```

        sum4=(qqaa*(1.2d1-qqaa)-2.4d1)*cs+2.4d1 +
& 4.d0*qqaa*(qqaa-6.d0)*sn
        cd=a1*sum1+(a2*sum2+a4*sum4qqaa)qqa
        sq=1.d0(1.d0-3.d0*ph*cdqa**3)
        return
    end

```

```

c-----
c Integrand for <F(q)> --- calls form for MIE amplitudes, and
c calculates intensities.

```

```

c Note: the q in qdq is included HERE

```

```

c

```

```

c

```

```

    function f(qa)
    implicit real*8 (a-h,o-z)
    complex*16 f1,f2
    call form(qa,f1,f2)
    b=f1*dconjg(f1)+f2*dconjg(f2)
    f=qa*b
    return
    end

```

```

c-----
c Integrand for <q*q*F(q)> ---- same as f(qa), but mul. by extra
    qa*2

```

```

c

```

```

    function fqq(qa)
    implicit real*8 (a-h,o-z)
    complex*16 f1,f2
    call form(qa,f1,f2)

```

```

b=f1*dconjg(f1)+f2*dconjg(f2)
fqq=qa**3*b
return
end

```

```

c-----
c Integrand for <F(q)*S(q)> --- same as f(qa) but includes S(q)
  from sq(qa)

```

```

c
  function fs(qa)
  implicit real*8 (a-h,o-z)
  complex*16 f1,f2
  s=sq(qa)
  call form(qa,f1,f2)
  b=f1*dconjg(f1)+f2*dconjg(f2)
  fs=qa*b*s
  return
  end

```

```

c-----
c Integrand for <q*q*F(q)*S(q)> --- same as fs(qa) but mul by
  xtra qa2

```

```

c
  function fsqq(qa)
  implicit real*8 (a-h,o-z)
  complex*16 f1,f2
  s=sq(qa)
  call form(qa,f1,f2)
  b=f1*dconjg(f1)+f2*dconjg(f2)
  fsqq=qa**3*b*s

```

```

c print *,'fsqq( ',qa,') = ',fsqq
      return
      end

c-----
c Calculate the scattering amplitude using mie theory.
c The amplitude recursion relations are derived by J. Xue
c
      subroutine form(y,f1,f2)
c
      implicit real*8 (a-h,o-z)
      complex*16 f1,f2
      real*8 sp(100),st(100)
      complex*16 spi(100), sti(100),as(100),bs(100)
      commonblk1 y0,as,bs,nc

c
c first two terms
c
c  $x = 1 - 2(\sin^2(\theta)) = \cos(2\theta)$ 
      x=1.-2.*y*y(y0*y0)

c sti(i) is the ith Legendre Polynomial, sti(i) is its derivative
      spi(1)=dcmplx(1.,0.)
      sti(1)=dcmplx(x,0.)
      spi(2)=dcmplx(3.*x,0.)
      sti(2)=dcmplx(6.*x*x-3.,0.)

c
c these are recursion rel'ns to calculate higher order terms.

```

```

do 100 n=3,nc
  fn=dbl(n)
  sp(n) = ( (2.*fn-1.)*x*spi(n-1) - fn*spi(n-2) ) (fn-1.)
  spi(n)=dcmplx(sp(n),0.)
  st(n) = fn*x*spi(n) - (fn+1.)*spi(n-1)
  sti(n)=dcmplx(st(n),0.)
100 continue

```

```

c f1 & f2 correspond to S1 and S2 in Ishimaru (S1 goes with E
  phi)

```

```

  f1=dcmplx(0.,0.)
  f2=dcmplx(0.,0.)

```

```

c Calculate the actual scattering amplitude.

```

```

do 200 i=1,nc
  enx=dbl(2*i+1)
  eny=enxdbl(i*i+i)
  f1=f1+eny*(as(i)*spi(i)+bs(i)*sti(i))
  f2=f2+eny*(bs(i)*spi(i)+as(i)*sti(i))
200 continue

```

```

  return
end

```

```

c -----

```

```

  subroutine coeff(nc,alpha,beta,a,b,m,tol)

```

```

c

```

```

c By D. Pine -- January 1988 modified April 1988 modified June
  1989

```

c some comments added Sept 1990 by Peter Kaplan  
 c  
 c This subroutine calculates the Mie coefficients  $a(n)$  and  $b(n)$ .  
     See  
 c  
 c "Wave Propagation and Scattering in Random Media"  
 c by Akira Ishimaru  
 c Academic Press, New York (1978)  
 c pp. 27-30  
 c and  
 c "Light Scattering by Small Particles"  
 c by H.C. van de Hulst  
 c Dover Publications, New York 1957 & 1981  
 c pp. 121-128, 176-177  
 c  
 c Glossary  
 c  $\alpha = k \cdot \text{radius}$   
 c  $\beta = k \cdot m \cdot \text{radius}$   
 c  $m = \text{relative index of refraction}$   
 c  $a(n) \ \& \ b(n) = \text{mie coefficients}$   
 c  $nc = \text{order up to which } a(n) \ \text{and } b(n) \ \text{are calculated}$   
 c  
     implicit real\*8 (a-h,o-z)  
     parameter (nmax=100)  
     complex\*16 tp1, tp2, bt1 , bt2, mc, a(nmax), b(nmax)  
     real\*8 m  
     real\*8 psia(nmax), dpsia(nmax), psib(nmax), dpsib(nmax)  
     real\*8 zetaa(nmax), dzetaa(nmax)

```

        if(nc.gt.nmax) nc=nmax
c ----- Initialize shorthand variables -----
        mc = dcplx(m,0.d0)
        sna = sin(alpha)
        csa = cos(alpha)
        snb = sin(beta)
        csb = cos(beta)

c
c Determine a(n) and b(n)
c
c The formula for a(n) & b(n) has spherical bessels and hankels.
c They are calculated here by explicitly writing out j1 and j2
  then
c using recursion relations (see, for example Jackson, Classical
c Electrodynamics) to calculate the higher terms. --PDK
        do 300 n=1,nc
          fn = dble(n)
          if (n.eq.1) then
            psia(1) = snaalpha - csa
            dpsia(1) = sna - psia(1)alpha
            zetaa(1) = -csaalpha - sna
            dzetaa(1) = -csa - zetaa(1)alpha
            psib(1) = snbbeta - csb
            dpsib(1) = snb - psib(1)beta
          else if (n.eq.2) then
            psia(2) = (3.d0alpha**2-1.d0)*sna - 3.d0alpha*csa
            dpsia(2) = psia(1) - 2.d0alpha*psia(2)

```

```

zetaa(2) = (-3.d0alpha**2+1.d0)*csa - 3.d0alpha*sna
dzetaa(2) = zetaa(1) - 2.d0alpha*zetaa(2)
psib(2) = (3.d0beta**2-1.d0)*snb - 3.d0beta*csb
dpsib(2) = psib(1)-2.d0beta*psib(2)
else
psia(n) = (2.d0*fn-1.d0)alpha*psia(n-1) - psia(n-2)
dpsia(n) = psia(n-1) - fnalpha*psia(n)
zetaa(n) = (2.d0*fn-1.d0)alpha*zetaa(n-1) - zetaa(n-2)
dzetaa(n) = zetaa(n-1) - fnalpha*zetaa(n)
psib(n) = (2.d0*fn-1.d0)beta*psib(n-1) - psib(n-2)
dpsib(n) = psib(n-1) - fnbeta*psib(n)
endif

```

c this formula is in Ishimaru p29

```

tp1 = dcplx(psia(n)*dpsib(n),0.d0)
tp2 = dcplx(psib(n)*dpsia(n),0.d0)
bt1 = dcplx(psia(n),zetaa(n))*dcplx(dpsib(n),0.d0)
bt2 = dcplx(psib(n),0.d0)*dcplx(dpsia(n),dzetaa(n))
a(n) = (tp1-mc*tp2)(bt1-mc*bt2)
b(n) = (mc*tp1-tp2)(mc*bt1-bt2)

```

c when the last calculated term is small, stop working

```

atest = dsqrt(dreal(a(n)*dconjg(a(n))))
btest = dsqrt(dreal(b(n)*dconjg(b(n))))
test = (2.d0*fn+1.d0)*(atest+btest)
if (test.lt.tol) goto 400

```

300 continue

400 nc = int(fn)

return

end

# Bibliography

- [1] B. J. Ackerson, R. L. Dougherty, N. M. Reguigui, and U. Nobbman, , J. Thermophys. and Heat Trans. **6**, 577 (1992).
- [2] E. Akkermans, P. E. Wolf, R. Maynard, and G. Maret, *Theoretical Study of the Coherent Backscattering of Light by Disordered Media*, J. De Phys. **49**, 77 (1988).
- [3] B. J. Alder, *Studies in Molecular Dynamics. III. A Mixture of Hard Spheres*, J. Chem. Phys. **40**, 2724 (1964).
- [4] S. Alexander *et al.*, *Charge Renormalization Osmotic Pressure and Bulk Modulus of Colloidal Crystals: Theory*, J. Chem. Phys. **80**, 5776 (1984).
- [5] P. W. Anderson, *The Question of Classical Localization A Theory of White Paint?*, Philos. Mag. B **52**, 505 (1985).
- [6] S. Asakura and Oosawa, *Interaction between particles suspended in solutions of macromolecules*, J. Polymer Sci. **32**, 183 (1958).
- [7] N. W. Ashcroft and D. C. Langreth, *Structure of Binary Liquid Mixtures I*, Phys. Rev. **156**, 685 (1967).
- [8] N. W. Ashcroft and D. C. Langreth, *Errata to Structure of Binary Liquid Mixtures I*, Phys. Rev. **166**, 934 (1968).

- [9] N. W. Ashcroft and D. C. Langreth, *Structure of Binary Liquid Mixtures. II. Resistivity of Alloys and the Ion-Ion Interaction*, Phys. Rev. **159**, 500 (1968).
- [10] J. L. Barrat, M. Baus, and J. P. Hansen, *Freezing of Binary Hard-sphere Mixtures into Disordered Crystals: a Density Functional Approach*, J. Phys. C **20**, 1413 (1987).
- [11] P. Bartlett, R. H. Ottewill, and P. N. Pusey, *Freezing of Binary Mixtures of Colloidal Hard Spheres*, J. Chem. Phys. **93**, 1299 (1990).
- [12] P. Bartlett and R. H. Ottewill, *Geometric Interactions in binary colloidal dispersions*, Langmuir **8**, 1919 (1992).
- [13] G. K. Batchelor and R. W. J. van Rensburg, *Structure Formation in Bidisperse Sedimentation*, J. Fluid Mech. **16**, 379 (1986).
- [14] G. K. Batchelor, *Brownian Diffusion of Particles with Hydrodynamic Interaction*, J. Fluid Mech. **74**, 1 (1976).
- [15] C. W. J. Beenakker and P. Mazur, *Diffusion of Spheres in a Concentrated Suspension II*, Physica **126A**, 349 (1984).
- [16] T. Beilini, M. A. Glaser, N. A. Clark, and V. Degiorgio, *Effects of finite laser coherence in quasielastic multiple scattering*, Phys. Rev. A **44**, 5215 (1991).
- [17] T. Biben and J. P. Hansen, *Phase Separation of Asymmetric Binary Hard-Sphere Fluids*, Phys. Rev. Lett. **66**, 2215 (1991).
- [18] J. Bibette, D. Roux, and B. Pouligny, *Creaming of emulsions: the role of depletion forces induced by surfactant*, J. Phys. II France **2**, 401 (1992).
- [19] J. Bibette, D. Roux, and F. Nallet, *Depletion Interactions and Fluid-Solid Equilibrium in Emulsions*, Phys. Rev. Lett. **65**, 2470 (1990).

- [20] D. A. Boas, M. A. O'Leary, B. Chance, and A. G. Yodh, *Scattering and Wavelength Transduction of Diffuse Photon Density Waves*, Phys. Rev. E **47**, R2999 (1993).
- [21] J. O. M. Bockris and A. K. N. Reddy, in *Modern Electrochemistry v.1* (Plenum Press, New York, 1970).
- [22] C. F. Bohren, *Multiple scattering of light and some of its observable consequences*, Am. J. Phys. **55**, 524 (1987).
- [23] H. S. Carslaw and J. C. Jaeger, *Conduction of Heat in Solids, Second Edition* (Oxford University Press, New York, 1959).
- [24] B. Chu, *Laser light scattering : basic principles and practice* (Academic Press, Boston, 1991).
- [25] D. J. Courtemanche and F. van Swol, *Wetting State of a Crystal-Fluid System of Hard Spheres*, Phys. Rev. Lett. **69**, 2078 (1993).
- [26] D. G. Dalgleish and D. S. Horne, *Studies of gelation of acidified and renneted milks using diffusing-wave spectroscopy*, Milchwissenschaft **46**, 417 (1991).
- [27] M. J. Devon and A. Rudin, *A simple technique for measuring the refractive index of polymer latexes at various wavelengths*, J. Appl. Polymer Sci. **34**, 469 (1987).
- [28] D. J. Durian, D. A. Weitz, and D. J. Pine, *Multiple Light-scattering Probes of Foam Structure and Dynamics*, Science **252**, 686 (1991).
- [29] G. E. Elicabe and L. H. Garcia-Rubio, in *Polymer Characterization* (American Chemical Society, Washington DC, 1990).
- [30] B. U. Felderhof, *Diffusion of Interacting Brownian Particles*, J. Phys. A **11**, 929 (1978).

- [31] B. U. Felderhof, *Hydrodynamic interaction between two spheres*, Physica A **89**, 373 (1977).
- [32] L. X. Finegold, *Advances in Irreproducible Physics*, Bulletin of the American Physical Society **38**, no.1, 354 (1993).
- [33] S. Fraden and G. Maret, *Multiple Light Scattering from Concentrated Interacting Suspensions*, Phys. Rev. Lett. **65**, 512 (1990).
- [34] D. Frenkel and A. A. Louis, *Phase separation in binary hard-core mixtures: An exact result*, Phys. Rev. Lett. **68**, 3363 (1992).
- [35] A. P. Gast, C. K. Hall, and W. B. Russel, *Polymer-induced phase separations in nonaqueous colloidal suspensions*, J. Coll. Int. Sci. **96**, 251 (1983).
- [36] A. P. Gast, W. B. Russel, and C. K. Hall, *An Experimental and Theoretical Study of Phase Transitions in the Polystyrene Latex and Hydroxyethylcellulose System*, J. Coll. Int. Sci. **109**, 161 (1986).
- [37] A. Z. Genack, N. Garcia, and W. Polkosnik, *Long-range intensity correlation and the approach to localization*, Waves in random media **3**, s57 (1991).
- [38] S. Glasstone and M. C. Edlund, in *the Elements of Nuclear Reactor Theory* (D. van Nostrand Co., Princeton N.J., 1952).
- [39] C. P. Gonatas *et al.*, *Determination of optical mean free path from pulse propagation and backscattering*, submitted Phys. Rev. E **XX**, XXX (1993).
- [40] G. Hale and M. Query, *Optical constants of water in the 200-nm to 2000- $\mu$ m wavelength region*, Appl. Optics **12**, 555 (1973).
- [41] J. P. Hansen and I. R. McDonald, *Theory of Simple Liquids*, 2nd ed. (Academic Press, London, 1991).

- [42] J. P. Hansen and I. R. McDonald, *Theory of simple liquids* (Academic Press, London, 1986).
- [43] W. Hess and R. Klein, *Generalized Hydrodynamics of Systems of Brownian Particles*, *Adv. Phys.* **32**, 173 (1983).
- [44] T. Inagaki, E. T. Arakawa, R. N. Hamm, and M. W. Williams, *Optical properties of polystyrene from the near-infrared to the x-ray region and convergence of optical sum rules*, *Phys. Rev. B* **15**, 3243 (1977).
- [45] A. Ishimaru and Y. Kuga, *Attenuation constant of a coherent field in a dense distribution of particles*, *J. Opt. Soc. Am.* **72**, 1317 (1982).
- [46] A. Ishimaru, in *Wave Propagation and Scattering in Random Media* (Academic Press, New York, 1978).
- [47] J. D. Jackson, *Classical Electrodynamics* (John Wiley and Sons, New York, 1975).
- [48] R. B. Jones, *Diffusion of Tagged Interacting Spherically Symmetric Polymers*, *Physica A* **97**, 113 (1979).
- [49] M. H. Kao, A. G. Yodh, and D. J. Pine, *Observation of brownian motion on the time scale of hydrodynamic interactions*, *Phys. Rev. Lett.* **70**, 242 (1992).
- [50] P. D. Kaplan, A. G. Yodh, and D. F. Townsend, *Noninvasive study of gel formation in polymer-stabilized dense colloids using multiply scattered light*, *J. Coll. and Int. Sci.* **155**, 31 (1993).
- [51] P. D. Kaplan, A. G. Yodh, and D. J. Pine, *Diffusion and Structure in Dense Binary Suspensions*, *Phys. Rev. Lett.* **68**, 393 (1992).
- [52] P. D. Kaplan, M. H. Kao, A. G. Yodh, and D. J. Pine, *Geometric constraints for the design of diffusing-wave spectroscopy experiments*, *Appl. Optics* **32**, 3828 (1993).

- [53] M. Kaveh, M. Rosenbluh, I. Edrei, and I. Freund, *Weak Localization and Light Scattering from Disordered Solids*, Phys. Rev. Lett. **57**, 2049 (1986).
- [54] W. G. T. Kranendonk and D. Frenkel, *Computer Simulation of Solid-liquid Coexistence in Binary Hard Sphere Mixtures*, Mol. Phys. **72**, 679 (1991).
- [55] R. Krause *et al.*, *Statics and tracer-diffusion in binary suspensions of polystyrene spheres: experiment vs. theory.*, Physica A (Netherlands). **178**, 241 (1991).
- [56] R. Krause *et al.*, *Static structure factors of binary suspensions of charged polystyrene spheres: experiment against theory and computer simulation.*, J. Phys., Condens. Matter. (UK). **3**, 4459 (1991).
- [57] A. Lagendijk, R. Vreeker, and P. DeVries, *Influence of Internal Reflection on Diffusive Transport in Strongly Scattering Media*, Phys. Lett. A **136**, 81 (1989).
- [58] J. L. Lebowitz, *Exact Solution of Generalized Percus-Yevick Equation for a Mixture of Hard Spheres*, Phys. Rev. **133**, A895 (1964).
- [59] H. M. Lindsay and P. M. Chaikin, *Elastic Properties of Colloidal Crystals and Glasses*, J. Chem. Phys. **76**, 3774 (1982).
- [60] F. C. MacKintosh and S. John, *Diffusing-Wave Spectroscopy and Multiple Scattering of Light in Correlated Random Media*, Phys. Rev. B **40**, 2383 (1989).
- [61] F. C. MacKintosh, *Multiple scattering of classical waves in random media*, Ph.D. thesis, Princeton University, 1989.
- [62] L. Mandel and E. Wolf, *Coherence Properties of Optical Fields*, Rev. Mod. Phys. **37**, 231 (1965).
- [63] G. Maret and P. E. Wolf, *Multiple Light Scattering from Disordered Media. The Effect of Brownian Motion of Scatterers*, Z. Phys. B **65**, 409 (1987).

- [64] A. Meller and J. Stavans, *Glass transition and phase diagrams of strongly interacting binary colloidal mixtures*, Phys. Rev. Lett. **68**, 3646 (1992).
- [65] Y. Monovoukas, G. G. Fuller, and A. P. Gast, *Optical Anisotropy in Colloidal Crystals*, J. Chem. Phys. **93**, 8294 (1990).
- [66] G. Nagele, O. Kellerbauer, R. Krause, and R. Klein, *Hydrodynamic effects in polydisperse charged colloidal suspensions at short times.*, Phys. Rev. E, Stat. Phys. Plasmas Fluids Relat. Interdiscip. Top. (USA). **47**, 2564 (1993).
- [67] M. A. O'Leary, D. A. Boas, B. Chance, and A. G. Yodh, *Refraction of diffuse photon density waves*, Phys. Rev. Lett. **69**, 2658 (1993).
- [68] T. Okubo, *Alloy Structures in Binary Mixtures of Highly Deionized Colloids at Sedimentation Equilibrium*, J. Chem. Phys. **93**, 8276 (1990).
- [69] R. K. Pathria, *Statistical Mechanics* (Pergammon, Oxford, 1972).
- [70] R. A. Pecorra, *Dynamic Light Scattering Applications of photon correlation spectroscopy* (Plenum Press, New York, 1985).
- [71] A. P. Philipse and A. Vrij, *Determination of Static and Dynamic Interactions Between Monodisperse Charged Silica Spheres in an Optically Matching Organic Solvent*, J. Chem. Phys. **88**, 6459 (1988).
- [72] P. Pieranski and B. Pansu, *Microspectroscopy*, J. de Phys. **46-C3**, c3 (1985).
- [73] P. Pieranski, *Colloidal Crystals*, Contemp. Phys. **24**, 25 (1983).
- [74] D. J. Pine, D. A. Weitz, J. X. Zhu, and E. Herbolzheimer, *Diffusing-Wave Spectroscopy: Dynamic Light Scattering in the Multiple Scattering Limit*, J. Phys. France **51**, 2101 (1990).
- [75] D. J. Pine, D. A. Weitz, P. M. Chaikin, and E. Herbolzheimer, *Diffusing-Wave Spectroscopy*, Phys. Rev. Lett. **60**, 1134 (1988).

- [76] W. H. Press, B. P. Flannery, S. A. Teukolsky, and W. T. Vetterling, *Numerical recipes in C : the art of scientific computing* (Cambridge, New York, 1988).
- [77] P. N. Pusey, H. M. Fijnaut, and A. Vrij, *Mode Amplitudes in Dynamic Light Scattering by Concentrated Liquid Suspensions of Polydisperse Hard Spheres*, J. Chem. Phys. **77**, 4270 (1982).
- [78] P. N. Pusey and R. J. A. Tough, in *Dynamic Light Scattering* (Plenum, New York, 1985).
- [79] P. N. Pusey and W. van Meegen, *Phase Behaviour of Concentrated Suspensions of Nearly Hard Colloidal Spheres*, Nature **320**, 340 (1986).
- [80] X. Qiu, *Diffusion in equilibrium and non-equilibrium interacting liquids*, Ph.D. thesis, University of Pennsylvania, 1990.
- [81] X. Qiu *et al.*, *Hydrodynamic Interactions in Concentrated Suspensions*, Phys. Rev. Lett. **65**, 516 (1990).
- [82] F. Reif, *Fundamentals of statistical and thermal physics* (McGraw-Hill, New York, 1965).
- [83] S. Sanyal, N. Easwar, S. Ramaswamy, and A. K. Sood, *Phase separation in binary nearly-hard-sphere colloids: evidence for the depletion force*, EuroPhys. Lett. **18**, 107 (1992).
- [84] K. S. Schmitz, *An introduction to dynamic light scattering by macromolecules* (Academic Press, Boston, 1990).
- [85] P. R. Sperry, H. B. Hopfenberg, and N. L. Thomas, *Flocculation of latex by water-soluble polymers: experimental confirmation of a nonbridging nonadsorptive volume-restriction mechanism*, J. Coll. and Int. Sci. **82**, 62 (1981).

- [86] M. R. Spiegel, *Schaum's Outline Series Theory and Problems of Mathematical Handbook of Formulas and Tables* (McGraw-Hill, New York, 1968).
- [87] M. J. Stephen, *Temporal Fluctuations in Wave Propagation in Random Media*, Phys. Rev. B **37**, 1 (1988).
- [88] D. J. Tritton, *Physical Fluid Dynamics* (van Nostrand Reinhold Co., New York, 1977).
- [89] L. Tsang, J. A. Kong, and T. Habashy, *Multiple scattering of acoustic waves by random distribution of discrete spherical scatterers with the quasicrystalline and Percus-Yevick approximation*, J. Acoust. Soc. Am. **71**, 552 (1982).
- [90] D. A. Weitz and D. J. Pine, in *Dynamic Light Scattering* (Oxford University Press, New York, 1993).
- [91] M. S. Wertheim, *Exact Solution of the Percus-Yevick Integral Equation for Hard Spheres*, Phys. Rev. Lett. **10**, 321 (1963).
- [92] P. E. Wolf and G. Maret, *Weak Localization and Coherent Backscattering of Photons in Disordered Media*, Phys. Rev. Lett. **55**, 2696 (1985).
- [93] H. Xu and M. Baus, *The Partial Freezing of Hard-sphere Mixtures*, J. Phys. C **20**, L373 (1987).
- [94] E. Yablonovitch, *Photonic band-gap structures*, J. Opt. Soc. Am. B **10**, 283 (1993).
- [95] A. G. Yodh, P. D. Kaplan, and D. J. Pine, *Pulsed Diffusing-Wave Spectroscopy: High Resolution through Nonlinear Optical Gating*, Phys. Rev. B **42**, 4744 (1990).
- [96] A. G. Yodh *et al.*, *Speckle fluctuations and their use as probes of dense random media*, Mol. Cryst. Liq. Cryst. Sci. Technol. - Sec B Nonlinear Optics **3**, 149 (1992).

- [97] K. M. Yoo, F. Liu, and R. R. Alfano, *Errata: When Does the Diffusion Approximation Fail to Describe Photon Transport in Random Media?*, Phys. Rev. Lett. **65**, 2210 (1990).
- [98] K. M. Yoo, F. Liu, and R. R. Alfano, *When Does the Diffusion Approximation Fail to Describe Photon Transport in Random Media?*, Phys. Rev. Lett. **64**, 2647 (1990).
- [99] J. X. Zhu, D. J. Pine, and D. A. Weitz, *Internal reflection of diffusive light in random media*, Phys. Rev. A **44**, 3948 (1991).
- [100] J. Zhu, *Diffusing-Wave Spectroscopy*, Ph.D. thesis, City University of New York, 1992.
- [101] J. M. Ziman, *A Theory of the Electrical Properties of Liquid Metals I: The Monovalent Metals*, Philos. Mag. **6**, 1013 (1961).
- [102] Measurements of non-hard-sphere structure were performed by M.H.G. Duits, R.P. May, A. Vrij, and C.G. de Kruif, J. Chem. Phys. **94**, 4521 (1991); H.J.M. Hanley, G.C. Straty, and P. Lindner, Physica A **174**, 60 (1991). Polydisperse hard-spheres have been studied by C.G. de Kruif, W.J. Briels, R.P. May, and A. Vrij, Langmuir **4**, 668 (1988).
- [103] M. P. van Albada, B. A. van Tiggelen, A. Lagendijk, and A. Tip, *Speed of Propagation of Classical Waves in Strongly Scattering Media*, Phys. Rev. Lett. **66**, 3132 (1991).
- [104] J. S. van Duijneveldt, A. W. Heinen, and H. N. W. Lekkerkerker, *Phase separation in bimodal dispersions of sterically stabilized silica particles*, Europhys. Lett. **21**, 369 (1993).

- [105] A. van Veluwen, H. N. W. Lekkerkerker, C. G. de Kruif, and A. Vrij, *Influence of Polydispersity on Dynamic Light Scattering Measurements on Concentrated Suspensions*, J. Chem. Phys. **89**, 2810 (1988).
- [106] A. van Veluwen, H. N. W. Lekkerkerker, C. G. de Kruif, and A. Vrij, *Measurement of the Short Time Self-diffusion Coefficient in Dilute and Concentrated Suspensions: Influence of Direct Particle Interactions*, J. Chem. Phys. **87**, 4873 (1987).

# Index

- $\alpha$ , 22, 24, 50, 51, 117, 120
- $l^*$ , 13, 58, 61–64, 68–70, 72, 113, 116,  
117
  - and  $l$ , 13, 14
  - and index of refraction, 121
  - and persistence length, 13
- binary
  - non-interacting theory, 69
- definition
  - average scattering angle, 13
- $q$ 
  - average square, 14
  - definition, *see* scattering wave vector
- $y$ 
  - definition, *see*  $q$
- colloidal crystals
  - cleaning ions, 144
- diffusion
  - collective
    - $y$ -dependence, 45, 65–67, 71
  - collective and self, 45
  - hydrodynamic calculations, 75
  - diffusion approximation, 12
    - and colloidal crystals, 125
  - diffusion equation
    - assumptions, 12
- DWS
  - backscattering correlation function, 50
  - transmission correlation function, 51
- electron microscopy of polystyrene spheres, 108
- entropic crystallization
  - interstitial particles, 103
- entropy
  - and volume exclusion, 84
  - at a wall, 84
  - phase transitions, 82
- field correlation function, 33–39, 48–50, 52, 71
  - backscattering, 50
  - transmission, 51
- form factor
  - amplitude, 10

- and partial cross section, 17
  - definition, 10
  - peaked at small angles, 12
- Kossel lines, 9, 106
- milk, 1, 8, 112
- multiple scattering
  - loss of information, 12
  - phenomena, 12
  - prevalence, 1, 2
  - techniques, 9, 12
- optical fiber, 11, 149, 150, 152
- particle size
  - experimental determination, 123, 124
- Percus Yevick
  - plot of structure factor, 74, 114
- photon flux, 22, 24, 117
- photon transport
  - in colloidal crystals, 125
- polystyrene
  - density, 143
  - refractive index, 155
- polystyrene spheres
  - sizes, 2
- refractive index, 21, 115
  - wavelength dependence
    - polystyrene, 155
    - water, 155
- refractive index-matching, 112
- sample cell, 21, 24–26, 118, 142, 143
- scattering geometry, 2, 3, 11
- Siegert relation, 39, 41, 44, 48, 152
- $\beta$ 
  - experimental limits, 153
- structure factor
  - change with interaction potential, 125
  - definition, 10
  - expansion in Bessel functions, 135
  - expansion in Percus-Yevick functions, 133
  - expansion in polynomials, 132, 134
  - symmetry, 10
- transmission of a slab, 120
  - apparatus, 118, 119
  - corrections for multiple reflections, 121
  - importance of normalized measurements, 121
  - technique, 118
- two body calculations
  - unreasonable success, 75
- volume overlap, 4, 84, 85, 95–97
- white, 8